

DESIGN OF RF AND MICROWAVE PARAMETRIC AMPLIFIERS AND POWER UPCONVERTERS

A Thesis
Presented to
The Academic Faculty

by

Blake Raymond Gray

In Partial Fulfillment
of the Requirements for the Degree
Doctor of Philosophy in the
School of Electrical and Computer Engineering

Georgia Institute of Technology
May 2012

DESIGN OF RF AND MICROWAVE PARAMETRIC AMPLIFIERS AND POWER UPCONVERTERS

Approved by:

Professor John Papapolymou,
Committee Chair
School of Electrical and Computer
Engineering
Georgia Institute of Technology

Professor J. Stevenson Kenney,
Advisor
School of Electrical and Computer
Engineering
Georgia Institute of Technology

Professor Kevin Kornegay
School of Electrical and Computer
Engineering
Georgia Institute of Technology

Professor Ronald Harley
School of Electrical and Computer
Engineering
Georgia Institute of Technology

Professor Paul Kohl
School of Chemical and Biomolecular
Engineering
Georgia Institute of Technology

Date Approved: 15 January 2012

ACKNOWLEDGEMENTS

First and foremost, the author would like to acknowledge the assistance and support of his advisor, Prof. Steve Kenney, whose insight and guidance over the author's years at Georgia Tech was indispensable. The author would also like to thank the electrical and computer engineering department at Georgia Tech for their help in transitioning from a doctoral student, to doctoral candidate, to doctoral graduate.

The author would like to thank the support offered by his committee members at Georgia Tech, Prof. John Papapolymerou, Prof. Kevin Kornegay, and Prof. Ronald Harly. The author is well aware of just how busy each faculty member is, so the time investments each made to sit on his committee, review his dissertation and listen to his presentations was much appreciated.

The author would like to specially thank Dr. Robert Melville at New Jersey Institute of Technology, Dr. Franco Ramirez and Prof. Almudena Suarez at University of Cantabria in Santander, Spain, who spent their free time assisting with simulations and measurements and offered their expertise in his research endeavors.

The many conversations had with friends and colleagues at Georgia Tech and elsewhere were very helpful in working out problems in the author's research work that just didn't want to seem to go away, and he is much appreciative.

Finally, thanks should go to the author's family back in Kansas City, Missouri, who have continued to support him both financially and emotionally through this process.

TABLE OF CONTENTS

ACKNOWLEDGEMENTS	iii
LIST OF FIGURES	vi
SUMMARY	ix
I INTRODUCTION	1
1.1 High-Gain Single-Stage Power Amplifiers	2
1.2 Conventional Power Amplifier Efficiency-Enhancement Techniques .	3
1.2.1 Class-A Mode	7
1.2.2 Class-AB Mode	7
1.2.3 Class-B Mode	8
1.2.4 Class-C Mode	8
1.3 Bandwidth Limitations in Transconductance Power Amplifiers . . .	9
1.4 Broadband High-Efficiency Parametric Architectures	11
1.5 Thesis Organization	12
II THEORY OF PARAMETRIC AMPLIFIERS	13
2.1 The Manley-Rowe Relations	13
2.2 Phase-Incoherent Upconverting Parametric Amplifiers	19
2.3 Negative-Resistance Parametric Amplifiers	24
2.3.1 Nondegenerate Negative-Resistance Parametric Amplifiers . .	25
2.3.2 Phase-Coherent Degenerate Negative-Resistance Parametric Amplifiers	30
III ANALYTICAL MODELING OF PARAMETRIC AMPLIFIERS	33
3.1 Phase-Incoherent Parametric Upconverting Amplifiers	33
3.2 Phase-Coherent Degenerate Parametric Amplifiers	43
3.3 Phase-Coherent Upconverting Parametric Amplifiers	48
IV DESIGN AND PERFORMANCE OF UPCONVERTING AND NEGATIVE-RESISTANCE PARAMETRIC AMPLIFIERS . . .	54

4.1	VHF and RF Phase-Incoherent Upconverting Parametric Amplifiers	54
4.2	Phase-Coherent Negative-Resistance Degenerate Parametric Amplifiers	62
4.3	Phase-Coherent Upconverting Parametric Amplifiers	69
V	STABILITY ANALYSIS OF PARAMETRIC AMPLIFIERS . .	72
5.1	Conditional Stability of Phase-Incoherent Upconverting Parametric Amplifiers	73
5.2	Conditional Stability of Negative-Resistance Parametric Amplifiers .	77
5.3	Conditional Stability of Phase-Coherent Upconverting Parametric Amplifiers	86
VI	CONCLUSIONS AND FUTURE WORK	88
6.1	Summary and Comparisons to Current State-Of-The-Art	88
6.2	Contributions	92
6.3	Future Work	94
	BIBLIOGRAPHY	99
	VITA	104

LIST OF FIGURES

1	Plot of the amplitude of (1.8) for a constant and normalized $I_{max} = 1$ as the conduction angle decreases from 2π to 0.	6
2	Simplified circuit model that Manley and Rowe considered for their derivation.	15
3	A phase-incoherent upconverting parametric amplifier.	21
4	Change in term 1 in (2.23) with changing maximum-to-minimum nonlinear capacitance ratio.	23
5	An equivalent circuit of a nondegenerate negative-resistance parametric amplifier.	26
6	An equivalent circuit of a degenerate negative-resistance parametric amplifier. The pump circuit has been omitted, however, its effects have been included in the definition of $C(t)$ in (2.49). The parallel resonant traps have also been omitted by assuming on-resonance operating conditions.	30
7	Piecewise-linear approximation of the square-law region of the varactor junction capacitance, as normalized to its maximum value at 0V bias, versus ideal characteristics. This figure demonstrates the difference between the varactors maximum available change in capacitance, as opposed to that observed under RF drive.	37
8	Plot of the change in the gain-degradation factor versus varactor capacitance ratio with $\gamma = 0.1, 0.5$ and 1.	39
9	A degenerate parametric amplifier utilizing a nonlinear capacitance. The circulator, $L_s - C_s$, and $L_p - C_p$ electrically isolate the output, source, and pump currents, respectively, from one another.	43
10	Equivalent circuits of the degenerate parametric amplifier in Fig. 9 as seen by (a) the source current generator, and (b) the pump current generator.	46
11	Equivalent circuit as seen by the pump current generator according to (3.48).	48
12	Idealized equivalent circuit for a phase-coherent upconverting parametric amplifier utilizing a nonlinear capacitance. The circulator, $L_s - C_s$, $L_p - C_p$, and $L_{3fs} - C_{3fs}$ electrically isolate the source, pump, and output currents, respectively, from one another.	49
13	Circuit topology for both the VHF and RF phase-incoherent upconverting parametric amplifiers.	55

14	Hardware implementation of the VHF upconverting parametric amplifier.	56
15	Simulated and measured gain and efficiency versus source power for the VHF upconverting parametric amplifier.	57
16	Comparison of surface plots of the measured gain of the VHF breadboard upconverting parametric amplifier against predicted by the analytical model of (3.17).	59
17	Comparison of surface plots of the measured system efficiency of the VHF breadboard upconverting parametric amplifier against predicted by the analytical model of (3.34).	60
18	Mathematical reasoning behind the error between the prediction made by the gain analytical model of (3.17) and the measured results from the VHF breadboard upconverting parametric amplifier.	61
19	Surface plot comparison of the measured gain of the RF breadboard upconverting parametric amplifier to that predicted by the analytical model of (3.17).	62
20	Comparison of surface plots of the measured system efficiency of the breadboard parametric upconverter against the predicted efficiency of the analytical model of (3.34).	63
21	A double-balanced mixer showing the incident and reflected source, pump, and output waves. By Conservation of Phase, the reflected source waveforms will be in-phase and will combine at the center tap of the secondary of the source balun.	64
22	Equivalent circuit from the perspective of the source generator. The polarity of the pumping voltage across each varactor is indicated to illustrate how Conservation of Phase for mixers will guarantee the reflected waves will always be in-phase.	65
23	Circuit schematic of the double-balanced phase-coherent degenerate parametric amplifier showing all component values.	66
24	Photograph of the prototype double-balanced phase-coherent degenerate parametric amplifier board with critical components identified and labeled.	67
25	Test bench setup to measure gain, bandwidth, and stability of the phase-coherent degenerate parametric amplifier.	68
26	Plot of the simulated and measured gain versus source frequency of the double-balanced phase-coherent degenerate paramp at a constant pump power level of 30 dBm.	69

27	Plot of the measured and predicted gain versus both the available source and pump power of the double-balanced phase-coherent degenerate parametric amplifier at $f_s = 650$ MHz.	70
28	Plot of the measured and predicted AM-AM distortion characteristics of the double-balanced phase-coherent degenerate parametric amplifier for several values of power gain at $f_s = 650$ MHz.	71
29	Simulated and measured transducer gain versus upconverted output frequency in addition to predicted values according to the analytical model in (3.66).	71
30	A black box phase-incoherent upconverting parametric amplifier. The incident and reflected source and output waves can be expressed independently of one another, allowing for the two ports to be analyzed individually.	74
31	Evolution of the system poles of the phase-coherent degenerate parametric amplifier as the pump power level is swept. A set of complex poles at 650 MHz cross the imaginary axis at about $P_p = 30.85$ dBm causing a flip bifurcation and destabilizing the amplifier. The paramp appears to be stable when $P_p < 30.5$ dBm.	80
32	Solution curve of the phase-coherent degenerate parametric amplifier at $f_s = 716$ MHz using a HB simulation.	82
33	Analysis of the branching phenomenon of the phase-coherent degenerate parametric amplifier at $f_s = 716$ MHz.	83
34	Stability analysis using pole-zero identification of the solution curves in Fig. 33.	85
35	Variation in the output power at f_s versus increasing source power level showing two possible solution curves that are dependent on the initial conditions of the phase-coherent degenerate parametric amplifier. . .	86
36	Solution curve for the phase-coherent negative-resistance degenerate parametric amplifier at $f_s = 650$ MHz.	86
37	Technology comparison of current state-of-the-art solid-state transconductance amplifiers to degenerate parametric amplifiers.	90
38	Technology comparison of phase-coherent upconverting parametric amplifiers to reported upconverting mixers with conversion gain.	92
39	Change in the pump port impedance as the source drive level increases. .	98

SUMMARY

The objective of this research is to develop, characterize, and demonstrate novel parametric architectures capable of wideband operation while maintaining high gain and stability. To begin the study, phase-incoherent upconverting parametric amplifiers will be explored by first developing a set of analytical models describing their achievable gain and efficiency. These models will provide a set of design tools to optimize and evaluate prototype circuit boards. The prototype boards will then be used to demonstrate their achievable gain, bandwidth, efficiency, and stability. Further investigation of the analytical models and data collected from the prototype boards will conclude bandwidth and gain limitations and end the investigation into phase-incoherent upconverting parametric amplifiers in lieu of negative-resistance parametric amplifiers.

Traditionally, there were two versions of negative-resistance parametric amplifiers available: degenerate and non-degenerate. Both modes of operation are considered single-frequency amplifiers because both the input and output frequencies occur at the source frequency. Degenerate parametric amplifiers offer more power gain than their non-degenerate counterpart and do not require additional circuitry for idler currents. As a result, a phase-coherent degenerate parametric amplifier printed circuit board prototype will be built to investigate achievable gain, bandwidth, and stability. Analytical models will be developed to describe the gain and efficiency of phase-coherent degenerate parametric amplifiers. The presence of a negative resistance suggests the possibility of instability under certain operating conditions, therefore, an in-depth stability study of phase-coherent degenerate parametric amplifiers will be performed.

The observation of upconversion gain in phase-coherent degenerate parametric amplifiers will spark investigation into a previously unknown parametric architecture: phase-coherent upconverting parametric amplifiers. Using the phase-coherent degenerate parametric amplifier prototype board, stable phase-coherent upconversion with gain will be demonstrated from the source input frequency to its third harmonic. An analytical model describing the large-signal transducer gain of phase-coherent upconverting parametric amplifiers from the first to the third harmonic of the source input will be derived and validated using the prototype board and simulations.

CHAPTER I

INTRODUCTION

In modern communication systems, the radio frequency (RF) transconductance power amplifier (PA) is responsible for the majority of the system's power consumption. When the PA is operating below 50% DC-DC efficiency, it is more an electrical heater than an amplifier, necessitating high power DC supplies and heat dissipation systems. Heat damage can wreak havoc on radar and satellite communication systems, demanding sophisticated cooling structures to protect not only the PA, but the surrounding electronics. With wireless communication systems, hand-held battery-operated mobile devices suffer the most from the PAs high power consumption, resulting in a decreased battery life and shorter talk time. Reported results on high efficiency PAs, typically operating above 75%, rely upon precise multi-harmonic impedance terminations on both the input and output terminals at very high levels of device compression, both of which results in highly nonlinear and narrow operating bandwidths [1, 2]. Power amplifier design has, until recently, been focused on specified RF bandwidths of 5% or less. Systems such as worldwide interoperability for microwave access (WiMAX) and 4G necessitate large instantaneous bandwidths, and future systems will likely require even more, not just due to wider spectral allocations, but the base bandwidth of the signals themselves may well exceed 100 MHz [3, 4]. In addition, radar and satellite communication systems have yet to benefit from recent improvements in PA output power and efficiency because of their much wider bandwidth requirements.

The need for PAs capable of achieving high gain and conversion efficiencies across a broad range of frequencies has fueled extensive previous research and development

of innovative power amplifier architectures. While primarily now an industry-driven field, broadband high gain and efficiency PA design still has a place in an academic setting as communication systems continue to push the limits of data rates in narrow channels.

1.1 High-Gain Single-Stage Power Amplifiers

High-gain transconductance power amplifiers are desirable in modern communication systems for their potential in single-stage designs that typically result in lower power consumption and higher conversion efficiencies. In field-effect transistor (FET) amplifiers, the gain of the device is directly proportional to the transconductance in the saturation region of operation. When operating in the active mode, the transconductance, g_m , can be expressed as

$$g_m = \frac{2I_D}{V_{GS} - V_{th}}, \quad (1.1)$$

where I_D is the drain current, V_{GS} is the gate-to-source voltage potential, and V_{th} is the threshold voltage. The threshold voltage of any particular FET device is considered to be a constant within the saturation region, therefore the transconductance of FET devices can be increased by increasing the drain current. In the saturation region, the drain current can be expressed as

$$I_D = \frac{\mu_n C_{ox}}{2} \frac{W}{L} (V_{GS} - V_{th})^2 (1 + \lambda V_{DS}), \quad (1.2)$$

where μ_n is the charge-carrier effective mobility, C_{ox} is the gate oxide capacitance per unit area, W is the gate width, L is the gate length, λ is the channel-length modulation parameter, and V_{DS} is the drain-to-source voltage potential [5]. Increasing the drain current, thereby increasing the transconductance, can be accomplished in

several ways as seen in (1.2), most of which are controllable through the fabrication process. However, care should be taken in choosing values for fabrication parameters, as pushing them to their limits can have negative, unintended consequences on the transconductance. Take, for instance, decreasing the channel length L in order to increase the small-signal transconductance. It was demonstrated in [6] that, for a given overdrive condition, velocity saturation of carriers in the channel due to short-channel effects will reduce the small-signal transconductance. This is by no means a complete description of the limiting phenomena in the small-signal transconductance; the reader is referred to [7] for a more in-depth analysis.

Current state-of-the-art transconductance devices report single-stage power amplifiers capable of over 23 dB of power gain within limited bandwidths at microwave frequencies using gallium nitride [8]. Typically, high-gain amplifiers are constructed using multiple stages or devices. This increases the current drain from the DC biasing supply, reducing the overall conversion efficiency. In addition, high-gain power amplifiers typically require precise input and output impedance control that reduces the operating bandwidth [1].

1.2 Conventional Power Amplifier Efficiency-Enhancement Techniques

Loosely, power amplifiers can be placed into two groups: linear and nonlinear. By the most rudimentary definition, a linear power amplifier is one when, given a single-tone sinusoidal input to the power amplifier, a single-tone sinusoid is seen at its output. While linearity is a highly desirable property in many modern communication systems, a stand-alone linear power amplifier will suffer from low conversion efficiency. Continued long-term low efficiency operation of a power amplifier can result in a decreased usable life time or damage to surrounding components due to heat generation. From an RF standpoint, a Class-A PA is considered to be a linear PA. Class-A operation is achieved by biasing the active device such that the drain quiescent current

is half of its maximum value, I_{max} , while maintaining an input drive level that does not force the drain current waveform to exceed I_{max} . Class-A power amplifiers have a theoretical maximum efficiency of 50%, achieved when the input drive level causes a swing in the drain current to peak at exactly I_{max} .

In contrast, a nonlinear power amplifier is one when, given a single-tone sinusoidal input, the output of the power amplifier contains harmonics of the input. Power amplifier architectures have been developed that will sacrifice linearity in order to increase the conversion efficiency by a considerable margin over their linear counterpart. Other architectures have demonstrated that waveform shaping of the output signal can produce efficient PAs with reasonable operating bandwidths.

One of the oldest ways of increasing the conversion efficiency of power amplifiers is to bias the active device to a quiescent current less than $\frac{I_{max}}{2}$. When considering optimal Class-A drive levels, the action of decreasing the quiescent current will cause part of the RF input drive waveform to dip below the threshold level for the active device, resulting in the negative portion of the input drive to not “conduct” to the output. These efficiency-enhancement architectures are therefore known as reduced conduction angle architectures.

To examine the effect of reducing the conduction angle by decreasing the quiescent current, usable definitions for efficiency must be defined. Traditionally, there are two main expressions which describe the conversion efficiency, η , of power amplifiers,

$$\eta = \frac{P_1}{P_{DC}} \tag{1.3}$$

$$\eta = \frac{P_1 - P_{in}}{P_{DC}}. \tag{1.4}$$

Equation (1.3), with respect to transconductance power amplifiers, is called the drain efficiency, where P_1 is the output power in the fundamental frequency, and P_{DC} is the

power being drawn from the DC supply. Equation (1.4) is referred to as the power-added efficiency since it takes into account the drive power, P_{in} , required to achieve maximum efficiency, which in most RF PA systems can be quite substantial. In both definitions of efficiency in (1.3) and (1.4), the conversion efficiency can be increased by reducing the DC power being drawn from the DC supply. In a typical PA system, the DC supply voltage will remain at a fixed voltage level, mandating a decrease in the DC current to achieve a reduction in P_{DC} . Following an analysis similar to that performed by Cripps in [9], it can be shown that the DC current will decrease as the conduction angle is reduced.

Let the drain current waveform be expressed as a sinusoidal function of the conduction angle α , such that

$$i_d(\theta) = I_q + I_{pk} \cos(\theta) \quad \frac{-\alpha}{2} < \theta < \frac{\alpha}{2}, \quad (1.5)$$

where $I_{pk} = I_{max} - I_q$ is the peak value of $i_d(\theta)$ and I_q is the quiescent current. By considering a cosine wave in (1.5), which is an even function, it is mathematically convenient to have α include the equal contributions from either side of time index zero of the conduction waveform. Under this assumption, the current cutoff points fall at $\omega t = \pm \frac{\alpha}{2}$, and $\cos\left(\frac{\alpha}{2}\right) = -\frac{I_q}{I_{pk}}$, so that

$$i_d(\theta) = \frac{I_{max}}{1 - \cos\left(\frac{\alpha}{2}\right)} \left(\cos(\theta) - \cos\left(\frac{\alpha}{2}\right) \right). \quad (1.6)$$

The average component of $i_d(\theta)$ can then be determined from

$$I_{DC} = \frac{1}{2\pi} \int_{-\frac{\alpha}{2}}^{\frac{\alpha}{2}} \frac{I_{max}}{1 - \cos\left(\frac{\alpha}{2}\right)} \left(\cos(\theta) - \cos\left(\frac{\alpha}{2}\right) \right) d\theta \quad (1.7)$$

$$= \left(\frac{I_{max}}{2\pi} \right) \left(\frac{2 \sin\left(\frac{\alpha}{2}\right) - \alpha \cos\left(\frac{\alpha}{2}\right)}{1 - \cos\left(\frac{\alpha}{2}\right)} \right). \quad (1.8)$$

Similarly, the magnitude of the fundamental output current can be determined from

$$I_1 = \frac{1}{\pi} \int_{-\frac{\alpha}{2}}^{\frac{\alpha}{2}} \frac{I_{max}}{1 - \cos\left(\frac{\alpha}{2}\right)} \left(\cos(\theta) - \cos\left(\frac{\alpha}{2}\right) \right) \cos(\theta) d\theta \quad (1.9)$$

$$= \left(\frac{I_{max}}{2\pi} \right) \left(\frac{\alpha - \sin(\alpha)}{1 - \cos\left(\frac{\alpha}{2}\right)} \right). \quad (1.10)$$

From (1.10), the RF fundamental output power is given by

$$P_1 = \frac{V_{DC} I_1}{2}. \quad (1.11)$$

Figure 1 shows a plot of the amplitude of (1.8) for a constant and normalized $I_{max} = 1$ as the conduction angle decreases from 2π to 0.

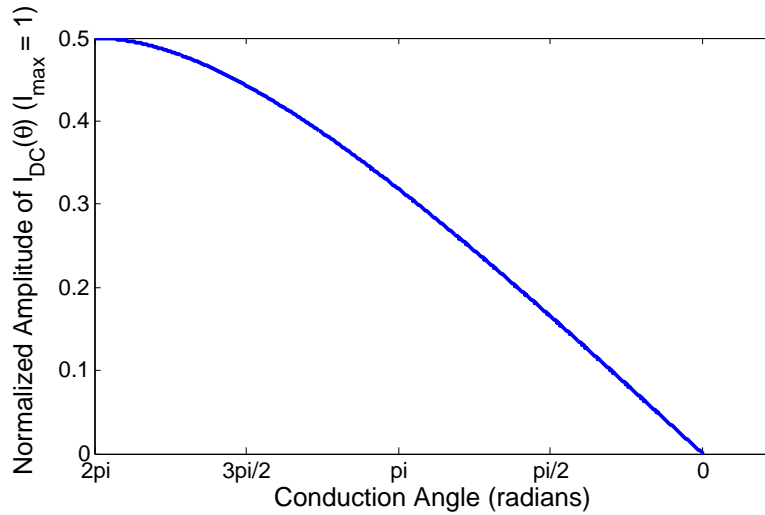


Figure 1: Plot of the amplitude of (1.8) for a constant and normalized $I_{max} = 1$ as the conduction angle decreases from 2π to 0.

As demonstrated in Fig. 1, the further the conduction angle is reduced, the less average current that is drawn from the DC supply, resulting in an increase in the overall conversion efficiency. However, this increase in efficiency comes with a trade

in not only linearity, but also in output power. Since the change in conduction angle from 2π to 0 causes a significant change in both linearity and output power, the total conduction angle range was divided up into classes of operation, each with a specified range of operating conduction angles with corresponding linearity and obtainable maximum efficiency specifications. The classical reduced conduction angle modes are: Class-A, Class-AB, Class-B, and Class-C.

1.2.1 Class-A Mode

As discussed above, Class A operation is obtained when the active device is biased such that the quiescent drain current is equal to half of the maximum drain current, I_{max} . The RF drive level is limited to cause a swing in the drain current that does not exceed its rails, ensuring maximum linearity and output power. Since the input drive levels are limited to maintaining constant active device conduction, the conduction angle of a Class-A amplifiers is 2π . Using (1.8), (1.10), and (1.3), the maximum obtainable efficiency of this class of operation is 50%.

1.2.2 Class-AB Mode

When transitioning to Class-AB mode, the bias point is reduced such that the drain current is below half of I_{max} , but above its zero threshold. With this restriction, the input drive waveform will experience clipping of the negative portion of its cycle, switching off the active device. This then allows less than 360 degrees, but more than 180 degrees, of the input drive waveform to conduct to the output, giving a range of possible conduction angles for Class-AB operation, θ_{AB} , to fall within $\pi < \theta_{AB} < 2\pi$. From Fig. 1, efficiency continues to increase as the conduction angle is decreased, therefore the highest obtainable efficiency for Class-AB operation occurs when the conduction angle approaches π radians. However, let us choose to examine the midpoint of the range of Class-AB mode conduction angles, where $\theta_{AB} = \frac{3\pi}{2}$.

Substitution into (1.8), (1.10), and (1.3) shows that when biased in “moderate” Class-AB mode, the amplifier will have a conversion efficiency of approximately 60%.

1.2.3 Class-B Mode

Class-B mode of operation is obtained when the bias point is set exactly to, or very close to, the threshold value for the active device, resulting in a drain quiescent current very near to zero. The RF input drive waveform will then symmetrically swing about the active device’s threshold level, resulting in half of the waveform, or π radians, conducting to the output. Application of (1.8), (1.10), and (1.3) to the Class-B mode of operation gives a maximum achievable conversion efficiency of 78.5%.

1.2.4 Class-C Mode

Continuing to decrease the bias point below the threshold value of the active device moves the mode of operation into Class-C. Here, only a portion of the positive cycle of the RF input drive waveform is conducted across the active device to the output. Here, the range of Class-C mode conduction angles, θ_C , falls within $0 < \theta_C < \pi$. As with the Class-AB mode of operation, biasing the active device closer to its lower-valued conduction angle increases the efficiency. However, in Class-C operation, this action would completely turn off the active device. Therefore, let us choose to examine the conversion efficiency of the Class-C mode when the conduction angle is at the midpoint of its valid range, namely, when $\theta_C = \frac{\pi}{2}$. Substitution of θ_C into (1.8), (1.10), and (1.3) shows an achievable conversion efficiency of approximately 94% when biased in “moderate” Class-C mode.

As briefly discussed above, the linearity of the active device decreases as the conduction angle is increased, therefore, as one progresses through each class mode, linearity is further traded for an increase in conversion efficiency. This can be seen from simple Fourier analysis of (1.6), where the magnitude of the harmonic currents increase with decreasing conduction angle [9].

Additional efficiency-enhancement architectures have been proposed for transconductance power amplifiers. When a PA system is well designed, the majority of the power loss resulting in sub-optimal conversion efficiency occurs in the active device itself. Time-domain analysis of the voltage and current waveforms across and through the active device show instances when they are simultaneously non-zero, indicating average power being absorbed. Ideally, to maximize the efficiency of these systems, the voltage and current waveforms would never coexist, meaning when one waveform is nonzero, the other must be identically zero, and vice versa. Then, the average power absorbed by the active device, being the product of the voltage and current waveforms, would be zero at all instantaneous values of time. Power amplifier architectures that exploit this concept are known as switching mode PA architectures [10, 11]. Efficiency-enhancement techniques such as the Doherty amplifier, envelope elimination and restoration, and polar modulation have also been identified and investigated [12–16].

1.3 Bandwidth Limitations in Transconductance Power Amplifiers

For transconductance power amplifiers, and by the Conservation of Power, the difference between the output power, P_o , and the input power, P_{in} , can never exceed the DC power, P_{DC} , being provided to the active device.

$$P_o - P_{in} \leq P_{DC} \quad (1.12)$$

In practice, the equality can never be obtain when considering physical losses in the linear circuitry surrounding the active device. The total input and output signal power can be expressed as an integral over their respective power spectral density functions. If $s(t)$ is the input signal as a function of time with $S(\omega)$ its corresponding

power spectral density (proportional to the squared modulus of the Fourier transform of $s(t)$), and if $G(\omega)$ is the power gain of the amplifier as a function of the frequency, ω , (1.12) can be rewritten as

$$\int G(\omega) S(\omega) d\omega - \int S(\omega) d\omega \leq P_{DC}, \quad (1.13)$$

or, equivalently,

$$\int [G(\omega) - 1] S(\omega) d\omega \leq P_{DC}, \quad (1.14)$$

where the integral is taken over the total bandwidth of G and S (or from 0 to infinity if the signals are not band-limited). When the amplifier gain is much greater than unity over its operational bandwidth, (1.14) can be approximated as

$$\int G(\omega) S(\omega) d\omega \leq P_{DC}. \quad (1.15)$$

Equation (1.15) is equivalent to neglecting the power of the input signal, which is a reasonable approximation if it is small relative to P_o . Now, suppose the amplifier operates over a bandwidth of BW , and assume that both the gain and the spectrum of the signal are constant over this entire bandwidth, with values of G and S , respectively. Under these conditions, (1.15) becomes

$$G \times BW \leq \frac{P_{DC}}{S}. \quad (1.16)$$

Equation (1.16) shows the origin of the gain-bandwidth product limit for transconductance amplifiers. The available DC power to the amplifier can either be put to use

for high signal gain over a limited bandwidth or limited gain over a wide bandwidth. Also note that for a fixed DC input power, the greatest signal gains are achieved with weak input signals.

1.4 Broadband High-Efficiency Parametric Architectures

Transconductance power amplifiers achieve power gain by converting DC to RF power through channel modulation of the active device. Since the efficiency-enhancement architectures described above operate by either reducing the average current drawn from the DC supply or eliminating the power loss associated with the active device, they are techniques that, in general, only apply to transconductance PAs. While DC-RF power amplifiers are currently the most implemented, they are but one of two possible ways to achieve amplification, the other being an RF to RF conversion of power. There are multiple ways to achieve RF-RF power conversion, but the focus of this section shall be on parametric power amplification.

Parametric amplifiers are a well-studied architecture of utilizing a nonlinear reactance to act as either a mixing element or a negative resistance [17–22]. Because parametric amplifiers make use of reactive elements, they were desirable for their low noise properties in low noise amplifiers before the invention of silicon-based transistors that were able to surpass parametric noise performance [23–26]. Because the noise characteristics of parametric power amplifiers was of primary interest, their efficiency and bandwidth performance was never extensively studied or modeled. Being a reactive-based active device, parametric power amplifiers should exhibit near perfect RF-RF conversion efficiencies. In addition, parametric systems should not suffer from the gain-bandwidth product that limits the usable bandwidth of transconductance PAs. These two observations make parametric systems very desirable for further investigation into their potential as a competitive power amplifier architecture to their transconductance counterpart.

1.5 Thesis Organization

This thesis is organized as follows. Chapter 2 details the theory of operation of the two traditional types of parametric amplifiers: phase-incoherent upconverting parametric amplifiers and negative-resistance parametric amplifiers. In addition, Chapter 2 will develop the Manley-Rowe relations and demonstrate their use in performance analysis of parametric amplifiers.

In Chapter 3, analytical models will be derived that will be able to predict the gain and efficiency of phase-incoherent upconverting parametric amplifiers, negative-resistance parametric amplifiers, and phase-coherent upconverting parametric amplifiers. The models will provide a circuit level description of the theoretical limitations of parametric systems, in addition to a set of tools to design the circuits to approach these limitations.

Chapter 4 utilizes the tools developed in Chapters 2 and 3 to design, synthesize, and test multiple parametric amplifiers, critiquing them on their achievable gain, bandwidth, and stability. Each system undergoes an in-depth analysis to explain any deviation from expected results.

Chapter 5 examines the stability of parametric amplifiers and provides a mathematical method to predict the operating conditions that might cause them to become unstable. The models developed in this chapter also provides a circuit design tool to ensure unconditional stability given a set of operating criteria.

Lastly, Chapter 6 concludes the thesis by comparing the performance of the parametric amplifiers developed in Chapter 4 to current state-of-the-art. A summary of the work performed, as well as key contributions of the research, is included. Suggestions for future work, as it relates to further development of parametric amplifiers, is discussed.

CHAPTER II

THEORY OF PARAMETRIC AMPLIFIERS

Parametric amplification is a process of RF-RF power conversion that operates by pumping a nonlinear reactance with a large-signal RF pumping source to either produce mixing products with gain or to generate a negative resistance. Parametric amplifiers (paramps) were traditionally grouped into two types: the phase-incoherent upconverting parametric amplifier and the negative-resistance parametric amplifier. With phase-incoherent upconverting parametric amplifiers, a fixed-frequency phase-incoherent incommensurate pump, at frequency f_p , mixes with an RF small-signal source input, at frequency f_s , to produce an upconverted output with gain that can be predicted by the Manley-Rowe relations [27, 28]. Negative-resistance parametric amplifiers are also mixers, but differ from phase-incoherent upconverting paramps in that the frequency relationship $f_i = f_p - f_s$ must be satisfied, where f_i is the so-called “idler” frequency [20]. The Manley-Rowe relations show that negative-resistance parametric amplifiers present a regenerative condition with the possibility of oscillation at both the source and idler frequencies.

2.1 The Manley-Rowe Relations

In 1956, J. M. Manley and H. E. Rowe published a manuscript that analyzed the power flow into and out of a nonlinear reactive element under excitation at its different harmonic frequencies [27]. The results of this analysis were two simple mathematical expressions quantifying how the total outgoing power flow would distribute itself among the harmonic terms. These two mathematical relationships, which will now be referred to as the Manley-Rowe relations, have the following important properties:

1. They are independent of the particular shape of the capacitance-voltage or inductance-current curve for a nonlinear capacitance or nonlinear inductance, respectively.
2. The power levels of the various driving sources are irrelevant.
3. The external circuitry connected to the nonlinear reactance will not affect how the power is distributed to the harmonic frequencies.

These two expressions provide information pertaining to the ideal performance metrics (such as gain and stability) of nonlinear reactance mixers and amplifiers without prior knowledge of the reactive devices or their surrounding circuitry. The simplicity of the Manley-Rowe relations, in addition to their wide applicability at a time when parametric architectures were being actively investigated, sparked multiple publications further exploring their use and validity in analytical modeling of parametric systems [29–33]. Because of the impact of the Manley-Rowe relations to parametric amplifiers, a shortened derivation will be presented here with an analysis of their applications to parametric amplifiers and mixers. The complete and detailed derivation performed by Manley and Rowe can be found in [27].

Manley and Rowe began their analysis by considering a circuit similar to that in Fig. 2. Figure 2 contains two voltage sources, V_1 and V_2 , at frequencies f_1 and f_2 , with their associated generator impedance, Z_o . These two voltage sources are electrically isolated from one another through ideal bandpass filters that are assumed to pass their indicated frequencies, and provide an open-circuit out-of-band. The two sources are placed across a nonlinear capacitance (though Manley and Rowe state that their derivation could have proceeded using a nonlinear inductance instead) whose capacitance, $C(V)$, is a function of its own terminal voltage V . In addition to the two voltage sources, an infinite number of resistive loads have been connected across the nonlinear capacitor, each electrically isolated from the rest of the circuit

by an ideal bandpass filter. The passband frequency of each load bandpass filter has been selected to correspond to a specific harmonic combination of the two driving frequencies, f_1 and f_2 , that occur because of the nonlinear mixing action of the nonlinear capacitance. Manley and Rowe made the assumption that the driving frequencies were incommensurate such that the ratio of the two will always satisfy

$$\frac{\omega_1}{\omega_2} \notin \mathbb{Q}. \quad (2.1)$$

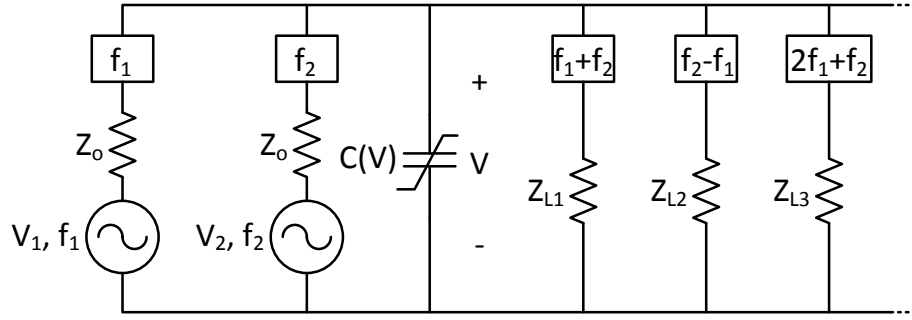


Figure 2: Simplified circuit model that Manley and Rowe considered for their derivation.

To begin the derivation, consider that the total charge, q , flowing into and out of the nonlinear capacitor in Fig. 2 can be expressed as a two-dimensional Fourier series as

$$q = \sum_{n=-\infty}^{\infty} \sum_{m=-\infty}^{\infty} q_{m,n} e^{j(m\omega_1 + n\omega_2)t}, \quad (2.2)$$

where the charge series coefficients, $q_{m,n}$, are expressed as

$$q_{m,n} = \frac{1}{4\pi^2} \int_{-\pi}^{\pi} \int_{-\pi}^{\pi} V \times C(V) e^{-j(mx+ny)} dx dy, \quad (2.3)$$

with $x = \omega_1 t$ and $y = \omega_2 t$. The total current, $I_{m,n}$, through $C(V)$ is the total time

derivative of the charge series coefficients,

$$I_{m,n} = \frac{dq_{m,n}}{dt} = \frac{\partial q_{m,n}}{\partial t} + \frac{\partial q_{m,n}}{\partial \omega_1} \frac{d\omega_1}{dt} + \frac{\partial q_{m,n}}{\partial \omega_2} \frac{d\omega_2}{dt}. \quad (2.4)$$

However, the incommensurability of ω_1 and ω_2 causes $\frac{\partial q_{m,n}}{\partial \omega_1} = \frac{\partial q_{m,n}}{\partial \omega_2} = 0$. As a result, (3.5) reduces to the partial time derivative of the charge series terms

$$I = \frac{\partial q}{\partial t} = \sum_{n=-\infty}^{\infty} \sum_{m=-\infty}^{\infty} I_{m,n} e^{j(m\omega_1 + n\omega_2)t} \quad (2.5)$$

$$I_{m,n} = j(m\omega_1 + n\omega_2) q_{m,n}. \quad (2.6)$$

The voltage across the nonlinear capacitor, V , may also be expressed as a two-dimensional Fourier series, just as was done with the charge,

$$V = \sum_{n=-\infty}^{\infty} \sum_{m=-\infty}^{\infty} V_{m,n} e^{j(m\omega_1 + n\omega_2)t}, \quad (2.7)$$

where the voltage series coefficients can be expressed as

$$V_{m,n} = \frac{1}{4\pi^2} \int_{-\pi}^{\pi} \int_{-\pi}^{\pi} V e^{-j(mx+ny)} dx dy. \quad (2.8)$$

It is at this point in their derivation that Manley and Rowe performed some mathematical “sleight-of-hand” in order to form products of $I_{m,n}$ and $V_{m,n}$ to obtain power series coefficients, $P_{m,n}$. The tricks employed by Manley and Rowe involves separating the problem into two parts, dealing first with frequencies at f_1 corresponding to index m , then next with frequencies at f_2 corresponding to index n , and do not need to be reproduced here; what is important is the result of this mathematical manipulation,

$$\sum_{m=-\infty}^{\infty} \sum_{n=-\infty}^{\infty} \frac{mV_{n,m}I_{n,m}^*}{mf_1 + nf_2} = \sum_{m=0}^{\infty} \sum_{n=-\infty}^{\infty} \frac{m2\Re\{V_{n,m}I_{n,m}^*\}}{mf_1 + nf_2} = \sum_{m=0}^{\infty} \sum_{n=-\infty}^{\infty} \frac{mP_{n,m}}{mf_1 + nf_2}, \quad (2.9)$$

where $P_{n,m}$ is the power flowing either into or out of the nonlinear capacitor at frequency $nf_1 + mf_2$. The desired result for the power flow through a nonlinear reactance is thus, by Conservation of Energy,

$$\sum_{m=0}^{\infty} \sum_{n=-\infty}^{\infty} \frac{mP_{n,m}}{mf_1 + nf_2} = 0. \quad (2.10)$$

When concerned with the evaluation of the power flow in a nonlinear reactance with respect to index n , a second result can be obtained.

$$\sum_{n=0}^{\infty} \sum_{m=-\infty}^{\infty} \frac{nP_{n,m}}{mf_1 + nf_2} = 0 \quad (2.11)$$

Equations (2.10) and (2.11) are known as the Manley-Rowe relations.

As discussed above, the Manley-Rowe relations are independent of the shape of the capacitance-voltage or inductance-current curve of the nonlinear reactance and the nature of the surrounding circuitry, assuming proper isolation of driving and harmonic currents. As a result, the Manley-Rowe relations provide a way to quantify the idealized metrics of parametric systems, such as gain and stability, and thus a figure of merit to evaluate the performance of circuit designs.

To illustrate this concept, let the voltage generator $V1$ in Fig. 2 be a small-signal input source, and $V2$ be a large-signal pumping source that is required to drive the nonlinear action of the nonlinear capacitor. Consider that power is allowed to flow out of the nonlinear reactance at a frequency $f_3 = f_1 + f_2$. Then (2.10) and (2.11) reduce to

$$\frac{P_1}{f_1} + \frac{P_3}{f_3} = 0 \quad (2.12)$$

$$\frac{P_2}{f_2} + \frac{P_3}{f_3} = 0. \quad (2.13)$$

To satisfy Conservation of Energy, we will define power flowing into the nonlinear capacitance as positive, and power flowing out of the nonlinear capacitance as negative. By rearranging (2.12) and (2.13), a gain expression can be obtained that is the ratio of output power to input power when power extracted at f_3 is considered to be the desired output term.

$$\text{gain} = \frac{f_3}{f_1} \quad (2.14)$$

Equation (2.14) demonstrates that given both lossless components and ideal harmonic isolation and terminations the maximum gain that is achievable when using a parametric circuit to upconvert a signal from a frequency f_1 to a frequency f_3 is the ratio of the upconverted frequency to the input frequency.

Conversely, let the signal frequency be equal to the sum of the desired output harmonic and the pumping frequency, such that now the signal frequency is f_3 , the desired output frequency is f_1 , and the pumping frequency remains at f_2 . In this case, the parametric circuit is downconverting the input signal to a lower frequency and the Manley-Rowe relations predict the maximum achievable gain will be

$$\text{gain} = \frac{f_1}{f_3}, \quad (2.15)$$

which will always be less than one, or a loss. These two examples are by no means

a complete listing of the applicability of the Manley-Rowe relations. These relations have also been used extensively in laser and fiber optic research [34–37].

The constraint of incommensurate frequencies imposed by Manley and Rowe in their derivation was challenged by Anderson and Someda [31, 32]. Their claim stems from reports of physically realized parametric circuits properly acting as upconverting parametric amplifiers when the ratio of the input to upconverted frequencies does not satisfy (2.1). When the driving generators are modeled as ideal, such that their driving voltage can be expressed as $V = V_o e^{j\omega t}$, then the constraint of incommensurate frequencies is necessary. However, nonideal physical generators cannot produce a discrete line spectrum. That is to say, the instantaneous output frequency of a physical generator is approximately ω , and will average out to ω over a sufficiently long time interval. The voltage of this physical generator could then be modeled as $V = V_o e^{j(\omega t + \phi)}$, where ϕ is some arbitrary phase that varies slowly over time with a mean value of zero. It is then arguable that the Manley-Rowe relations should be clarified to state that the instantaneous frequencies should be ‘almost always’ incommensurate. Anderson demonstrated that in the statistical case when the frequencies become commensurate, ensuring phase incoherence of the driving sources maintains the validity of the Manley-Rowe relations.

2.2 Phase-Incoherent Upconverting Parametric Amplifiers

Three general properties define the operation of phase-incoherent upconverting parametric amplifiers: the output frequency is equal to the sum of the input source frequency and the pump frequency, power is allowed to flow only at the source, pump, and output frequencies, and the source and pump waveforms must maintain phase incoherence. As (2.14) demonstrated, the maximum upconverting gain is the ratio of the output frequency to the input frequency, and is achievable only when harmonic

isolation is perfect and circuit components are ideal. In any physically realizable upconverting parametric amplifier, circuit component losses and leakage currents due to nonideal filters introduce mechanisms that limit approaching the ideal Manley-Rowe gain.

In an effort to better understand the operating characteristics of the phase-incoherent upconverting parametric amplifier, and to determine the primary circuit parameters responsible for decreasing the gain from the Manley-Rowe limit, Blackwell and Kotzebue considered a quasi-idealized circuit and developed an expression for the transducer gain of phase-incoherent upconverting parametric amplifiers based on the quality factor of the nonlinear reactance, frequencies of operation, and resistive terminations [38]. To continue their work in identifying gain-limiting circuit and component characteristics, a similar circuit was explored, taking into account the capacitance range of the nonlinear capacitor.

Consider the circuit in Fig. 3 that contains an input small-signal source at frequency f_s and a large-signal pumping source at frequency f_p interacting with a voltage-dependent nonlinear capacitor, $C(v)$. Filters are in place to electrically isolate currents at the source and pump frequencies from the desired output mixing product $f_o = f_p + f_s$.

Assuming that the pump voltage is several orders in magnitude larger than the source, the voltage across the reactive nonlinearity is dominated by the pump such that the voltage-dependent nonlinear capacitor can be considered a time-varying capacitance with frequency ω_p ,

$$C(t) = C_o (1 + 2M \cos \omega_p t), \quad (2.16)$$

where M is proportional to the pump voltage and gives the coupling between the voltages at the two angular frequencies ω_s and ω_p , and C_o is the large-signal average

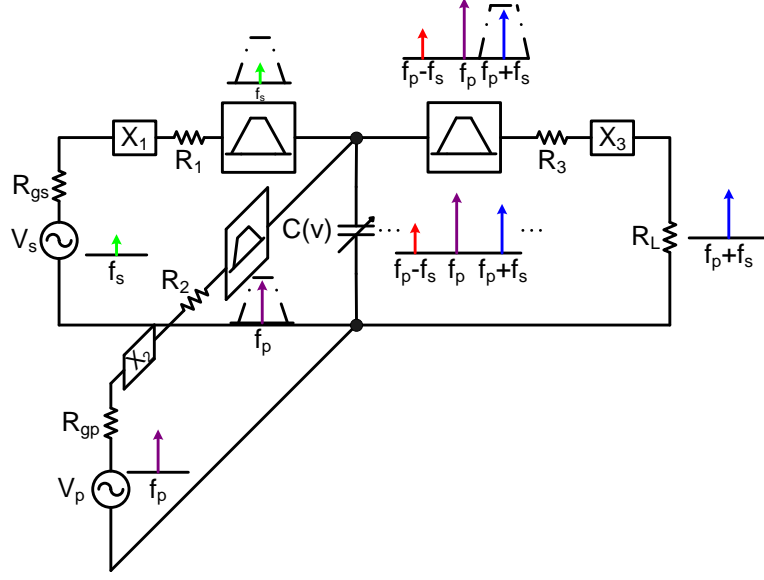


Figure 3: A phase-incoherent upconverting parametric amplifier.

capacitance of the nonlinear capacitor. Performing a derivation similar to Manley and Rowe, the power series coefficients can be expressed as

$$P_{n,m} = |I_{n,m}|^2 Z_{n,m}, \quad (2.17)$$

where $I_{n,m}$ and $Z_{n,m}$ are the current and impedance Fourier series coefficients of the nonlinear capacitance, respectively, and can mathematically be represented by

$$Z_{n,m} = \frac{1}{j(n\omega_s + m\omega_p) C_o (1 + 2M \cos y)} \quad (2.18)$$

$$q_{n,m} = \frac{1}{4\pi^2} \int_{-\pi}^{\pi} \int_{-\pi}^{\pi} (V_{dc} + V_s \cos x + V_p \cos y) \times C_o (1 + 2M \cos y) e^{-j(nx+my)} dx dy \quad (2.19)$$

$$I_{n,m} = \frac{\partial q_{n,m}}{\partial t}, \quad (2.20)$$

where $q_{n,m}$ are the charge series coefficients, $y = \omega_p t$ and $x = \omega_s t$. For a phase-incoherent upconverting parametric amplifier, the power terms of interest are $P_{1,1}$, the power in the upconverted output signal, and $P_{1,0}$, the power in the source signal. Evaluation of (2.17) results in

$$\frac{P_{1,1}}{P_{1,0}} = G_o = \frac{\omega_s + \omega_p}{\omega_s} M^2 = \frac{\omega_o}{\omega_s} M^2. \quad (2.21)$$

As we approach ideal conditions, M approaches unity, and we obtain the optimal gain predicted by Manley and Rowe.

Let us now assume that the time-dependent capacitance described by (2.16) is piecewise-linear, such that a sinusoidal excitation results in a sinusoidal change in capacitance. Let us also assume that the nonlinear capacitor's quality factor is sufficiently large such that its effects on the gain are negligible. Under these two assumptions, the coupling factor M can be treated as a constant and written as a direct function of the reactive nonlinearity's maximum and minimum capacitance, respectively C_{max} and C_{min} .

$$M = \frac{C_{max} - C_{min}}{C_{max}} \quad (2.22)$$

Substitution of (2.22) into (2.21) results in

$$G_o = \frac{\omega_o}{\omega_s} \underbrace{\left(1 - 2 \left(\frac{C_{max}}{C_{min}} \right)^{-1} + \left(\frac{C_{max}}{C_{min}} \right)^{-2} \right)}_1. \quad (2.23)$$

Equation (2.23) represents the maximum obtainable small-signal gain given the available change in the reactive nonlinearities capacitance. This expression is limited

to predicting only small-signal gain because of the assumption of a piecewise-linear capacitance-voltage curve. Term 1 in (2.23) can be considered a gain-degradation factor. Figure 4 shows the change in this gain-degradation factor with changing maximum-to-minimum capacitance ratio.

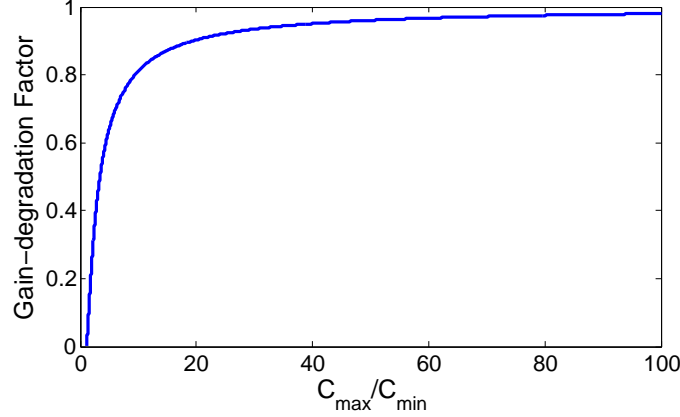


Figure 4: Change in term 1 in (2.23) with changing maximum-to-minimum nonlinear capacitance ratio.

From Fig. 4 it is clear that when assuming negligible circuit and component losses the gain of phase-incoherent upconverting parametric amplifiers approaches the Manley-Rowe limit as the nonlinear capacitor's available maximum-to-minimum capacitance ratio increases.

The bandwidth of phase-incoherent upconverting parametric amplifiers can be discussed if a couple of assumptions are first made. With respect to Fig. 3, the construction of the source, pump, and output filters was never specified. To determine a general expression for the bandwidth, these filters will each be comprised of high-Q series L-C resonant circuits. While single-tuned resonant circuits do not yield the maximum bandwidth, they do reduce the overall complexity of both the analysis and the corresponding mathematics.

In [20], Blackwell and Kotzbue approached the bandwidth of phase-incoherent upconverting parametric amplifiers in a similar manner. Their derivation showed that

when a phase-incoherent upconverting parametric amplifier is optimized for maximum gain, the operating bandwidth, b , will be limited by

$$b \leq \frac{2}{Q_s}, \quad (2.24)$$

where Q_s is the loaded quality factor of the source L-C series resonant filter.

2.3 Negative-Resistance Parametric Amplifiers

Consider now the situation where power flows into the nonlinear reactance at both the small-signal source frequency and the large-signal pump frequency, and power flows out of the nonlinear reactance at the desired output, which is the difference between the pump and source frequency, $f_o = f_p - f_s$. In this case, the Manley-Rowe relations reduce to

$$\frac{P_o}{f_o} + \frac{P_p}{f_p} = 0 \quad (2.25)$$

$$\frac{P_s}{f_s} + \frac{P_p}{f_p} = 0. \quad (2.26)$$

Maintaining the power flow convention that positive power flows into the nonlinear reactance and negative power flows out, P_p must be positive. Therefore, to satisfy the equalities in (2.25) and (2.26), both P_s and P_o must be negative. That is, the nonlinear reactance is delivering power to the source signal generator at frequency f_s instead of absorbing power from it. If the gain of this system were to be defined as the ratio of power delivered to the source input from the nonlinear reactance to that being provided to the nonlinear reactance from the source input, then it is possible for infinite gain to occur, as (2.25) and (2.26) demonstrate that the nonlinear reactance is capable of delivering power to the source at frequency f_s whether or not the source

input is active. The possibility of infinite gain suggests the potential for system instability at both f_s and f_o , however, when stable, this type of parametric amplifier has properties which differentiates it from the phase-incoherent upconverting parametric amplifier, and is known as a negative-resistance parametric amplifier. There are two modes of operation for negative-resistance parametric amplifiers: nondegenerate and degenerate.

Both degenerate and nondegenerate negative-resistance parametric amplifiers are considered single-frequency amplifiers since the input and output frequencies both occur at f_s . In addition, both modes satisfy the equality

$$f_o = f_p - f_s, \quad (2.27)$$

but since the output frequency is identical to the source frequency, two possibilities exist to fulfill (2.27). The first is when power flow is allowed to occur at a third frequency known as the “idler,” f_i , such that $f_i = f_p - f_s$. In this case, the amplifier is designed so that the idler current is contained within the nonlinear reactance and is never delivered to a real load. By doing so, (2.27) is satisfied without the idler affecting the gain or efficiency of the amplifier. The second case is when the pump frequency is exactly twice that of the source, such that $f_i = f_p - f_s = 2f_s - f_s = f_s$. In the second case, the source and pump frequencies are harmonically related and the phase relationship between them directly affects amplifier performance.

2.3.1 Nondegenerate Negative-Resistance Parametric Amplifiers

Parametric amplifiers that satisfy (2.27) and $f_o = f_i \neq f_s$ are known as nondegenerate negative-resistance parametric amplifiers. The gain of these amplifiers is a function of the negative resistance that is created through the interaction of the source and

pumping waves within the nonlinear reactance. Therefore, by determining an expression for the negative resistance of nondegenerate parametric amplifiers, an expression for the gain follows.

To begin the derivation, consider the nondegenerate parametric amplifier in Fig. 5. Figure 5 contains a small-signal current source, $i_s(t)$, and a large-signal pumping source, $i_p(t)$, each with their respective generator conductances G_s and G_p . The load conductance, G_L , is located within the source circuit. Each independent source is electrically isolated from the other through the use of the high-Q resonant traps $L_s - C_s$ and $L_p - C_p$. The idler current is limited to circulate within the nonlinear capacitor, $C(v)$, through the use of the high-Q resonant trap $L_i - C_i$ such that no power is dissipated at that frequency.

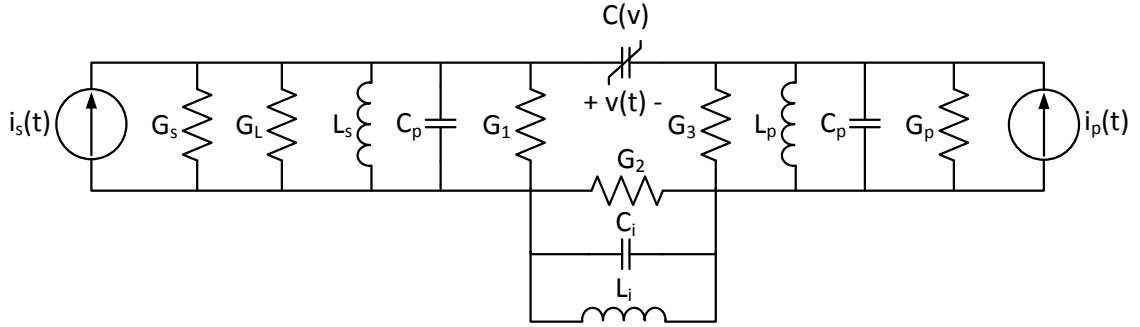


Figure 5: An equivalent circuit of a nondegenerate negative-resistance parametric amplifier.

Under the assumption that the sum of the source and pump voltage amplitudes are much smaller than the DC operating point, the charge, q , stored on the plates of the nonlinear capacitor can be expanded in a Taylor series about the DC operating point. If only the linear and quadratic terms are sufficient size to consider in the expansion, then q can be written as

$$q = a_1 v(t) + a_2 v^2(t), \quad (2.28)$$

where $v(t)$ represents the total voltage across the nonlinear capacitor at frequencies f_s , f_p , and f_i ,

$$v(t) = V_s \cos(\omega_s t + \phi_s) + V_i \cos(\omega_i t + \phi_i) + V_p \cos(\omega_p t + \phi_p), \quad (2.29)$$

and a_1 and a_2 are the Taylor series coefficients. V_s , V_i , and V_p in (2.29) are the peak values of the harmonic voltages making up the total voltage waveform $v(t)$. The linear term a_1 in the expansion in (2.28) must be well-defined, for to ensure high electrical isolation between source, idler, and pump currents, each resonant trap must satisfy

$$\omega_s = \frac{1}{\sqrt{L_s (C_s + a_1)}} \quad (2.30)$$

$$\omega_i = \frac{1}{\sqrt{L_i (C_i + a_1)}} \quad (2.31)$$

$$\omega_p = \frac{1}{\sqrt{L_p (C_p + a_1)}}. \quad (2.32)$$

With knowledge of the total charge stored on the plates of the nonlinear capacitor, the current passing through the nonlinear capacitor, $i_{NLC}(t)$, can be found from the nonlinear capacitor's C-V characteristics and the total voltage across its terminals.

$$i_{NLC}(t) = \frac{dq(v(t))}{dv(t)} \frac{dv(t)}{dt} = C(v(t)) \frac{dv(t)}{dt} = a_1 \frac{dv(t)}{dt} + 2a_2 v(t) \frac{dv(t)}{dt} \quad (2.33)$$

By substituting (2.29) into (2.33), expanding the result and grouping terms of similar frequency, the total current passing through the nonlinear capacitor can be expressed as

$$i_{NLC}(t) = i_s(t) + i_i(t) + i_p(t), \quad (2.34)$$

where

$$i_s(t) = -\omega_s a_1 V_s \sin(\omega_s t + \phi_s) - \omega_s a_2 V_i V_p \sin(\omega_s t + \phi_p - \phi_i) \quad (2.35)$$

$$i_i(t) = -\omega_i a_1 V_i \sin(\omega_i t + \phi_i) - \omega_i a_2 V_s V_p \sin(\omega_i t + \phi_p - \phi_s) \quad (2.36)$$

$$i_p(t) = -\omega_p a_1 V_p \sin(\omega_p t + \phi_p) - \omega_p a_2 V_s V_i \sin(\omega_p t + \phi_s + \phi_i). \quad (2.37)$$

Equations (2.35), (2.36), and (2.37) can now be rewritten as

$$i_s(t) = a_1 \frac{dv_s(t)}{dt} + \frac{a_2 V_i V_p}{V_s} \left[\cos(\phi_p - \phi_i - \phi_s) \frac{dv_s(t)}{dt} - \omega_s v_s(t) \sin(\phi_p - \phi_i - \phi_s) \right] \quad (2.38)$$

$$i_i(t) = a_1 \frac{dv_i(t)}{dt} + \frac{a_2 V_s V_p}{V_i} \left[\cos(\phi_p - \phi_i - \phi_s) \frac{dv_i(t)}{dt} - \omega_i v_i(t) \sin(\phi_p - \phi_i - \phi_s) \right] \quad (2.39)$$

$$i_p(t) = a_1 \frac{dv_p(t)}{dt} + \frac{a_2 V_s V_i}{V_p} \left[\cos(\phi_p - \phi_i - \phi_s) \frac{dv_p(t)}{dt} + \omega_p v_p(t) \sin(\phi_p - \phi_i - \phi_s) \right]. \quad (2.40)$$

Taking the Fourier transform of (2.38), (2.39), and (2.40) and dividing each by their respective transformed voltage $\tilde{\mathbf{V}}_s$, $\tilde{\mathbf{V}}_i$, and $\tilde{\mathbf{V}}_p$, the admittance of the nonlinear capacitor is obtained at the source, idler, and pump frequencies, $\tilde{\mathbf{Y}}_s$, $\tilde{\mathbf{Y}}_i$, and $\tilde{\mathbf{Y}}_p$, respectively.

$$\tilde{\mathbf{Y}}_s = \frac{\tilde{\mathbf{I}}_s(j\omega)}{\tilde{\mathbf{V}}_s(j\omega)} = j\omega_s a_1 + j\omega_s a_2 \frac{V_i V_p}{V_s} e^{j(\phi_p - \phi_i - \phi_s)} \quad (2.41)$$

$$\tilde{\mathbf{Y}}_i = \frac{\tilde{\mathbf{I}}_i(j\omega)}{\tilde{\mathbf{V}}_i(j\omega)} = j\omega_i a_1 + j\omega_i a_2 \frac{V_s V_p}{V_i} e^{j(\phi_p - \phi_i - \phi_s)} \quad (2.42)$$

$$\tilde{\mathbf{Y}}_p = \frac{\tilde{\mathbf{I}}_p(j\omega)}{\tilde{\mathbf{V}}_p(j\omega)} = j\omega_p a_1 + j\omega_p a_2 \frac{V_s V_i}{V_p} e^{-j(\phi_p - \phi_i - \phi_s)} \quad (2.43)$$

With the aid of (2.41), (2.42), and (2.43) and the circuit in Fig. 5, the current-voltage relationships for the source, idler, and pump circuits can be expressed as

$$\tilde{\mathbf{I}}_s(\mathbf{j}\omega) = \left(G_T + j\omega_s a_2 \frac{V_i V_p}{V_s} e^{j(\phi_p - \phi_i - \phi_s)} \right) \tilde{\mathbf{V}}_s(\mathbf{j}\omega) \quad (2.44)$$

$$0 = \left(G_2 + j\omega_i a_2 \frac{V_s V_p}{V_i} e^{j(\phi_p - \phi_i - \phi_s)} \right) \tilde{\mathbf{V}}_i(\mathbf{j}\omega) \quad (2.45)$$

$$\tilde{\mathbf{I}}_p(\mathbf{j}\omega) = \left(G_3 + j\omega_p a_2 \frac{V_s V_i}{V_p} e^{-j(\phi_p - \phi_i - \phi_s)} \right) \tilde{\mathbf{V}}_p(\mathbf{j}\omega), \quad (2.46)$$

where $G_T = G_s + G_L + G_1$. Applying the resonance conditions of (2.30), (2.31), and (2.32) and substituting (2.45) and (2.46) into (2.44) to eliminate V_i and V_p allows the admittance looking into the source current driver, $\tilde{\mathbf{Y}}_{\text{source}}$, to be expressed in the following manner.

$$\tilde{\mathbf{Y}}_{\text{source}} = G_T - \frac{\omega_s \omega_i a_2^2}{G_2 G_3^2} \frac{|\tilde{\mathbf{I}}_p(\mathbf{j}\omega)|^2}{\left(1 + \frac{\omega_i \omega_p}{G_2 G_3} a_2^2 V_s^2 \right)^2} = G_T - G \quad (2.47)$$

The small-signal transducer gain, g_t , of the circuit in Fig. 5 can now be determined as

$$g_t = \frac{G_L V_s^2}{\frac{|I_s|^2}{4G_s}} = \frac{4G_s G_L}{|\tilde{\mathbf{Y}}_{\text{source}}|^2}. \quad (2.48)$$

By truncating the Taylor series expansion of the charge stored on the plates of the nonlinear capacitor in (2.28), (2.48) will be unable to accurately predict the gain of the amplifier under large-signal operating conditions.

2.3.2 Phase-Coherent Degenerate Negative-Resistance Parametric Amplifiers

With degenerate negative-resistance parametric amplifiers, the pump frequency is exactly twice that of the source such that the condition of (2.27) reduces to $f_i = f_s$. Thus, in degenerate mode of operation, there is no need for a separate high-Q resonant trap to contain the idler, reducing the complexity of the circuit model of Fig. 5 to that of Fig. 6.

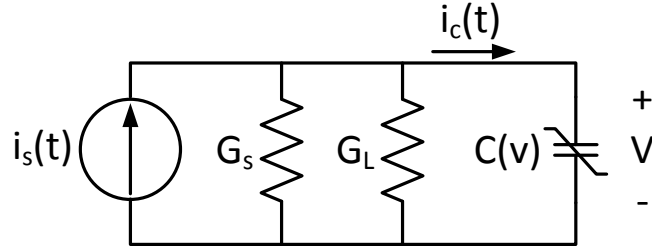


Figure 6: An equivalent circuit of a degenerate negative-resistance parametric amplifier. The pump circuit has been omitted, however, its effects have been included in the definition of $C(t)$ in (2.49). The parallel resonant traps have also been omitted by assuming on-resonance operating conditions.

The pump circuit has been omitted from Fig. 6. This is because the nonlinear capacitor's change in capacitance is dominated by the pump voltage swing, therefore the pump circuit can be absorbed into the nonlinear capacitor's model, such that it is now a time-varying capacitance with frequency $\omega_p = 2\omega_s$.

$$C(v_p(t)) = C(t) = 2MC_o \sin(2\omega_s t + \phi_p), \quad (2.49)$$

where M denotes the coupling between the source and pump voltages, and C_o is the large-signal average capacitance of the nonlinear capacitor. Defining

$$v = V_s \sin(\omega_s t + \phi_s) \quad (2.50)$$

and substituting (2.49) and (2.50) into the definition of the current passing through a nonlinear capacitor from (2.33), the total current can be expressed as

$$i_c(t) = -\omega_s M C_o V_s \sin(\omega_s t + \phi_p - \phi_s). \quad (2.51)$$

Applying Kirchoff's Current Law, the source generator current, $i_s(t)$, is

$$i_s(t) = V_s (G_s + G_L) \sin(\omega_s t + \phi_s) - \omega_s M C_o V_s \sin(\omega_s t + \phi_p - \phi_s). \quad (2.52)$$

The small-signal transducer gain, g_t , is then given by

$$g_t = \frac{4G_s G_L V_s^2}{|\tilde{\mathbf{I}}_s \tilde{\mathbf{I}}_s^*|} = \frac{4G_s G_L}{(G_s + G_L)^2 \underbrace{[1 + \beta^2 - 2\beta \cos(2\phi_s - \phi_p)]}_1}, \quad (2.53)$$

where

$$\tilde{\mathbf{I}}_s = V_s (G_s + G_L) e^{j\phi_s} - \omega_s M C_o V_s e^{j(\phi_p - \phi_s)} \quad (2.54)$$

is the Fourier transform of (2.52), and

$$\beta = \frac{\omega_s M C_o}{G_s + G_L}. \quad (2.55)$$

Equation (2.53) will be unable to predict large-signal gain because of the linear approximation of the change in nonlinear capacitance in (2.49). Term 1 in (2.53) acts to increase the transducer gain and is phase-dependent. This is a consequence of the

harmonic relationship between the pump and source frequencies, namely, $\omega_p = 2\omega_s$. The maximum transducer gain occurs when $2\phi_s = \phi_p$ and will then take on the value

$$g_{t,max} = \frac{4G_s G_L}{(G_s + G_L)^2 (1 - \beta)^2}. \quad (2.56)$$

Similar to parametric upconverters, the operating bandwidth of negative-resistance parametric amplifiers will depend on the form of the filtering necessary to isolate the pump, source, and idler currents. Both Figs. 5 and 6 make use of high-Q parallel resonant L-C filters and as a result the bandwidth will be primarily limited by the loaded quality factor of these circuits. Blackwell and Kotzbue approached the problem of the bandwidth of negative-resistance parametric amplifiers by assuming single-tuned resonant structures, and determined that the gain-bandwidth product can be written approximately as

$$g^{1/2}b = \frac{1}{Q_l}, \quad (2.57)$$

where Q_l is the loaded quality factor of the amplifier resonant circuit.

CHAPTER III

ANALYTICAL MODELING OF PARAMETRIC AMPLIFIERS

The theory in Chapter 2 focused on the gain and bandwidth of parametric amplifiers from a quasi-idealistic circuit standpoint. Because of the use of quasi-idealistic circuit models in Chapter 2, the derived expressions offer little aid in the design process of physical parametric systems. By considering more complex, nonidealized circuits, analytical models can be developed that describe power gain, gain-compression, and RF-RF conversion efficiency. These analytical models provide not only a more in-depth understanding of the mechanisms that limit gain, efficiency, and bandwidth of parametric amplifiers, but also contribute a design tool for error correction and optimization of parametric systems.

3.1 Phase-Incoherent Parametric Upconverting Amplifiers

The derivation performed by Manley and Rowe demonstrated the ideal mathematical relationship that exists between the mixing products of a nonlinear reactive element under excitation. Their relationships came as a result of the assumptions of incommensurable and periodic excitation signals. Under these two assumptions, it was never necessary for Manley and Rowe to solve the two-dimensional Fourier integrals for the mixing term coefficients. In doing so, and with a proper circuit model for the nonlinear reactance, analytical models can be developed describing the non-ideal achievable gain and efficiency of a parametric upconverter.

Varactor diodes, when operating well below their self-resonance frequency, can be modeled as a series variable resistance, $R_s(v)$, and nonlinear capacitance, $C(v)$, both

a function of the varactor's terminal voltage [22]. In the following derivation, it will be assumed that the change in $R_s(v)$ with respect to the terminal voltage is minimal (assuming reverse bias operation) and can be treated as a constant to a first-order approximation. It was demonstrated in [39] that the capacitive change in the varactor can be approximated as a linear function of the terminal voltage, $C(v) = c_0 + c_1 v$, where c_0 is dependent on the bias voltage, and c_1 is some constant of units Farads per volt. In the particular instance of high gain parametric amplifiers, the pump voltage is several orders of magnitude greater than the source, and dominates the terminal voltage such that $C(v)$ can be expressed as a time-varying sinusoidal function with frequency ω_p ,

$$C(v) = c_0 + c_1 v \Big|_{v=V_p \cos \omega_p t} \approx C_o (1 + 2M \cos \omega_p t) = C(t), \quad (3.1)$$

where M is proportional to the pump voltage and gives the coupling between the voltages at the two angular frequencies ω_s and ω_p , and C_o is the average large-signal capacitance [40]. Let the charge, q , stored on $C(t)$ be a single-valued function of the terminal voltage $v = V_{DC} + V_s \cos \omega_s t + V_p \cos \omega_p t$. The charge can be expressed as a Taylor series in v to obtain

$$q = q(0) + \frac{\partial q}{\partial v} v + \frac{1}{2} \frac{\partial^2 q}{\partial v^2} v^2 + \cdots, \quad (3.2)$$

where all derivatives are evaluated at $v = V_{DC}$. Since all powers of v exist in (3.2), the frequencies of the charge coefficients will span $\{f_s, f_p\}$. Thus, the frequencies of the current coefficients also spans $\{f_s, f_p\}$, and the voltage developed across $C(t)$ contains information on all possible mixing products. Consequently, the charge can be represented as a two-dimensional Fourier series,

$$q = \sum_{n=-\infty}^{\infty} \sum_{m=-\infty}^{\infty} q_{n,m} e^{j(n\omega_s + m\omega_p)t}, \quad (3.3)$$

where the charge series coefficients, $q_{n,m}$, are expressed as

$$q_{n,m} = \frac{1}{4\pi^2} \int_{-\pi}^{\pi} \int_{-\pi}^{\pi} (V_{DC} + V_s \cos x + V_p \cos y) \\ \times C_o (1 + 2M \cos y) e^{-j(nx+my)} dx dy, \quad (3.4)$$

with $x = \omega_s t$ and $y = \omega_p t$. The total current, $I_{n,m}$, through $C(t)$ is the total time derivative of the charge series coefficients,

$$I_{n,m} = \frac{dq_{n,m}}{dt} = \frac{\partial q_{n,m}}{\partial t} + \frac{\partial q_{n,m}}{\partial \omega_s} \frac{d\omega_s}{dt} + \frac{\partial q_{n,m}}{\partial \omega_p} \frac{d\omega_p}{dt}. \quad (3.5)$$

However, the initial assumption of the incommensurability of ω_s and ω_p causes $\frac{\partial q_{n,m}}{\partial \omega_s} = \frac{\partial q_{n,m}}{\partial \omega_p} = 0$. As a result, (3.5) reduces to the partial time derivative of the charge series terms

$$I = \frac{\partial q}{\partial t} = \sum_{n=-\infty}^{\infty} \sum_{m=-\infty}^{\infty} I_{n,m} e^{j(n\omega_s + m\omega_p)t} \quad (3.6)$$

$$I_{n,m} = j(n\omega_s + m\omega_p) q_{n,m}. \quad (3.7)$$

The frequencies of the impedance coefficients $Z_{n,m}$, as with the current coefficients, will span $\{f_s, f_p\}$ in the Fourier domain. The representation of $C(t)$ in (3.1), while a good mathematical model for the time-dependent change in capacitance, is a result of large-signal excitation. Thus, (3.1) must be linearized about V_{DC} and can be accurately approximated by C_o to obtain the varactor impedance series terms

$$Z_{n,m} = R_s + \frac{1}{j(n\omega_s + m\omega_p)C_o}. \quad (3.8)$$

Two-dimensional Fourier synthesis can now be used to express the complex power, P , of the varactor,

$$P = \sum_{n=-\infty}^{\infty} \sum_{m=-\infty}^{\infty} P_{n,m} e^{j(n\omega_s + m\omega_p)t} \quad (3.9)$$

$$P_{n,m} = |I_{n,m}|^2 Z_{n,m}. \quad (3.10)$$

Evaluation of (3.10) for the ratio of $P_{1,1}$ to $P_{1,0}$ results in

$$G_o = \frac{P_{1,1}}{P_{1,0}} = \underbrace{\frac{\omega_o}{\omega_s}}_1 \underbrace{M^2}_2 \underbrace{\frac{1 + jC_o R_s \omega_o}{1 + jC_o R_s \omega_s}}_3. \quad (3.11)$$

We are interested in both the real and reactive power being provided by the varactor, such that (3.11) can be written as $G_o = \Re\{G_o\} + j\Im\{G_o\} = G_r + jG_i$. Separating the real and reactive terms in (3.11) yields

$$G_r = \frac{\omega_o}{\omega_s} M^2 \frac{Q_s}{Q_o} \frac{Q_s Q_o + 1}{Q_s^2 + 1} \quad (3.12)$$

$$G_i = \frac{\omega_o}{\omega_s} M^2 \frac{Q_s}{Q_o} \frac{Q_s - Q_o}{Q_s^2 + 1}, \quad (3.13)$$

where

$$Q_s = \frac{1}{\omega_s R_s C_o} \quad (3.14)$$

$$Q_o = \frac{1}{\omega_o R_s C_o}. \quad (3.15)$$

In (3.1) it was assumed that the varactor's capacitance was piecewise-linear, as in Fig. 7, to describe $C(t)$ as sinusoidal. Making the same assumption, the coupling factor M in term 2 in (3.11) can be treated as a constant and written as a direct function of the change in capacitance experienced under RF excitation at a specified amplitude.

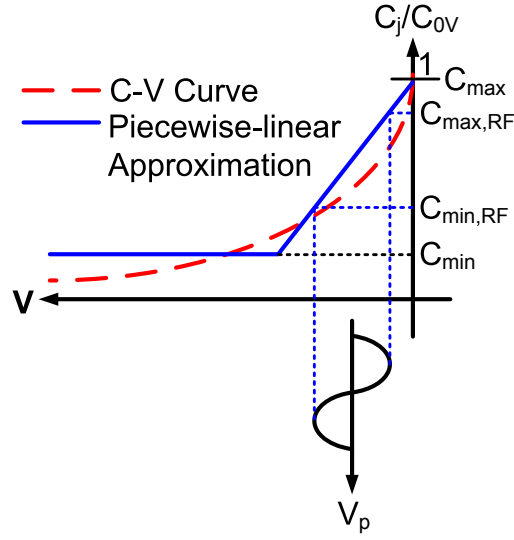


Figure 7: Piecewise-linear approximation of the square-law region of the varactor junction capacitance, as normalized to its maximum value at 0V bias, versus ideal characteristics. This figure demonstrates the difference between the varactors maximum available change in capacitance, as opposed to that observed under RF drive.

$$M = \frac{C_{max,RF} - C_{min,RF}}{C_{max,RF}} \quad M \in (0, 1) \quad (3.16)$$

Substitution of (3.16) into (3.12) and (3.13) provides a complete description of the achievable real and reactive gain of a phase-incoherent upconverting parametric amplifier.

$$G_r = \underbrace{\frac{\omega_o}{\omega_s}}_1 \underbrace{\left(1 - \frac{C_{min,RF}}{C_{max,RF}}\right)^2 \left(\frac{Q_s}{Q_o} \frac{Q_s Q_o + 1}{Q_s^2 + 1}\right)}_2 \quad (3.17)$$

$$G_i = \frac{\omega_o}{\omega_s} \left(1 - \frac{C_{min,RF}}{C_{max,RF}}\right)^2 \left(\frac{Q_s}{Q_o} \frac{Q_s - Q_o}{Q_s^2 + 1}\right) \quad (3.18)$$

Manley and Rowe predict the maximum achievable real power gain of any phase-incoherent upconverting parametric amplifier to be $\frac{\omega_o}{\omega_s}$. Therefore, term 2 in (3.17) can be considered a gain-degradation factor, and

$$\lim_{\frac{C_{max,RF}}{C_{min,RF}}, Q_s, Q_o \rightarrow \infty} G_r = \frac{\omega_o}{\omega_s}, \quad (3.19)$$

as predicted by Manley and Rowe under ideal conditions. Conversely,

$$\lim_{\substack{\frac{C_{max,RF}}{C_{min,RF}} \rightarrow 1 \\ \frac{Q_s}{Q_o} \rightarrow 0}} G_r = 0. \quad (3.20)$$

For any appreciable value of Q_s and Q_o , the last term in (3.17) is approximately equal to 1. Gain-degradation is therefore dominated by the change in capacitance in the varactor. Let

$$\gamma = \frac{Q_s}{Q_o} \frac{Q_s Q_o + 1}{Q_s^2 + 1} \quad \gamma \in [0, 1]. \quad (3.21)$$

Then, $G_r = f\left(\frac{C_{max,RF}}{C_{min,RF}}, \gamma\right)$. Figure 8 shows a family of isolines of the gain-degradation term of (3.17) with $\gamma = 0.1, 0.5$ and 1.

The reactive power gain gives a measure of the mismatch between the varactor and the load. An ideal varactor will deliver all available real power to the load and all reactive power should be reflected back to the varactor; the reactive gain G_i should be zero. Let

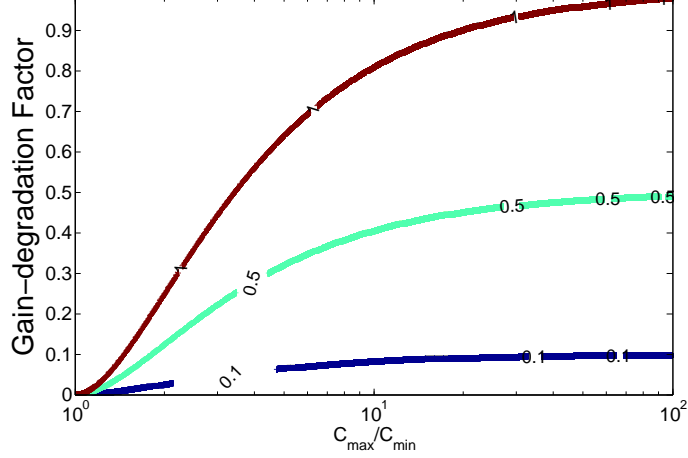


Figure 8: Plot of the change in the gain-degradation factor versus varactor capacitance ratio with $\gamma = 0.1, 0.5$ and 1 .

$$\beta = \frac{Q_s}{Q_o} \frac{Q_s - Q_o}{Q_s^2 + 1}. \quad (3.22)$$

Then $G_i = f\left(\frac{C_{max,RF}}{C_{min,RF}}, \beta\right)$. Under ideal conditions, it can be seen that

$$\lim_{\substack{\frac{C_{max,RF}}{C_{min,RF}} \rightarrow \infty \\ \beta \rightarrow 0}} G_i = 0. \quad (3.23)$$

Equations (3.17) and (3.18) do not include higher order terms that would account for the strong nonlinear effects of gain compression. Therefore, predicting gain-degradation is limited to the linear region of the AM-AM distortion curve and will begin to deviate from measured results as the output power begins to saturate.

The derivation of the achievable efficiency of a phase-incoherent upconverting parametric amplifier proceeds similar to that just performed for the gain and will not be presented with as much detail. There are multiple ways to define system efficiency of phase-incoherent upconverting parametric amplifiers, however one should avoid solving the Manley-Rowe relations for the ratio of the power in the upconverted

$$\eta_r = \frac{M^2 Q_p Q_s V_s^2 \omega_o \left[(1 + Q_o Q_p) Q_s (2MV_{DC} + V_p)^2 \omega_p + Q_p (1 + Q_o Q_s) V_s^2 \omega_s \right]}{Q_o \left[(1 + Q_p^2) Q_s^2 (2MV_{DC} + V_p)^4 \omega_p^2 + 2Q_p Q_s (1 + Q_p Q_s) (2MV_{DC} + V_p)^2 V_s^2 \omega_p \omega_s + Q_p^2 (1 + Q_s^2) V_s^4 \omega_s^2 \right]} \quad (3.27)$$

$$\eta_i = \frac{M^2 Q_p Q_s V_s^2 \omega_o \left[(Q_o - Q_p) Q_s (2MV_{DC} + V_p)^2 \omega_p + Q_p (Q_o - Q_s) V_s^2 \omega_s \right]}{Q_o \left[(1 + Q_p^2) Q_s^2 (2MV_{DC} + V_p)^4 \omega_p^2 + 2Q_p Q_s (1 + Q_p Q_s) (2MV_{DC} + V_p)^2 V_s^2 \omega_p \omega_s + Q_p^2 (1 + Q_s^2) V_s^4 \omega_s^2 \right]} \quad (3.28)$$

output to that of the pump, as it results in an equation that predicts an efficiency greater than 100%. The power in the upconverted output must be the sum of the source and pump powers P_s and P_p , respectively, as required by Conservation of Power for a lossless reactance.

$$P_o = P_s + P_p \quad (3.24)$$

For this reason, an accurate way to represent the system efficiency, η , is

$$\eta = \frac{P_o}{P_s + P_p} \quad (3.25)$$

that guarantees the maximum obtainable efficiency under ideal conditions is 100%; this is effectively equivalent to power-added efficiency for transconductance amplifiers. For system efficiency, the power series coefficients given in (3.10) are still valid. In the definition of efficiency presented in (3.25), it can be shown that

$$\eta = \frac{M^2 V_s^2 \omega_o (Q_o^{-1} - j)}{(2MV_{DC} + V_p)^2 \omega_p (Q_p^{-1} - j) + V_s^2 \omega_s (Q_s^2 - j)}. \quad (3.26)$$

As with gain, both the real and imaginary components of (3.26) are of interest. Equation (3.27) shows the real component of the efficiency, and (3.28) the imaginary component, such that $\eta = \eta_r + j\eta_i$.

Equations (3.27) and (3.28) cannot be simplified in such a way to contain an efficiency-degradation term as was done with the maximum gain. However, functional analysis of (3.27) and (3.28) can be used to confirm the correctness of the derivation. Under ideal conditions, $Q_o, Q_p, Q_s \rightarrow \infty$ and $M \rightarrow 1$. As a result,

$$\lim_{\substack{M \rightarrow 1 \\ Q_{s,p,o} \rightarrow \infty}} \eta_r = \frac{V_s^2 \omega_o}{(2V_{DC} + V_p)^2 \omega_p + V_s^2 \omega_s}. \quad (3.29)$$

In (3.1) it was assumed that $V_p \gg V_s$. Consequently, let $V_s = 0$ and equate (3.29) to 1 being the maximum obtainable efficiency. Then,

$$(2V_{DC} + V_p)^2 \omega_p = 0. \quad (3.30)$$

There is only one solution to the quadratic in (3.30): $V_p = -2V_{DC}$. With reference to Fig. 7, selecting a bias point in the middle of the linear approximation to the square-law region and allowing a symmetric swing in V_p equal to twice the bias voltage ensures that the varactor will experience its available C_{max} to C_{min} ratio. In addition, the terminal voltage of the varactor will exceed its built-in potential, forcing saturated operating conditions. This confirms the derivational necessity of the varactor experiencing its maximum change in terminal capacitance and suggests that driving the phase-incoherent upconverting parametric amplifier into saturation may maximize the efficiency. Conversely,

$$\lim_{\substack{M \rightarrow 0 \\ Q_{s,p,o} \rightarrow 0}} \eta_r = 0. \quad (3.31)$$

The reactive component of the efficiency provides a measure of the reflective mismatch between the varactor and the load. In the ideal case, the parasitic self-resistance of

the varactor goes to zero and the quality factor at all frequencies of operation is infinite.

$$\lim_{Q_{s,p,o} \rightarrow \infty} \eta_i = 0 \quad (3.32)$$

It is difficult to determine the dominant terms in (3.27) with uncertainty in its independent variables using a graphical means as was performed with the gain analytical model. Instead, first-order variable sensitivity analysis can be employed to examine the uncertainty of the efficiency analytical model. The first-order sensitivity of a dependent function f with respect to independent variable x is defined as [41]

$$S_x^f = \frac{\partial f}{\partial x} \frac{x}{f}. \quad (3.33)$$

Evaluation of S_x^f at a typical operating point demonstrated the general sensitivity of the efficiency analytical model showing the per unit change in η with a per unit change in Q_o , Q_p , Q_s , and M was insignificant if all are sufficiently large. The sensitivity of η is dominated by the uncertainty in V_s , V_{DC} , and V_p as expected with the choice of initial assumptions. A practical efficiency analytical model is thus described in (3.34).

$$\eta_r \approx \frac{V_s^2 \omega_o}{(2V_{DC} + V_p)^2 \omega_p + V_s^2 \omega_s} \quad (3.34)$$

Similar to the gain analytical model, the efficiency analytical model is limited to predicting system efficiency in backed-off operating conditions only. Equation (3.34) does not include higher order terms and as a result cannot compensate for saturated operating conditions.

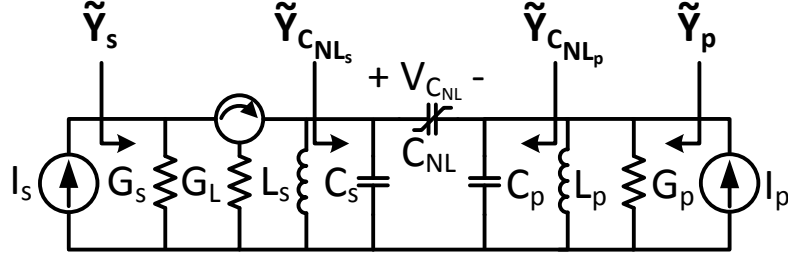


Figure 9: A degenerate parametric amplifier utilizing a nonlinear capacitance. The circulator, $L_s - C_s$, and $L_p - C_p$ electrically isolate the output, source, and pump currents, respectively, from one another.

3.2 Phase-Coherent Degenerate Parametric Amplifiers

Consider the circuit in Fig. 9 that shows the basic architecture of degenerate parametric amplifiers. The circuit contains a nonlinear capacitance (NLC) whose junction capacitance is a function of its own terminal voltage, $V_{C_{NL}}$. Source and pump currents are electrically isolated from one another through the high-Q parallel resonant combinations $L_s - C_s$ and $L_p - C_p$ that resonate at ω_s and ω_p , respectively. It is assumed that the circulator's ideal scattering matrix is

$$\begin{bmatrix} S \end{bmatrix}_{\text{circulator}} = \begin{bmatrix} 0 & 0 & 1 \\ 1 & 0 & 0 \\ 0 & 1 & 0 \end{bmatrix} \quad (3.35)$$

for any impedance combination presented to the circulator allowing it to direct incident and reflected waves without affecting their magnitude and phase. This assumption provides for an exploration of the effect of impedance mismatch between only the NLC and G_s , G_p , and G_L in degenerate paramps.

The NLC can be modeled in a Taylor series about some neighborhood of its DC operating point, V_{DC} , as

$$C_{NL}(V) = a + b(V_{C_{NL}} - V_{DC}), \quad (3.36)$$

where a and b are the Taylor series coefficients with units F and F/V , respectively. In a degenerate parametric amplifier, voltage potentials at only frequencies ω_s and ω_p need to be present across the terminals of the NLC to generate the negative resistance responsible for power amplification. Therefore, if all unwanted harmonic voltages across the terminals of the NLC are properly shorted,

$$\begin{aligned} v_{C_{NL}}(t) &= \frac{V_p}{2} \left(e^{j(2\omega_s t + \phi_p - \frac{\pi}{2})} + e^{-j(2\omega_s t + \phi_p - \frac{\pi}{2})} \right) \\ &+ \frac{V_s}{2} \left(e^{j(\omega_s t + \phi_s - \frac{\pi}{2})} + e^{-j(\omega_s t + \phi_s - \frac{\pi}{2})} \right), \end{aligned} \quad (3.37)$$

where V_s and V_p are the peak amplitude values of the voltage waveforms at ω_s and ω_p , respectively, across the terminals of the NLC. It is necessary to consider an initial phase displacement of 90 degrees lagging in (3.37) if the NLC is to properly present a negative resistance. It was demonstrated in [42] that the time-varying currents through a NLC can be determined from the time-varying voltage applied to its terminals by

$$i_{C_{NL}}(t) = C_{NL}(v_{C_{NL}}(t)) \frac{\partial v_{C_{NL}}(t)}{\partial t}. \quad (3.38)$$

By substituting (3.36) and (3.37) into (3.38) and expanding, collecting terms at ω_s and ω_p , bringing the solution over to the positive frequency spectrum, and dividing the terms at ω_s by $V_s e^{j\omega_s t + \phi_s}$ and the terms at ω_p by $V_p e^{2j\omega_s t + \phi_p}$, equivalent admittances for the NLC are obtained at both ω_s and ω_p .

$$\tilde{\mathbf{Y}}_{\mathbf{C}_{\text{NLs}}} = \omega_s \left(ja - \frac{be^{j(\phi_p - 2\phi_s)}V_p}{2} \right) \quad (3.39)$$

$$\tilde{\mathbf{Y}}_{\mathbf{C}_{\text{NLp}}} = \omega_s \left(2ja + \frac{be^{j(2\phi_s - \phi_p)}V_s^2}{2V_p} \right) \quad (3.40)$$

Using (3.39) and (3.40), and applying Euler's formula to each complex exponential, the total admittance seen by the source and pump generators, $\tilde{\mathbf{Y}}_{\mathbf{s}}$ and $\tilde{\mathbf{Y}}_{\mathbf{p}}$, can be expressed as

$$\begin{aligned} \tilde{\mathbf{Y}}_{\mathbf{s}} &= G_s - \frac{\omega_s b V_p}{2} \cos(\phi_p - 2\phi_s) \\ &+ j \left(\frac{\omega_s b V_p}{2} \sin(\phi_p - 2\phi_s) + \omega_s a \right) \end{aligned} \quad (3.41)$$

$$\begin{aligned} \tilde{\mathbf{Y}}_{\mathbf{p}} &= G_p + \frac{\omega_s b V_s^2}{2V_p} \cos(2\phi_s - \phi_p) \\ &+ j \left(\frac{\omega_s b V_s^2}{2V_p} \sin(2\phi_s - \phi_p) + 2\omega_s a \right). \end{aligned} \quad (3.42)$$

Equations (3.41) and (3.42) reveal that the phase relationship $\phi_p = 2\phi_s$ must exist if both the negative conductance is to be maximized and the excess nonlinear reactance (which results from pumping the NLC) is to be minimized.

To ensure that the phase condition stated above is satisfied, the linear susceptance terms $j\omega_s a$ and $2j\omega_s a$ in $\tilde{\mathbf{Y}}_{\mathbf{s}}$ and $\tilde{\mathbf{Y}}_{\mathbf{p}}$, respectively, must be properly eliminated through resonance. This can be accomplished if the values for L_s and L_p in Fig. 9 fulfill

$$L_s = \frac{1}{\omega_s^2 (C_s + a)}, \text{ and } L_p = \frac{1}{4\omega_s^2 (C_p + 2a)}. \quad (3.43)$$

Then, (3.41) and (3.42) can be substituted into the other such that each is now a function of its own peak terminal voltage V_s or V_p .

$$\tilde{\mathbf{Y}}_s = G_s - \frac{\omega_s b I_p}{2G_p} + \frac{(\omega_s b V_s)^2}{4G_p} \quad (3.44)$$

$$\tilde{\mathbf{Y}}_p = G_p + \frac{2bI_s^2}{V_p(\omega_s b V_p - 2G_s)^2} \quad (3.45)$$

Equations (3.44) and (3.45) show that the circuit in Fig. 9 can be modeled as two separate equivalent circuits from the viewpoints of the source current generator and the pump current generator.

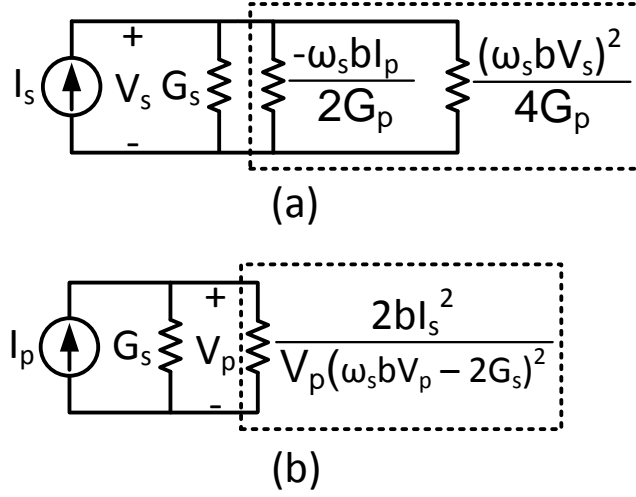


Figure 10: Equivalent circuits of the degenerate parametric amplifier in Fig. 9 as seen by (a) the source current generator, and (b) the pump current generator.

Now, from (3.44) and Fig. 10, an expression for the transducer gain, g_t , can be derived.

$$g_t(P_L) = \frac{8G_s \left(\underbrace{\frac{\omega_s b I_p}{2G_p}}_1 - \underbrace{\frac{(\omega_s b)^2}{2G_L G_p} P_L}_2 \right)^2}{G_L \left(\underbrace{G_s - \frac{\omega_s b I_p}{2G_p}}_3 + \underbrace{\frac{(\omega_s b)^2}{2G_L G_p} P_L}_4 \right)^2} \quad (3.46)$$

Equation (3.46) reveals the mechanism of gain compression in phase-coherent degenerate parametric amplifiers. If the available source power level, $P_{s,av} = \frac{I_s^2}{8G_s}$, is increased, and all other variables in (3.46) remain constant, then terms 2 and 4 increase in magnitude and eventually become comparable in magnitude to terms 1 and 3. This results in a nonlinear decrease in the power delivered to the load causing amplitude modulation distortion of the output. When considering backoff operating conditions, terms 2 and 4 in (3.46) can be ignored and the linear transducer gain, $g_{t,lin}$, can be determined to be

$$g_{t,lin} = \frac{2G_s (\omega_s b I_p)^2}{G_L G_p^2 \left(G_s - \frac{\omega_s b I_p}{2G_p} \right)^2}. \quad (3.47)$$

The RF-RF conversion efficiency of phase-coherent degenerate parametric amplifiers can also be explored. Consider the expression for the total admittance seen by the pump current generator, $\tilde{\mathbf{Y}}_{\mathbf{p}}$, in (3.42). By applying the phase condition $\phi_p = 2\phi_s$, $\tilde{\mathbf{Y}}_{\mathbf{p}}$ can be simplified to a useful expression involving both the source and pump voltage amplitudes V_s and V_p .

$$\tilde{\mathbf{Y}}_{\mathbf{p}} = G_p + \frac{\omega_s b V_s^2}{2V_p G_s} \quad (3.48)$$

This new expression for $\tilde{\mathbf{Y}}_{\mathbf{p}}$ provides an equivalent circuit from the perspective of the pump current generator, as seen in Fig. 11.

If it is assumed that G_p is close in value to $\frac{\omega_s b V_s^2}{2V_p G_s}$ then the peak voltage V_p can be approximated as

$$V_p = \frac{I_p}{2G_p}. \quad (3.49)$$

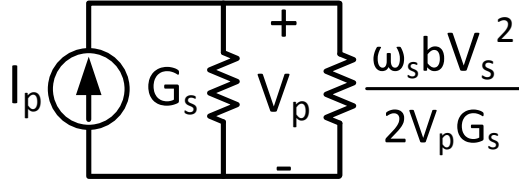


Figure 11: Equivalent circuit as seen by the pump current generator according to (3.48).

From (3.48) and (3.49), the available pump power can be expressed as

$$P_{p,av} = \frac{I_p \omega_s b P_L}{8 G_p G_L}, \quad (3.50)$$

where $P_L = \left(\frac{V_s}{\sqrt{2}}\right)^2 G_L$. By defining the RF-RF conversion efficiency as the ratio of output power to available pump power, the efficiency of negative-resistance parametric amplifiers can be expressed as

$$\eta = \frac{P_L}{P_{p,av}} = \frac{8 G_p G_L}{I_p \omega_s b}. \quad (3.51)$$

3.3 Phase-Coherent Upconverting Parametric Amplifiers

Phase-coherent upconverting parametric amplifiers combine traits from both phase-incoherent upconverting parametric amplifiers and phase-coherent negative-resistance parametric amplifiers. With phase-coherent upconverting parametric amplifiers, the source and pump frequencies are commensurate (as with degenerate parametric amplifiers), but the output is taken at a harmonic (greater than the first) of the source frequency. In this way, phase-coherent upconverting parametric amplifiers mix the source input up to a higher harmonic with gain through the action of a negative resistance.

In the development of the Manley-Rowe relations in (2.10) and (2.11), the authors

explicitly maintained the incommensurability of the two mixing frequencies f_1 and f_2 . The validity of the Manley-Rowe relations when dealing with commensurate frequencies f_1 and f_2 was challenged in [31] and [32], and concluded that they are still valid when the two frequencies are commensurate, however, the two signals must maintain phase incoherence. The imposition of phase incoherence in no way restricts a new mathematical exploration of the possibility of a phase-coherent upconverting parametric amplifier.

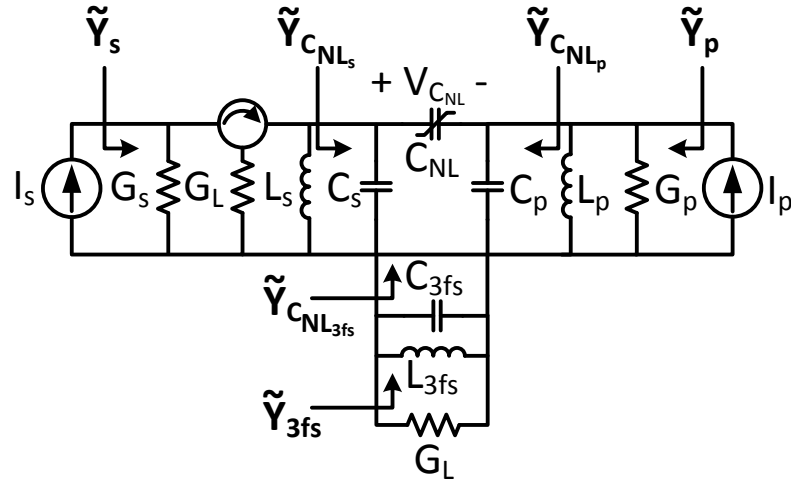


Figure 12: Idealized equivalent circuit for a phase-coherent upconverting parametric amplifier utilizing a nonlinear capacitance. The circulator, $L_s - C_s$, $L_p - C_p$, and $L_{3fs} - C_{3fs}$ electrically isolate the source, pump, and output currents, respectively, from one another.

Consider the circuit in Fig. 12 that shows the basic architecture of a phase-coherent upconverting parametric amplifier designed to upconvert to three times the source frequency when $\omega_p = 2\omega_s$. The circuit contains a nonlinear capacitor whose capacitance is a function of its own terminal voltage, $V_{C_{NL}}$. Source, pump, and upconverted output currents are electrically isolated from one another through the high-Q parallel resonant combinations $L_s - C_s$, $L_p - C_p$, and $L_{3fs} - C_{3fs}$ that resonate at ω_s , ω_p , and ω_{3fs} , respectively. It is assumed that the circulator's ideal scattering matrix is

$$\begin{bmatrix} S \end{bmatrix}_{\text{circulator}} = \begin{bmatrix} 0 & 0 & 1 \\ 1 & 0 & 0 \\ 0 & 1 & 0 \end{bmatrix} \quad (3.52)$$

for any impedance combination presented to the circulator allowing it to direct incident and reflected waves without affecting their magnitude and phase. This assumption provides for an exploration of the effect of impedance mismatch between only the NLC and G_s , G_p , and G_L in phase-coherent upconverting parametric amplifiers.

The NLC can be modeled in a Taylor series about some neighborhood of its DC operating point, V_{DC} , as

$$C_{NL}(V) = a + b(V_{C_{NL}} - V_{DC}), \quad (3.53)$$

where a and b are the Taylor series coefficients with units F and F/V , respectively. In a phase-coherent upconverting parametric amplifier, voltage potentials at only frequencies ω_s , ω_p , and ω_{3fs} need to be present across the terminals of the NLC to generate the negative resistance responsible for power amplification at the third harmonic. Therefore, if all unwanted harmonic voltages across the terminals of the NLC are properly shorted,

$$\begin{aligned} v_{C_{NL}}(t) &= \frac{V_p}{2} \left(e^{j(2\omega_s t + \phi_p - \frac{\pi}{2})} + e^{-j(2\omega_s t + \phi_p - \frac{\pi}{2})} \right) \\ &+ \frac{V_s}{2} \left(e^{j(\omega_s t + \phi_s - \frac{\pi}{2})} + e^{-j(\omega_s t + \phi_s - \frac{\pi}{2})} \right) \\ &+ \frac{V_{3fs}}{2} \left(e^{j(3\omega_s t + \phi_{3fs} - \frac{\pi}{2})} + e^{-j(3\omega_s t + \phi_{3fs} - \frac{\pi}{2})} \right), \end{aligned} \quad (3.54)$$

where V_s , V_p , and V_{3fs} are the peak amplitude values of the voltage waveforms at ω_s , ω_p , and ω_{3fs} , respectively, across the terminals of the NLC. It is necessary to

consider an initial phase displacement of 90 degrees lagging in (3.54) if the NLC is to properly present a negative resistance. It was demonstrated in [42] that the time-varying currents through a NLC can be determined from the time-varying voltage applied to its terminals by

$$i_{C_{NL}}(t) = C_{NL}(v_{C_{NL}}(t)) \frac{\partial v_{C_{NL}}(t)}{\partial t}. \quad (3.55)$$

By substituting (3.53) and (3.54) into (3.55) and expanding, collecting terms at ω_s , ω_p , and ω_{3fs} , bringing the solution over to the positive frequency spectrum, and dividing the terms at ω_s by $V_s e^{j\omega_s t + \phi_s}$, the terms at ω_p by $V_p e^{2j\omega_s t + \phi_p}$, and the terms at ω_{3fs} by $V_{3fs} e^{3j\omega_s t + \phi_{3fs}}$, equivalent admittances for the NLC are obtained at ω_s , ω_p , and ω_{3fs} .

$$\tilde{\mathbf{Y}}_{\mathbf{C}_{\text{NLs}}} = \omega_s \left[ja - \frac{bV_p}{2} \left(e^{j(\phi_p - 2\phi_s)} + e^{j(\phi_{3fs} - \phi_p - \phi_s)} \frac{V_{3fs}}{V_s} \right) \right] \quad (3.56)$$

$$\tilde{\mathbf{Y}}_{\mathbf{C}_{\text{NLp}}} = \omega_s \left[2ja + \frac{bV_s}{2V_p} \left(e^{j(2\phi_s - \phi_p)} V_s - 2e^{j(\phi_{3fs} - \phi_p - \phi_s)} V_{3fs} \right) \right] \quad (3.57)$$

$$\tilde{\mathbf{Y}}_{\mathbf{C}_{\text{NL3fs}}} = \omega_s \left[3ja + \frac{3bV_s V_p e^{j(\phi_s + \phi_p - \phi_{3fs})}}{2V_{3fs}} \right] \quad (3.58)$$

Using (3.56), (3.57), and (3.58), imposing the phase relationships $\phi_p = 2\phi_s$ and $\phi_{3fs} = 3\phi_s$, and selecting the resonance combinations $L_s - C_s$, $L_p - C_p$, and $L_{3fs} - C_{3fs}$ such that

$$L_s = \frac{1}{\omega_s^2 (C_s + a)} \quad (3.59)$$

$$L_p = \frac{1}{4\omega_s^2 (C_p + 2a)} \quad (3.60)$$

$$L_{3fs} = \frac{1}{9\omega_s^2 (C_{3fs} + 3a)}, \quad (3.61)$$

to eliminate the linear susceptance terms $j\omega_s a$, $2j\omega_s a$, and $3j\omega_s a$ from (3.56), (3.57), and (3.58), respectively, the total admittance seen by the source and pump generators, $\tilde{\mathbf{Y}}_s$, $\tilde{\mathbf{Y}}_p$, and $\tilde{\mathbf{Y}}_{3fs}$ can be expressed as

$$\tilde{\mathbf{Y}}_s = G_s - \frac{\omega_s b V_p}{2} \left(1 + \frac{V_{3fs}}{V_s} \right) \quad (3.62)$$

$$\tilde{\mathbf{Y}}_p = G_p + \underbrace{\frac{\omega_s b V_s}{2 V_p} (V_s - 2 V_{3fs})}_1 \quad (3.63)$$

$$\tilde{\mathbf{Y}}_{3fs} = \frac{3\omega_s b V_s V_p}{2 V_{3fs}}. \quad (3.64)$$

Assuming that term 1 in (3.63) is matched to G_p , V_p can be approximated as $V_p = \frac{I_p}{2G_p}$. Using (3.62) and the approximation of V_p to eliminate V_s and V_p from (3.64), the peak current passing through the nonlinear capacitor in Fig. 12 at the third harmonic is

$$I_{3fs} = \frac{3\omega_s b I_p (4G_p I_s + \omega_s b I_p V_{3fs})}{16G_p^2 G_s}. \quad (3.65)$$

From (3.65), it can then be shown that the transducer gain, g_t , from ω_s to $3\omega_s$ is

$$g_t(V_L) = \frac{288 (\omega_s b I_p)^2 G_s G_p G_L (2G_p I_s + \omega_s b I_p V_L)}{I_s \underbrace{\left[256 (G_s G_L G_p^2)^2 - 9 (\omega_s b I_p)^4 \right]}_1}. \quad (3.66)$$

It is clear from (3.66) that the parameters G_s , G_p , and G_L may be selected to provide any amount of gain for a given NLC.

The RF-RF conversion efficiency of phase-coherent upconverting parametric amplifiers can also be explored using (3.65) when defining conversion efficiency as the ratio of output power at ω_{3fs} to the available pump power at ω_p .

$$\eta = \frac{288 (\omega_s b G_p)^2 I_s G_L (2 G_p I_s + \omega_s b I_p V_L)}{256 (G_s G_L G_p^2)^2 - 9 (\omega_s b I_p)^4} \quad (3.67)$$

CHAPTER IV

DESIGN AND PERFORMANCE OF UPCONVERTING AND NEGATIVE-RESISTANCE PARAMETRIC AMPLIFIERS

The analytical models derived in Chapter 3 provide a set of design equations for developing parametric upconverters and negative-resistance parametric amplifiers. However, by themselves, the analytical models are not sufficient to construct an entire parametric system. The parametric amplifier must be embedded in an architecture that not only supports the necessary conditions outlined in previous chapters for achieving high gain and broad bandwidth, but must also provide isolation between the source, pump, and/or output/idler circuits, and properly transform impedances to their optimal values. When properly designed and optimized, parametric amplifiers are comparable in performance to their transconductance counterparts in power gain and operating bandwidth.

4.1 VHF and RF Phase-Incoherent Upconverting Parametric Amplifiers

Utilizing (3.17), (3.18), (3.27), and (3.28), two phase-incoherent upconverting parametric amplifiers were constructed. Both upconverting amplifiers were similarly designed following the topology of Fig. 13. The first amplifier upconverted a 30 MHz signal to 300 MHz through parametric mixing with a 270 MHz pump. Varactor diodes were used to act at the nonlinear capacitive mechanism. The varactor diode chosen was the 1S2208 (characteristically similar to the BB833) that has a junction capacitance range of approximately 5 pF at maximum reverse bias to 50 pF at zero

bias with a minimum quality factor of 130 at 50 MHz. The varactors were placed in anti-parallel such that the upconverted output currents were in anti-phase to create a virtual ground between the two varactors at the upconverted frequency. This balanced operation allowed for the pump and source circuits to be introduced at the virtual ground without shorting the upconverted output current [43]. Electrical isolation between the pump and source was accomplished using high-Q resonant traps that also assisted in transforming the varactor impedance to its optimal value at the pump and source frequencies. The balanced upconverted currents were then combined using a coaxial balun that also acted as the output match to transform a standard 50 Ohm load to 100 Ohms differential. The DC bias voltages were introduced through transmission lines a quarter-wavelength long at the upconverted output frequency and connected to the balun's balanced inputs. These transmission lines prevented leakage currents at the upconverted frequency.

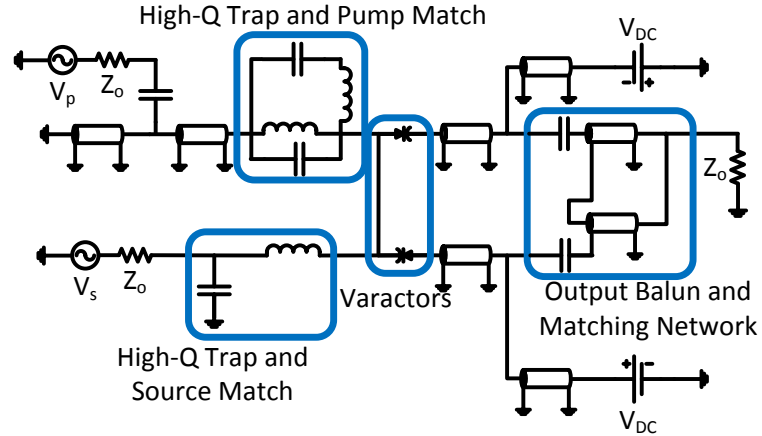


Figure 13: Circuit topology for both the VHF and RF phase-incoherent upconverting parametric amplifiers.

The VHF upconverting parametric amplifier was first simulated in a harmonic-balance simulator using standard SPICE models for all components. Simulations predicted a linear power gain of approximately 8 dB at a pump power level of 20 dBm when practical losses were included in all circuit components. Using the definition of

efficiency in (3.25), a maximum RF-RF conversion efficiency of 50.7% was achieved in saturated conditions. Simulations estimated the 3 dB bandwidth to be approximately 29.48 MHz to 31.2 MHz, or 5.73% fractional bandwidth.

The breadboard shown in Fig. 14 was fabricated to compare measured performance to simulated results.

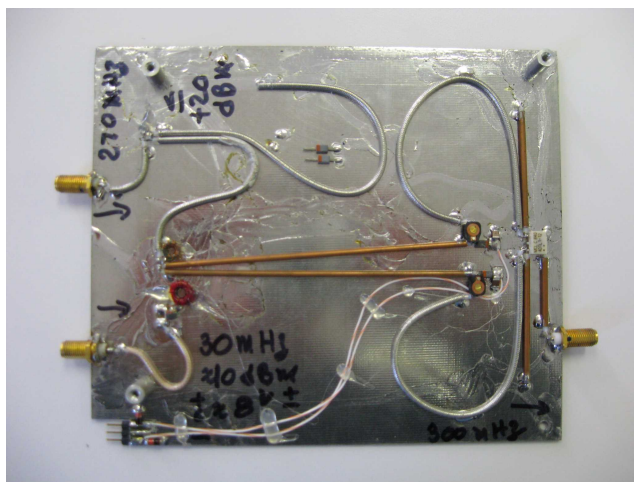


Figure 14: Hardware implementation of the VHF upconverting parametric amplifier.

By increasing the source power level, the 1-dB compression point was measured to be 16.87 dBm at $P_s = 10.86$ dBm and $P_p = 20$ dBm. This translated to an efficiency in saturated conditions of 48.6%. At that signal drive level, the varactor became forward biased and created a hard saturation where the output power remained at 16.87 dBm regardless of any increase in P_s . As a result, P_{3dB} was also measured to be approximately 16.87 dBm. The 3-dB bandwidth was next determined. Because of the tuned circuits on the source, pump, and output side, the 3-dB bandwidth is narrow and was measured to be 28.28 MHz to 31.3 MHz, or a 10.1% bandwidth. Figure 15 shows the agreement between simulated and breadboard measurements for gain compression and efficiency at the optimal pump power level and DC bias point.

The analytical model in (3.17) predicts that the parametric amplifier will maximize its gain when the change in varactor junction capacitance is at its maximum. Care

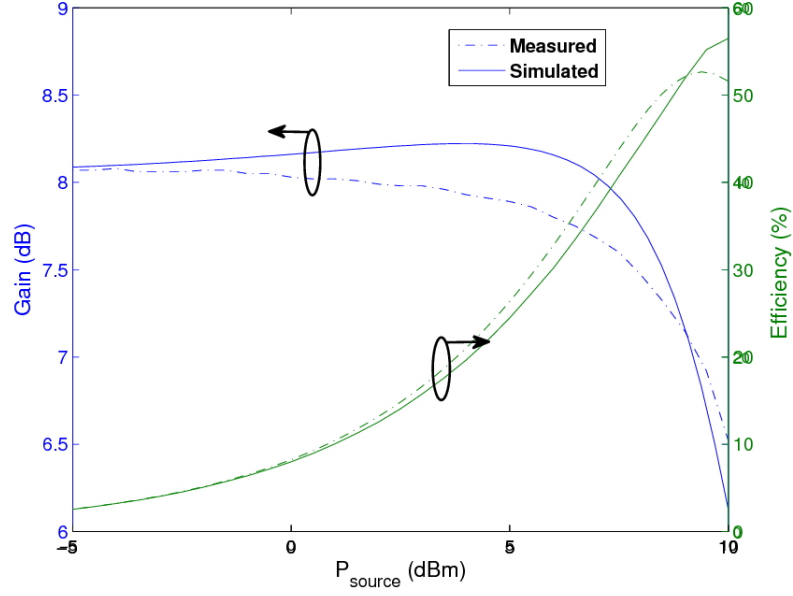


Figure 15: Simulated and measured gain and efficiency versus source power for the VHF upconverting parametric amplifier.

must be taken to limit the voltage swing across the varactor's terminals to prevent the diode from entering forward conduction. The differential design and optimal bias point establish a voltage swing across the varactor causing a capacitive change from 7.40 pF to 49.95 pF at $P_p = 20$ dBm. This results in a maximum-to-minimum capacitance ratio of 6.75. The quality factor of the varactor at the source, pump, and upconverted frequencies can be found by derating the varactor quality factor from 130 as measured at 50 MHz, however, γ in (3.21) will approximately be 1 since the quality factor is high for these frequencies. Therefore, gain degradation will be dominated by the experienced change in varactor capacitance under large-signal excitation. Application of (3.17) under optimal bias conditions and pump drive power results in

$$G_o = \frac{300 \text{ MHz}}{30 \text{ MHz}} \left(1 - \frac{7.4 \text{ pF}}{49.95 \text{ pF}} \right)^2 = 8.61 \text{ dB}. \quad (4.1)$$

The maximum measured gain at $P_p = 20$ dBm and optimal bias point, $V_{\text{bias}} = -9$

V, is 8.16 dB. Thus, the discrepancy between measured and calculated gain is 0.45 dB. The use of a piecewise-linear model for the reactive nonlinearity accounts for the small error between measured and calculated power gain.

The analytical model is not limited to predicting gain degradation under optimal operating conditions; it can also predict the change in gain as the capacitance ratio deviates from its maximum. Reducing the pump input power decreases the voltage swing across the varactor and limits the achievable capacitive ratio. At $P_p = 15$ dBm, the varactor junction capacitance changes from 11.1 pF to 49.95 pF resulting in a capacitance ratio of 4.5. Equation (3.17) then predicts a maximum power gain of

$$G_o = \frac{300 \text{ MHz}}{30 \text{ MHz}} \left(1 - \frac{11.1 \text{ pF}}{49.95 \text{ pF}} \right)^2 = 7.82 \text{ dB.} \quad (4.2)$$

Breadboard measurements under identical non-optimal conditions show a maximum obtainable power gain of 7.71 dB, which is a 0.11 dB discrepancy from the analytical model prediction.

The VHF parametric upconverter was then tested over a broad range of operating conditions and the measured data was compared to values predicted by (3.17) and (3.27). Figure 16 compares measured and predicted values for the linear gain against changing pump and source power levels for a constant bias voltage, and Fig. 17 compares measured and predicted values for the linear efficiency against changing bias levels and source power levels at a constant pump power level.

The small error between the analytical prediction and measured response can be graphically explained. Consider a small perturbation in the terminal voltage of the varactor about an operating point near the breakpoint of the piecewise-linear C-V curve, as seen in Fig. 18(a). The resulting change in capacitance is greater for the piecewise-linear curve than that of the actual since the slope of the actual curve is

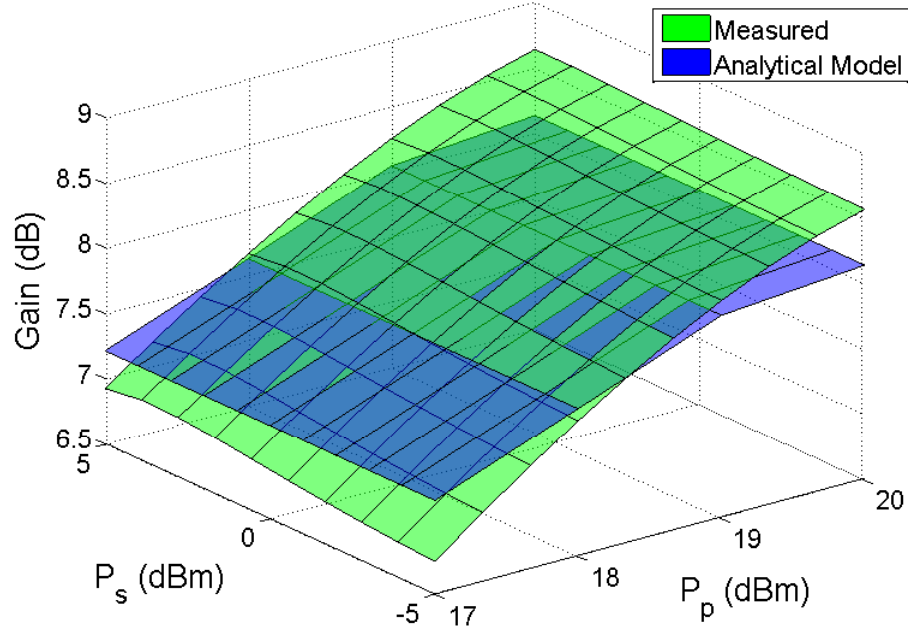


Figure 16: Comparison of surface plots of the measured gain of the VHF breadboard upconverting parametric amplifier against predicted by the analytical model of (3.17).

less than that of the approximation near the operating point. As a result, the gain analytical model overestimates the change in capacitance and returns a value greater than is measured. Conversely, in Fig. 18(b), the perturbation is applied about a bias point near zero volts where the slope of the actual C-V curve is greater than the slope of the piecewise-linear. The gain analytical model now underestimates the change in capacitance and returns a value that is less than measured. This error could be corrected by implementing a model for the C-V curve of the varactor similar to that used in [44] but the resulting equation is much more complex and is of little practical use for the purposes of circuit design.

The second upconverting parametric amplifier translated a 140 MHz input to 1.3 GHz through parametric mixing with a 1.16 GHz pump source. As with the previously discussed upconverting parametric amplifier, the 1S2208 varactor diode was chosen as the nonlinear capacitor for its high quality factor and available change

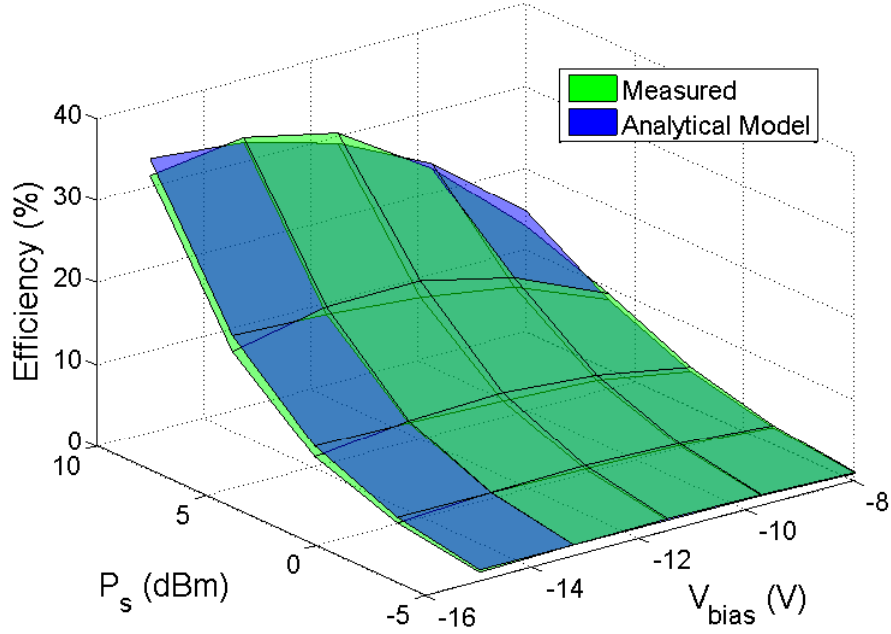


Figure 17: Comparison of surface plots of the measured system efficiency of the VHF breadboard upconverting parametric amplifier against predicted by the analytical model of (3.34).

in capacitance. The design of this RF upconverter was practically identical to the previously discussed following an architecture and layout similar to Fig. 13.

The RF upconverting parametric amplifier was first modeled in a harmonic balance simulator using standard SPICE models for all circuit components. Simulations predicted a linear power gain of 4 dB and a maximum efficiency of 30% in backoff at $P_p = 23$ dBm when practical losses were included in the transmission lines. Once constructed, the RF upconverting parametric amplifier demonstrated a maximum gain and efficiency of 4.5 dB and 37%, respectively, as P_s approached saturated operating levels.

The performance of the RF upconverting parametric amplifier and the ability of the analytical models in (3.17) and (3.27) to accurately predict the gain and efficiency across a wide range of operating points can be determined from the constructed breadboard. To compute the predicted responses from the gain and efficiency analytical

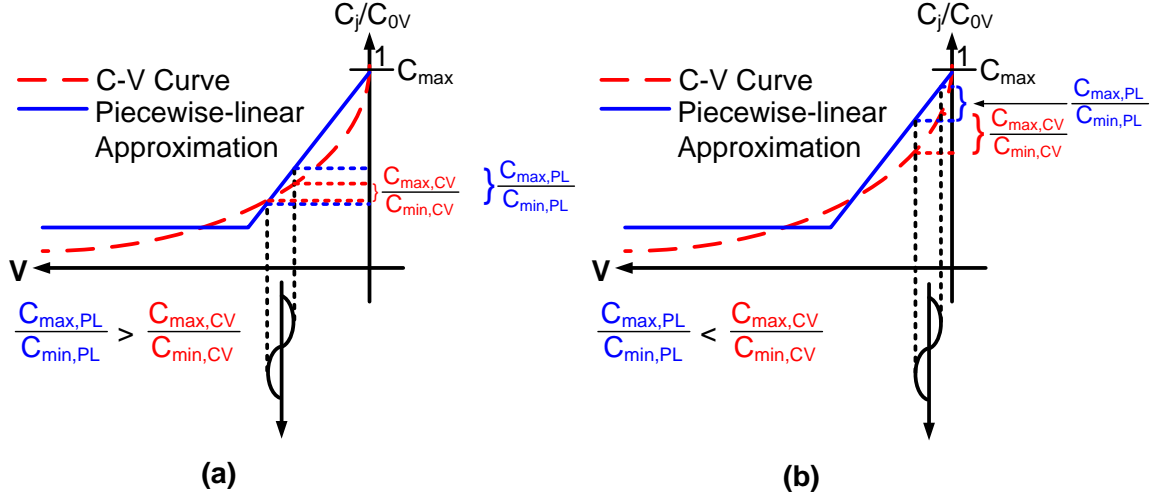


Figure 18: Mathematical reasoning behind the error between the prediction made by the gain analytical model of (3.17) and the measured results from the VHF breadboard upconverting parametric amplifier.

models, the varactor terminal voltage swing must be known at both the pump and source frequencies. Simulated measurements were used to determine both the capacitance ratio of the varactor under excitation and the peak source voltage at the varactor terminals. Because of the accuracy of the simulated results as compared to the measured results from the breadboard parametric upconverter, the simulated capacitance ratio and peak source voltage at the varactor terminals are considered to be indicative of what would be physically measured on the breadboard upconverting parametric amplifier.

Figure 19 compares the surface plot of the measured gain of the breadboard upconverting parametric amplifier to that predicted by the analytical model of (3.17), and Fig. 20 compares the measured efficiency to that predicted by the analytical model of (3.27). The small error between the measured and predicted values for both figures can be explained using the same argument presented above for the VHF upconverting parametric amplifier.

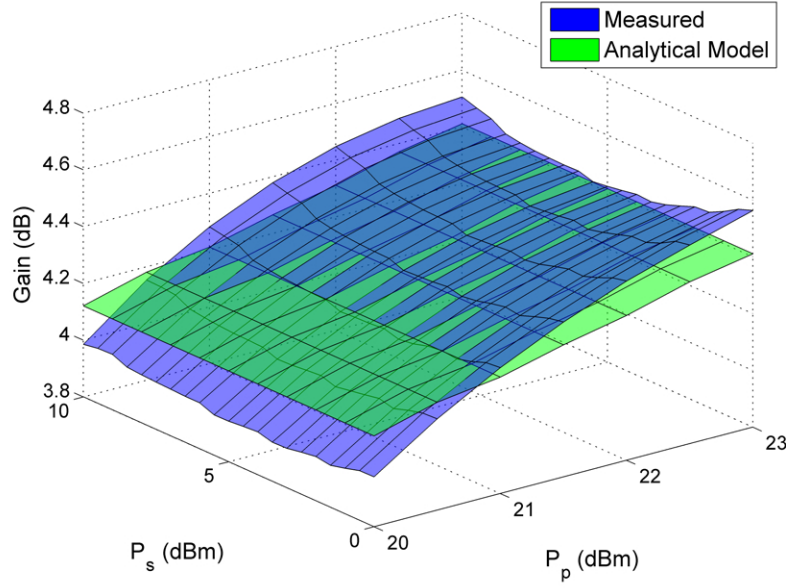


Figure 19: Surface plot comparison of the measured gain of the RF breadboard upconverting parametric amplifier to that predicted by the analytical model of (3.17).

4.2 *Phase-Coherent Negative-Resistance Degenerate Parametric Amplifiers*

Three fundamental conditions must be satisfied for a nonlinear capacitance to exhibit a negative resistance. First, a large-signal pumping source is needed to drive the nonlinear action. Second, the large-signal average capacitance of the nonlinear capacitor, C_o , must be eliminated by an attached resonant network, and, finally, the resonant network must properly isolate currents at ω_s from those at ω_p [39]. It was demonstrated in Chapter 3 that when these three requirements are satisfied, and the resonant conditions

$$L_s = \frac{1}{\omega_s^2(C_s + C_o)} \text{ and } L_p = \frac{1}{\omega_p^2(C_p + C_o)} \quad (4.3)$$

are established, (3.46) will predict the small-signal transducer gain, g_t , of a degenerate negative-resistance parametric amplifier.

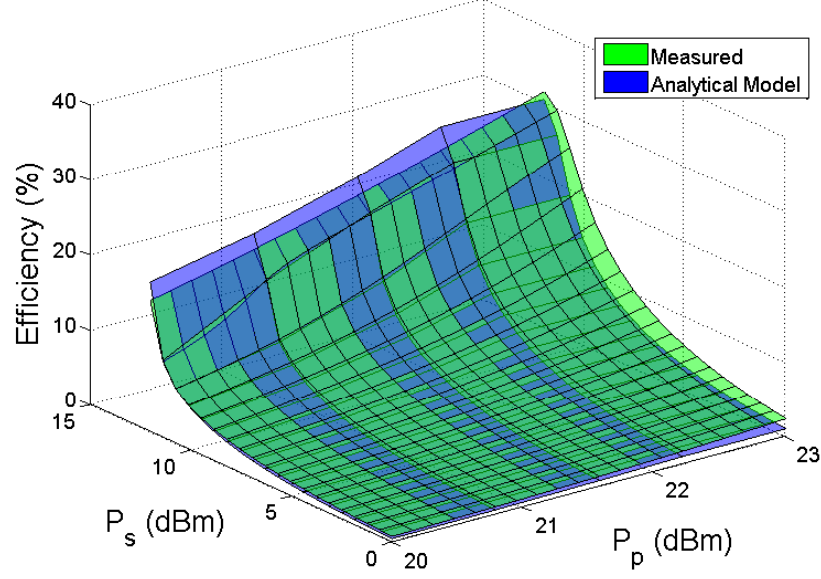


Figure 20: Comparison of surface plots of the measured system efficiency of the breadboard parametric upconverter against the predicted efficiency of the analytical model of (3.34).

To satisfy the three fundamental conditions outlined above across a broad range of operating frequencies, a double-balanced mixer (DBM) architecture was adopted. Double-balanced structures have the advantage of inherent isolation at all ports, broadband rejection of pump noise, spurious signals, and intermodulation products, and broadband operation. Conversely, the primary disadvantages of double-balanced mixer architectures are that they require four diodes and two baluns. However, the advantages of a double-balanced mixer architecture outweigh the disadvantages, making it ideal for use as a degenerate parametric amplifier architecture [45]. Figure 21 shows a double-balanced ring mixer.

The double-balanced mixer provides balanced differential signals at both the pump and source frequencies to each of the four ring diodes. Assuming ideal baluns, the incident balanced pump waveforms (blue) and source waveforms (red) will be of equal amplitude and perfectly 180 degrees out of phase. The differential action of the baluns force a virtual ground for both the incident pump waveforms (blue dashed line) and

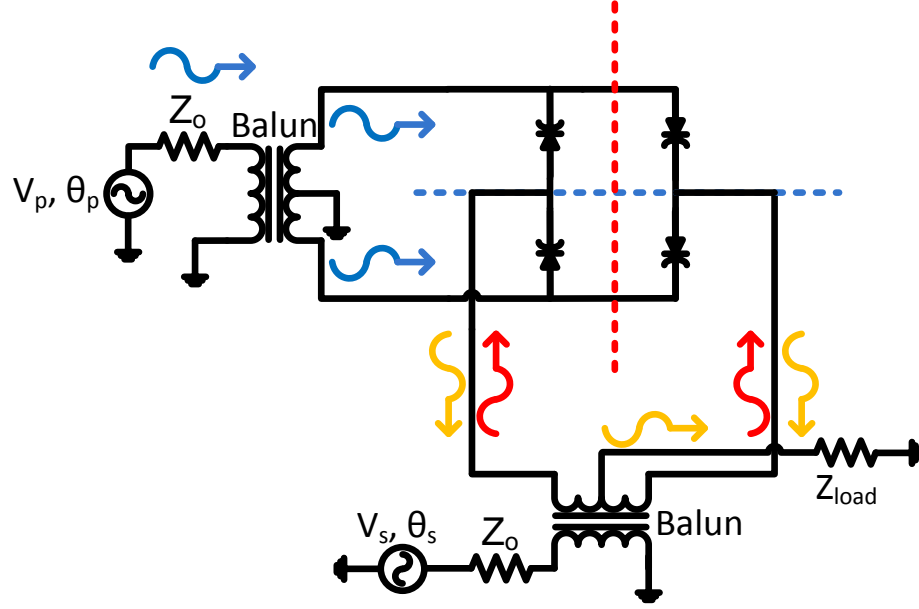


Figure 21: A double-balanced mixer showing the incident and reflected source, pump, and output waves. By Conservation of Phase, the reflected source waveforms will be in-phase and will combine at the center tap of the secondary of the source balun.

source waveforms (red dashed line) at the varactor diode terminals. Connecting the pump circuit to the source circuit's virtual ground and vice versa provides broadband isolation between the two. The incident source waveforms interact with the pumped varactors in anti-phase such that by the Conservation of Phase for mixers the reflected waveforms must be in-phase. The source reflected waves then combine to the center tap of the secondary of the source balun to form the output.

To better understand how the Conservation of Phase for mixers guarantees the source reflected waves will be in-phase with each other, consider the equivalent source circuit in Fig. 22. In each branch, the varactors are connected in anti-parallel but the polarity of the pumping voltage ensures that the change in capacitance is identical. Because of the differential pumping of the varactors, the pump voltage phase relationship between branch 1 and branch 2 will always be 180 degrees. Therefore, regardless of the dot convention of either the source or pump balun the possible phase

of each reflected source waveform is

$$\text{Branch 1: } \phi_p - \phi_s = 0^\circ \text{ or } 180^\circ - 0^\circ = 0^\circ \text{ or } 180^\circ \quad (4.4)$$

$$\text{Branch 2: } \phi_p - \phi_s = 180^\circ \text{ or } 0^\circ - 180^\circ = 0^\circ \text{ or } -180^\circ \quad (4.5)$$

such that the reflected source wave in branch 1 will always be in phase with the reflected source wave in branch 2.

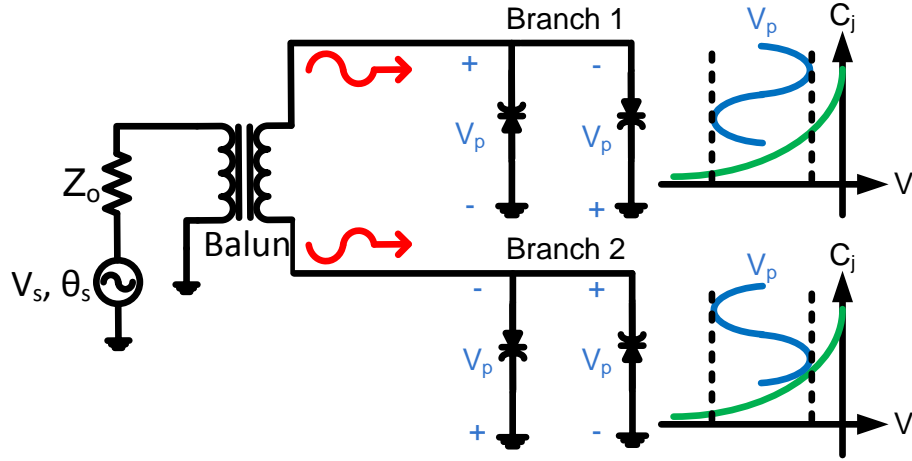


Figure 22: Equivalent circuit from the perspective of the source generator. The polarity of the pumping voltage across each varactor is indicated to illustrate how Conservation of Phase for mixers will guarantee the reflected waves will always be in-phase.

Figure 23 shows the circuit design of the phase-coherent degenerate parametric amplifier in the DBM architecture. Varactor diodes were selected to act as the non-linear capacitive mechanism. The design in Fig. 23 was implemented in a single-tone harmonic balance simulator with the source frequency set as the fundamental (note that the source and pump frequencies are commensurate in a degenerate paramp, so only one fundamental is needed), using standard SPICE models for all components. The varactor diodes are the BB857 model that have an available junction

capacitance range of approximately 0.5 pF at their maximum reverse bias voltage of 30 V to 6.6 pF at zero volt bias. Each varactor was doubled-up in parallel to center the capacitance-voltage curve for maximum gain. Surface-mount transforming baluns were chosen (Minicircuits TC4-25+), and RF crossovers were needed for routing traces in a single-layer microstrip environment. The prototype circuit was fabricated on 62 mils thick Rogers 4350 RF substrate material with 1 oz copper plating, as seen in Fig. 24.

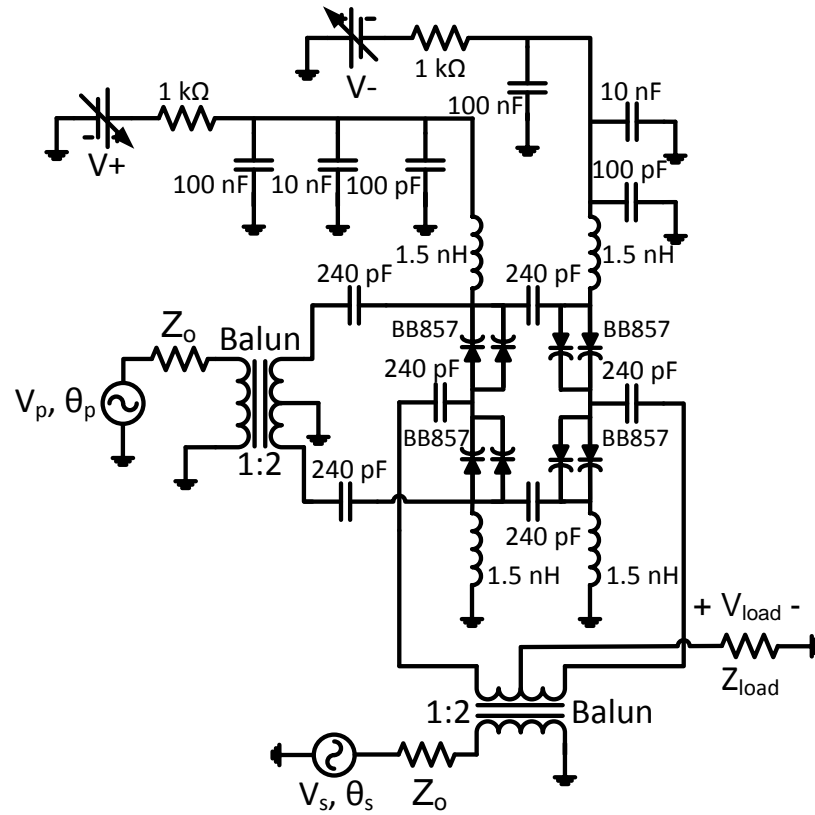


Figure 23: Circuit schematic of the double-balanced phase-coherent degenerate parametric amplifier showing all component values.

To test the prototype, a test bench setup was constructed. This setup used two phase-locked RF signal generators (one of which has the capability of phase adjustment) to produce the phase-coherent single-tone pump and source signals, as seen in Fig. 25. The output of the degenerate parametric amplifier was monitored by a

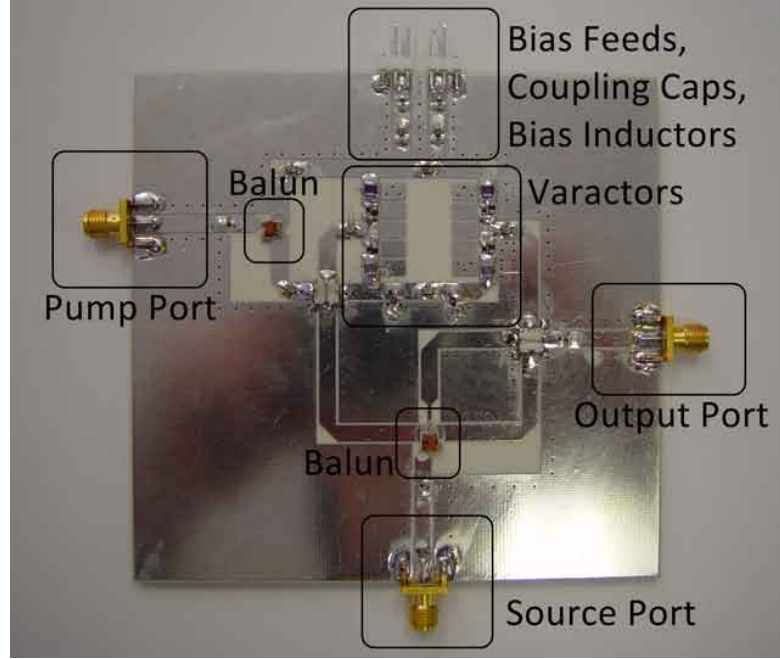


Figure 24: Photograph of the prototype double-balanced phase-coherent degenerate parametric amplifier board with critical components identified and labeled.

spectrum analyzer to confirm stable operation.

Figure 26 compares the simulated and measured gain versus source frequency of the double-balanced phase-coherent degenerate parametric amplifier at a constant pump power level of 30 dBm. This large of a pump power level was required to maximize the capacitance switch of the varactors. If lower breakdown voltage varactors had been available with similar capacitance-voltage characteristics, the necessary pump power level might have been considerably less.

Ripple can be seen in both the simulated and measured gain plots within their usable bandwidths. As the source frequency varies, phase coherence is not perfectly maintained and the amplitude of the voltage waveform at ω_p across each varactor diode fluctuates. These two factors contribute to a slight change in the negative resistance value that causes the gain ripple. In addition, the gain drops below zero when $150 \text{ MHz} > f_s > 1150 \text{ MHz}$ as it exceeds the operational bandwidth of the baluns. The average gain within the usable bandwidth of the amplifier is approximately 26

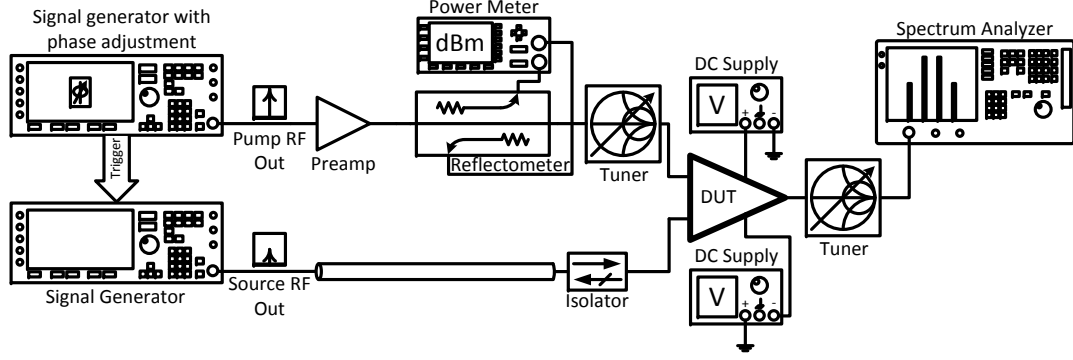


Figure 25: Test bench setup to measure gain, bandwidth, and stability of the phase-coherent degenerate parametric amplifier.

dB.

Figure 27 compares the power gain measured on the prototype double-balanced phase-coherent degenerate parametric amplifier to that predicted by the analytical model of (3.46) at $f_s = 650$ MHz across a wide range of operating conditions for both the source and pump generators. The values of G_s , G_p , G_L , and b in (3.46) were obtained in simulation. As demonstrated in Fig. 26, simulations correctly predict the measured performance of the degenerate paramp, therefore it is assumed that simulations will also correctly predict the Taylor coefficient b , as well as the transformed source, pump and load conductances seen by the varactor diodes. Figure 27 shows that the analytical model of (3.46) is capable of accurately approximating both transducer gain and gain compression deep into saturation.

Figure 28 simultaneously explores the performance of both (3.46) and (3.47) in their ability to accurately predict the AM-AM distortion characteristics. In Fig. 28, the power absorbed by the load conductance is plotted against the available source power for 3 arbitrarily chosen power gains. In backoff, the analytical model of (3.47) is able to estimate the linear gain with high certainty. Once output power saturation begins, due to the increase in magnitude of terms 2 and 4 in (3.46), compression occurs, and the prediction made by (3.46) follows closely with measured values, in

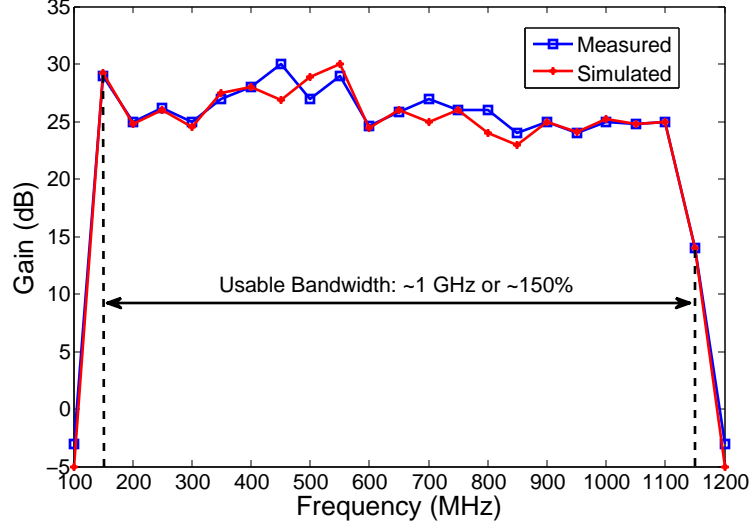


Figure 26: Plot of the simulated and measured gain versus source frequency of the double-balanced phase-coherent degenerate paramp at a constant pump power level of 30 dBm.

agreement with Fig. 27.

4.3 Phase-Coherent Upconverting Parametric Amplifiers

The analysis in Chapter 3 demonstrated that an architecture similar to that of a phase-coherent degenerate parametric amplifier could be used to demonstrate a phase-coherent upconverting amplifier. The degenerate parametric amplifier prototype developed in the above section does not use any output filtering and was intended to operate under the condition $\omega_p = 2\omega_s$ making it ideal to demonstrate phase-coherent upconversion.

Figure 29 compares the simulated and measured transducer gain versus the up-converted output frequency in addition to predicted values according to the analytical model in (3.66). Ripple in the gain can be seen within the usable bandwidth. Inspection of (3.66) shows that term 1 in the denominator is sensitive to changes in the source frequency and the transformed source, pump, and load conductances. Small perturbations in these values causes large changes in the transducer gain resulting in

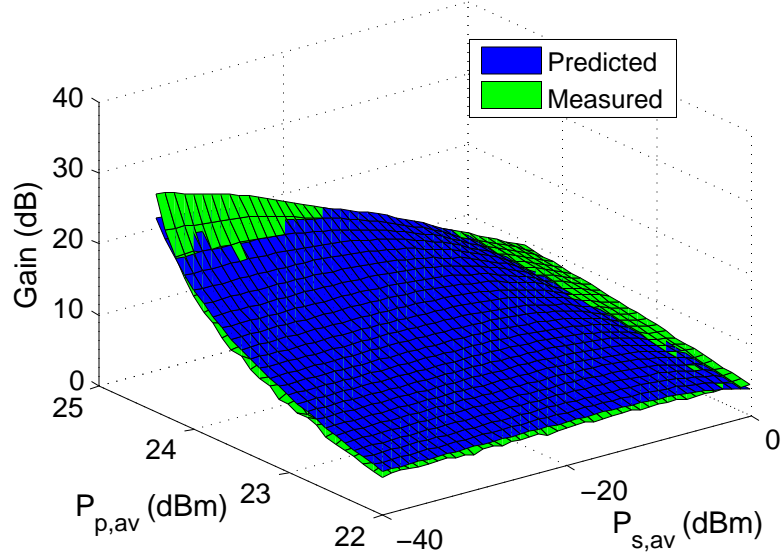


Figure 27: Plot of the measured and predicted gain versus both the available source and pump power of the double-balanced phase-coherent degenerate parametric amplifier at $f_s = 650$ MHz.

gain variations across the usable bandwidth. In addition, the gain drops below a usable value when $1.5 \text{ GHz} > 3f_s > 2.1 \text{ GHz}$. This is a result of bandwidth limitations of the source and pump baluns that introduce losses that cannot be overcome by the negative resistance.

Figure 29 also shows the theoretical phase-incoherent upconverting parametric power power gain limit imposed by the Manley-Rowe relations. As predicted by Anderson and Longo et al. in [31] and [32], the Manley-Rowe relations are incapable of predicting upconverted gain when the source and pump frequencies are phase-coherent. In addition, the achievable gain goes beyond what the Manley-Rowe relations would state is the theoretical limit for parametric upconversion.

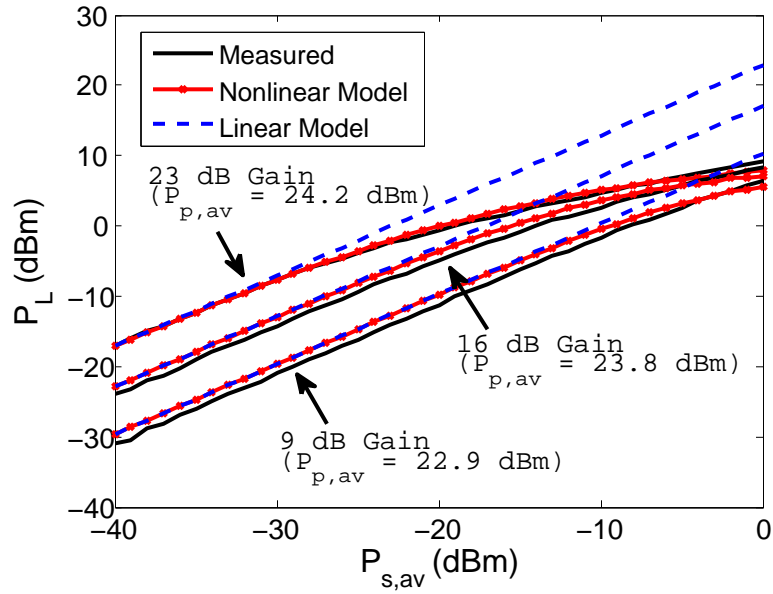


Figure 28: Plot of the measured and predicted AM-AM distortion characteristics of the double-balanced phase-coherent degenerate parametric amplifier for several values of power gain at $f_s = 650$ MHz.

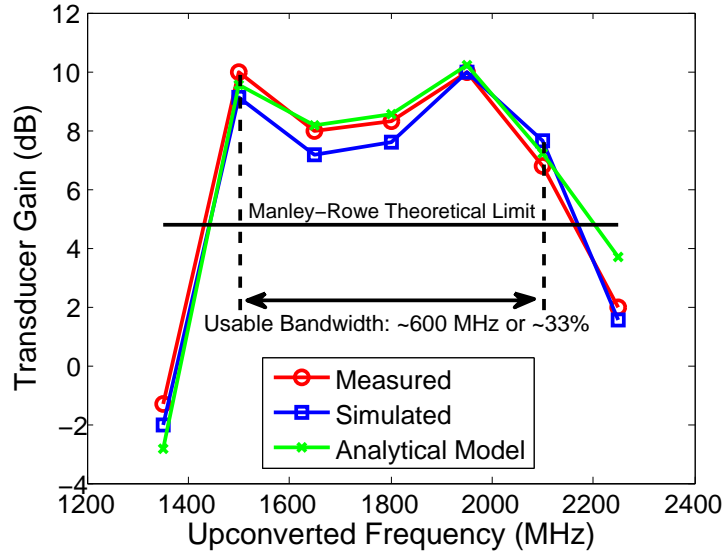


Figure 29: Simulated and measured transducer gain versus upconverted output frequency in addition to predicted values according to the analytical model in (3.66).

CHAPTER V

STABILITY ANALYSIS OF PARAMETRIC AMPLIFIERS

The strong nonlinearity of the nonlinear reactance in parametric amplifiers gives rise to situations when they can sustain an oscillation at a frequency different from those delivered by the source and pump generators or their harmonic combinations. As a result, paramps can be classified as autonomous microwave circuits. Stability analysis of autonomous microwave circuits is difficult due to their inherent nonlinearity and the usual coexistence of the oscillatory solution with a mathematical solution for which the circuit does not oscillate [39]. Traditionally, two-port amplifier stability is determined by investigating the small-signal regime of the circuit and determining if for some frequency interval $(\omega_{min}, \omega_{max})$ the S-parameters of the amplifier satisfy the Rollet stability criteria [46]. While parametric amplifiers are inherently three-port networks, they can be reduced to a two-port by linearizing the circuit equations about either the large-signal pump periodic regime (for large-signal stability analysis) or the small-signal source regime (for small-signal stability analysis). Typically, though, the Rollet stability criteria is not applicable to parametric amplifiers as it assumes the circuit is intrinsically stable and is a single-frequency device. However, the combination of the Manley-Rowe relations and the analytical models developed in Chapter 3 provides a simplified set of tools to analyze the stability of parametric amplifiers under various perturbations, operating conditions, and input and output reflection coefficients, Γ_{in} and Γ_{out} , respectively.

5.1 *Conditional Stability of Phase-Incoherent Upconverting Parametric Amplifiers*

While the Rollet stability criteria is limited to single-frequency two-port amplifiers (and thus not applicable to parametric upconverters), the general concepts of the theory can still provide a means to begin a stability analysis of phase-incoherent upconverting parametric amplifiers. By the Rollet stability criteria, a two-port amplifier is said to be unconditionally stable in the small-signal regime if $\Re\{Z_{in}(\omega)\} > 0$ for any passive complex load Z_L and $\Re\{Z_{out}(\omega)\} > 0$ for any passive complex source Z_s within the entire frequency interval $(\omega_{min}, \omega_{max})$. From the perspective of the source generator, any standing wave would be at ω_s , and from the perspective of the output, any standing wave would be at $\omega_o = \omega_s + \omega_p$. Therefore, the condition of the real part of the input and output impedances remaining positive should be satisfactory to determine upconverting parametric amplifier stability in the small-signal regime with the caveat that Z_{in} and Z_{out} be analyzed independently. Figure 30 shows a phase-incoherent upconverting parametric amplifier whose nonlinear reactance, circuit isolation filters, and pumping circuit have been placed inside a “black box.” The amplifier is being driven by an AC generator at frequency ω_s with a Thévenin impedance Z_s . The output circuit of the parametric amplifier has been terminated in an impedance Z_L resulting in a reflection coefficient Γ_L .

Unconditional stability in the small-signal regime is guaranteed if the magnitude of the total reflection coefficients seen at the source and output ports are less than or equal to 1 within the frequency interval $(\omega_{min}, \omega_{max})$ since this implies the real parts of the complex impedances $Z_{in}(\omega_s)$ and $Z_{out}(\omega_o)$ are non-negative. S-parameter analysis of the circuit in Fig. 30 can only be achieved if the circuit is treated as a one-port from, first, the perspective of the source, and, second, from the perspective of the output. Let

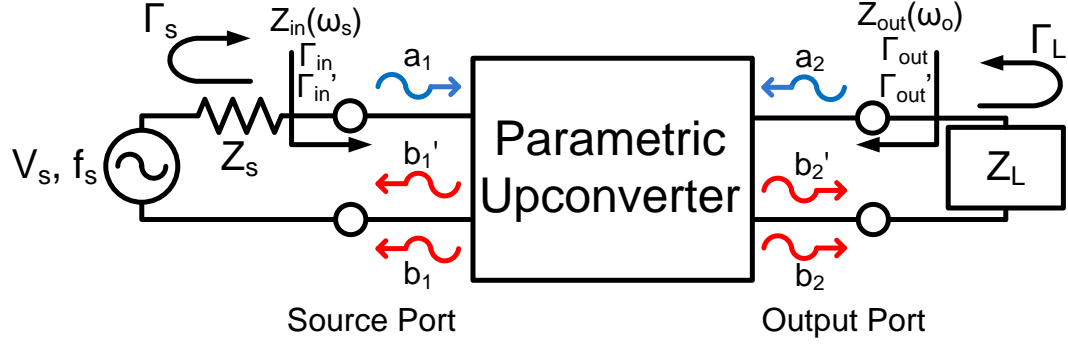


Figure 30: A black box phase-incoherent upconverting parametric amplifier. The incident and reflected source and output waves can be expressed independently of one another, allowing for the two ports to be analyzed individually.

$$\Gamma_{in} = \frac{b_1}{a_1} \quad (5.1)$$

be the input reflection coefficient without considering a substantial reverse-transfer wave b_1' . In other words, Γ_{in} is only a measure of impedance mismatch between the source generator and the phase-incoherent upconverting parametric amplifier's source port. Then, let

$$\Gamma'_{in} = \frac{b_1 + b_1'}{a_1} \quad (5.2)$$

be the total input reflection coefficient when considering the superposition of b_1 and b_1' . By S-parameter network theory,

$$a_2 = \Gamma_L b_2 \quad (5.3)$$

$$b_2 = (1 - \Gamma_{in}) S_{21} a_1 \quad (5.4)$$

$$b_1' = S_{12} a_2. \quad (5.5)$$

Substitution of (5.3), (5.4), and (5.5) into (5.2) yields

$$\Gamma'_{in} = \Gamma_{in} + S_{12}S_{21}\Gamma_L(1 - \Gamma_{in}). \quad (5.6)$$

From the Manley-Rowe relations, the idealized power gain of a phase-incoherent up-converting parametric amplifier can be expressed as $\frac{\omega_o}{\omega_s}$. In Chapter 2 it was noted that a parametric downconverter will always attenuate with an idealized minimum loss of $\frac{\omega_o}{\omega_s}$, where, for the downconverter, the down-converted output frequency ω_o is always less than the source input frequency ω_s . In addition, by the Conservation of Phase for mixers, the output of a parametric upconverter must have a relative phase equal to the sum of the relative phase of the source and the relative phase of the pump, ϕ_s and ϕ_p , respectively, and, similarly, the relative phase of the output from a parametric downconverter must be the difference between the source and pump relative phases. Finally, the forward and reverse power gain is related to S-parameter network theory by the square of S_{21} and S_{12} . Therefore, for a phase-incoherent up-converting parametric amplifier the forward- and reverse-transfer coefficients can be expressed as

$$S_{21} = \sqrt{\frac{\omega_o}{\omega_s}} \angle \phi_p \quad (5.7)$$

$$S_{12} = \sqrt{\frac{\omega_s}{\omega_o}} \angle -\phi_p. \quad (5.8)$$

It is important to note that the Manley-Rowe relations are independent of the shape of the nonlinearity curve of the nonlinear reactance, the manner in which harmonic currents are isolated, and how each harmonic current is terminated. As a result, the definition of S_{21} and S_{12} in (5.7) and (5.8) do not change for any passive reflection coefficient Γ_s or Γ_L . Equation (5.6) can now be simplified to

$$\Gamma'_{in} = \Gamma_{in} + \left(\sqrt{\frac{\omega_s}{\omega_o}} \angle \phi_p \right) \left(\sqrt{\frac{\omega_o}{\omega_s}} \angle -\phi_p \right) \Gamma_L (1 - \Gamma_{in}) = \Gamma_{in} + \Gamma_L (1 - \Gamma_{in}) \leq 1, \quad (5.9)$$

which is guaranteed to be less than or equal to 1 for any source frequency ω_s at any source power drive level that does not approach that of the pump and passive reflection coefficients Γ_s and Γ_L . Performing a similar derivation for the output port, it can be shown that

$$\Gamma'_{out} = \Gamma_{out} + S_{21} S_{12} \Gamma_s (1 - \Gamma_{out}) \leq 1, \quad (5.10)$$

where

$$\Gamma'_{out} = \frac{b_2 + b'_2}{a_2} \quad (5.11)$$

$$\Gamma_{out} = \frac{b_2}{a_2}, \quad (5.12)$$

and S_{21} and S_{12} are defined by (5.7) and (5.8). Equation (5.10) is guaranteed to be less than or equal to 1 for any output frequency ω_o at any source power drive level that does not approach that of the pump and passive reflection coefficients Γ_s and Γ_L .

From the analysis presented above, it would appear that phase-incoherent upconverting parametric amplifiers are unconditionally stable for any and all frequencies and input drive levels. However, this analysis focused on the small-signal response of the amplifier in the small-signal regime by linearizing its response to the large-signal pumping source. To complete the stability analysis of upconverting parametric amplifiers, the circuit must be linearized about the large-signal pumping source to determine its response in the periodic large-signal regime.

An analysis performed by Suárez in [47] demonstrated the capability of oscillation for a nonlinear capacitance being pumped by a periodic large-signal source. It was assumed that the circuit was lossy and contained some inductive reactance. At some pumping power threshold the circuit will exhibit a flip bifurcation resulting in a steady-state subharmonic oscillation at the natural frequency $\omega_o = \frac{\omega_p}{2}$. The former periodic solution occurring at ω_p continues to exist after the flip bifurcation, but it has become unstable. Beyond the threshold point the only observable solution is the frequency-divided solution.

Combining the small-signal and large-signal analysis for phase-incoherent upconverting parametric amplifiers it can be seen that they are conditionally stable. It should be noted that the possibility of a flip bifurcation was not explored in the small-signal analysis as it was assumed that the amplifier was intrinsically stable when linearized about the small-signal solution and that the input source drive level would never approach that of the pumping source. To do so would lead the analysis out of the small-signal regime and into the large-signal regime.

5.2 Conditional Stability of Negative-Resistance Parametric Amplifiers

The analytical models developed in Chapter 3 regarding both degenerate and non-degenerate parametric amplifiers shows the generation of a negative resistance. Power gain is possible when the negative resistance is large enough as the circuit attempts to balance the excess negative resistance exhibited by the nonlinear reactance with the positive resistance presented by the losses of the surrounding linear circuitry. However, when the value of the negative resistance exceeds the positive losses of the circuit, balance cannot be maintained, and the circuit will become unstable. From (3.46), large-signal stability will be maintained for degenerate parametric amplifiers when

$$G_s + \frac{(\omega_s b)^2}{2G_L G_p} P_L > \frac{\omega_s b I_p}{2G_p}. \quad (5.13)$$

To better understand the conditions for large-signal stability, assume that the source conductance G_s is small compared to $\frac{(\omega_s b)^2}{2G_L G_p} P_L$. Then, (5.13) reduces to

$$I_p < \frac{\omega_s b P_L}{G_L}. \quad (5.14)$$

Let $P_L = V_s^2 G_L$ such that

$$I_p < \omega_s b V_s^2 = \omega_s C_{s,NL} V_s, \quad (5.15)$$

where $C_{s,NL}$ is a measure of the nonlinearity of the capacitance-voltage curve of the nonlinear reactance. It is now useful to define a new positive resistance, $R_{stab} = \frac{V_s}{I_p}$, that relates the peak value of the voltage waveform across the nonlinear reactance at the source frequency to the peak value of the pump current generator such that

$$R_{stab} > \frac{1}{\omega_s C_{s,NL}}. \quad (5.16)$$

Evaluating the inequality of (5.16) shows that as the pump drive level is increased, R_{stab} decreases, and eventually will fall below the stability threshold resulting in unstable operation. In addition, an unexpected result comes from this inequality. Decreasing $C_{s,NL}$, and all else being unchanged, can eventually lead to instability. $C_{s,NL}$ is a measure of nonlinearity of the nonlinear reactance at the DC operating point. To decrease the nonlinearity when using, say, a varactor diode as a voltage-dependent nonlinear capacitor, one would increase the DC bias voltage such that the

operating point sat in the linear portion of the capacitance-voltage curve. At first this would seem counterintuitive based on the large-signal transducer gain analytical model in (3.46). However, (5.16) seems to suggest that a decrease in the nonlinearity of the nonlinear reactance at the DC operating point has an overall effect of increasing the negative resistance seen by the source resulting in an increase in the power gain. Following a similar derivation for non-degenerate parametric amplifiers, and using the transducer gain analytical model in (2.48), the criteria for stable operation can be shown to be

$$R_{stab} > \frac{1}{\sqrt{\omega_i \omega_s} C_{s,NL}}. \quad (5.17)$$

In Chapter 4, a phase-coherent degenerate parametric amplifier was designed based on the analytical models developed in Chapter 3. Because of the direct relationship between gain and stability in the large-signal regime, and the sensitivity of stability to small perturbations, an in-depth stability analysis of phase-coherent negative-resistance parametric amplifiers is warranted.

As discussed in Chapter 3, to obtain the maximum gain in phase-coherent degenerate parametric amplifiers, the phase condition $\phi_p = 2\phi_s$ must be imposed. The pump power must also be properly selected, which is generally done through a power sweep, most often using a commercially-available harmonic balance (HB) simulator. Inspection of (5.16) shows that perturbations in the pump power level results in changes in R_{stab} that could potentially destabilize the amplifier. Therefore, to continue the stability analysis of phase-coherent degenerate parametric amplifiers the evolution of the system poles will be determined under variations in the pump power level.

The poles are obtained by, first, inserting a small-signal current source of value I_s at a perturbation frequency, Ω , in parallel with a sensitive circuit node such as the cathode of a varactor diode [39, 48]. Next, the conversion-matrix approach is applied to linearize the circuit about each particular steady-state solution. A closed-loop

transfer function, $Z(\Omega)$, can then be defined as the ratio between the node voltage and the perturbation current I_s . Finally, the fitting of $Z(\Omega)$ with a quotient of polynomials numerically provides the poles associated with each steady-state solution. Figure 31 shows the evolution of the system poles of the phase-coherent degenerate parametric amplifier developed in Chapter 4 at $f_s = 400, 650$, and 900 MHz as the pump power level is swept from 28 dBm to 35 dBm. It can be seen that a set of complex poles at 650 MHz cross the imaginary axis into the right-half plane approximately when $P_p = 30.85$ dBm, resulting in a flip bifurcation. However, the amplifier appears to be stable within its usable bandwidth below $P_p = 30.5$ dBm.

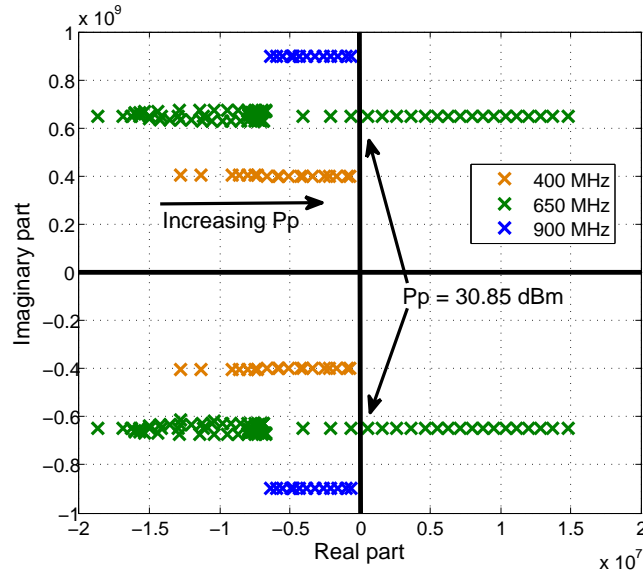


Figure 31: Evolution of the system poles of the phase-coherent degenerate parametric amplifier as the pump power level is swept. A set of complex poles at 650 MHz cross the imaginary axis at about $P_p = 30.85$ dBm causing a flip bifurcation and destabilizing the amplifier. The paramp appears to be stable when $P_p < 30.5$ dBm.

With phase-coherent degenerate parametric amplifiers, a flip bifurcation results in the coexistence of an oscillatory solution at the same frequency as the source input. The evolution of the system poles in Fig. 31 provides no insight into the implications of this instability on the solution curves in the periodic regime as this is dependent on the initial conditions of the amplifier and the relative phase of the oscillatory solution

with respect to the source input.

The stability properties of periodic regimes are determined by the Floquet multipliers [39, 49] with the number of multipliers agreeing with the system dimension N . In the frequency domain, stability is analyzed in terms of the poles, or roots, of the characteristic determinant of the harmonic balance (HB) system perturbed about the periodic regime. This determinant can be written in a compact manner as $\det[JH(k\omega_s + p)] = 0$, where J is the Jacobian matrix and $k = -NH$ to NH , where NH is the number of harmonic terms. There is a non-univocal relationship between the poles and the multipliers, given by $m_i = e^{p_k^i T_s}$, with $i = 1$ to N and T_s the solution period. Thus, there is a set of poles $p_i^k = p_i^0 + jk2\pi i$, with k an integer and p_i^0 a “canonical” pole associated with multiplier m_i . The critical poles, $p = \pm j\omega_s = \pm j\frac{\omega_p}{2}$, are associated with the multiplier $m_1 = e^{\pm j\frac{\omega_p}{2}T_s} = 1$. Also associated with m_1 is a pole with value zero, $p = 0$. For $p = 0$, the characteristic determinant agrees with the determinant of the Jacobian matrix of the original HB system. Therefore, the HB system should become singular at the bifurcation point with the critical poles $p = \pm j\frac{\omega_p}{2}$. This singularity can give rise to a turning point of the solution curve or to the onset of new solution paths at the same fundamental frequency ω_s [39, 49, 50].

To illustrate this, it will be assumed that prior to the bifurcation (occurring at η_o) there is only one solution per parameter value (single curve). Let \bar{X}_o be the HB solution at the bifurcation $\bar{H}(\bar{X}, \eta_o) = 0$. For an arbitrarily small increment $\Delta\eta$, the HB system can be linearized about \bar{X}_o . Then it is straightforward to demonstrate that the generation of new solution branches from \bar{X}_o is only possible in the case of a singular Jacobian matrix $\frac{\partial \bar{H}}{\partial \bar{X}_o}$. This situation can be associated with a pitchfork bifurcation [50] ruled by the transformation

$$S_o \rightarrow 2S'_o + S_1, \quad (5.18)$$

where the sub-index indicates the number of unstable poles. At the bifurcation, the original solution curve S_o becomes unstable (S_1) and gives rise to two distinct stable solutions S'_o . In fact, this pitchfork bifurcation is difficult to observe in practice because it requires particular symmetry conditions. Instead, the system exhibits an imperfect pitchfork bifurcation [39].

Utilizing the simulations and prototype board developed in Chapter 4, solution curves were obtained across multiple frequency and operating points. At $f_s = 716$ MHz, the output-power curve obtained with a HB simulation passes through a maximum, then begins to decrease, as seen in Fig. 32. The evolution of the system poles in Fig. 31 shows that at the sharp maximum near 650 MHz a pair of complex conjugate poles, $\sigma \pm j\frac{\omega_p}{2}$, cross the imaginary axis into the right half of the complex plane. However, there is no clue on how the system evolves after this bifurcation point. In fact, the remainder of the curve obtained in HB is unstable and unobservable.

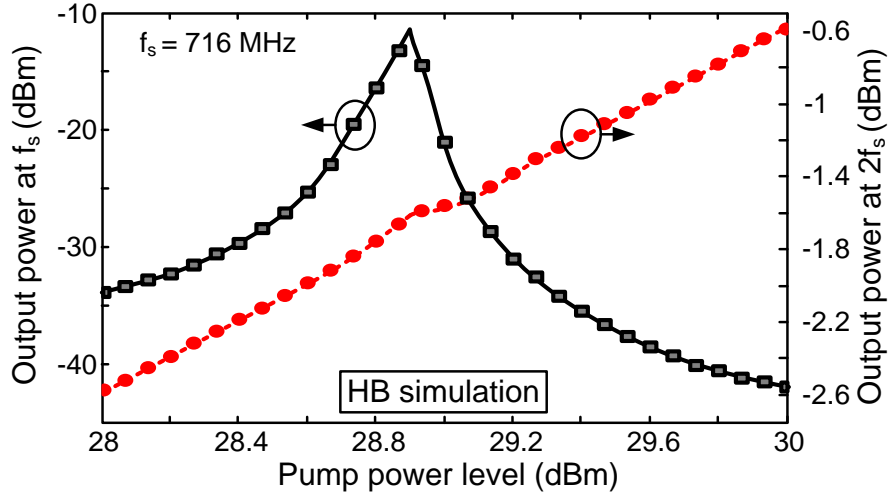


Figure 32: Solution curve of the phase-coherent degenerate parametric amplifier at $f_s = 716$ MHz using a HB simulation.

To search for other possible solution paths, auxiliary generators (AGs) [39] were

connected in parallel between the terminals of one of the varactor diodes. The AG operates at the source frequency, $\omega_{AG} = \omega_s$, and allows implementation of a parameter-switching technique. To obtain high slope sections of the solution curves, the AG amplitude, V_{AG} , is swept, optimizing both the AG phase, ϕ_{AG} , and the pump power in order to fulfill the non-perturbation condition $Y_{AG} = \frac{I_{AG}}{V_{AG}} = 0$, where I_{AG} is the current passing through the AG, V_{AG} is the voltage across the terminals of the AG, and Y_{AG} is the admittance seen by the AG. Using this technique, it was possible to complete the solution curves seen in Figs. 33(a) and (b).

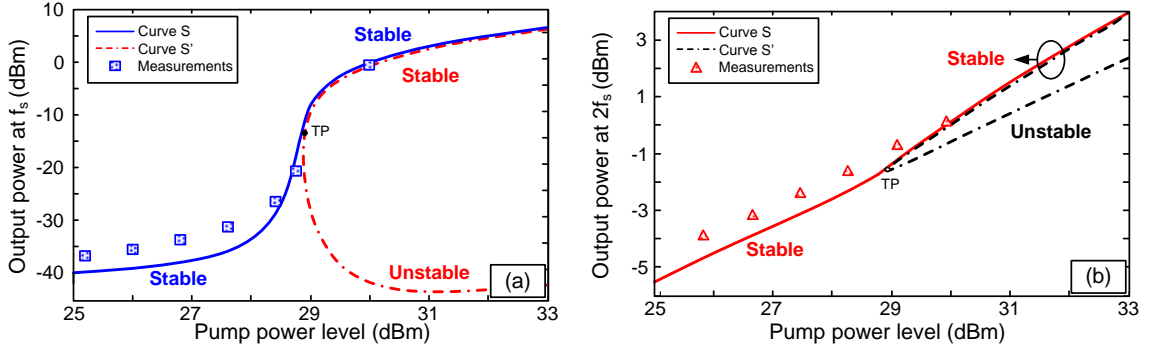


Figure 33: Analysis of the branching phenomenon of the phase-coherent degenerate parametric amplifier at $f_s = 716$ MHz.

The original curve, S , in Fig. 33(a) is continuous and quickly grows to high output power values at ω_s . There is a second path that only exists on the right hand side of Fig. 33(a), from the turning point TP ($P_p=28.9$ dBm). The upper section of this second path (S') is very close to the high power section of the original curve (S). Note that the HB simulation evolves from curve S to curve S' instead of following the fast power increase of the original curve S . In the higher output power section, the two curves S and S' have very similar amplitude values, however, they have a phase shift close to 180° at ω_s . To confirm that the difference is not due to an analysis inaccuracy, the solutions obtained with the AG have been introduced as initial conditions in the HB simulation and produced identical results.

Unlike the transformation in (5.18), there is no branching point in the curves in Fig. 33. In spite of this, the geometry of the paths suggest the possible occurrence of an imperfect pitchfork bifurcation. In this bifurcation, the original solution path (assumed stable here) S_o exists for the whole parameter interval and maintains its stability properties. However, a new independent path, with a turning point, is generated close to the original one. When the parameter is varied from the original regime S_o towards the bifurcation, the transformation at the bifurcation point is

$$S_o, \phi \rightarrow S'_o + S'_1, \quad (5.19)$$

where the second relationship indicates that there are no solutions (ϕ) in path S' before the bifurcation, and two solutions, one stable and the other unstable, after this bifurcation. Note that there is one solution prior to the bifurcation and three solutions after this bifurcation for both the perfect and imperfect pitchfork bifurcations.

To verify the above assumptions, pole-zero identification has been applied along the two solution paths in Fig. 33 with the results in Fig. 34. Curve S is stable for all values of P_p . Its dominant poles, $\sigma \pm j\frac{\omega_p}{2}$, approach the imaginary axis near the high slope section but do not cross this axis. In the case of the path S' , a pair of complex-conjugate poles $\sigma \pm j\frac{\omega_p}{2}$ cross the imaginary axis at $P_p = 28.9$ dBm; the upper section is stable and the lower section is unstable. The stability analysis confirms the existence of a transformation of the form in (5.19). This stability study explains the differences between simulations and measurements encountered in the pole-zero analysis in Fig. 31.

According to the above analysis there are two stable solutions with very similar output power values coexisting for pump power values larger than 28.9 dBm. The existence of two stable solutions can be related to the fact that the instability gives rise to a frequency division-by-2 of the pump signal. In standard divide-by-2 frequency

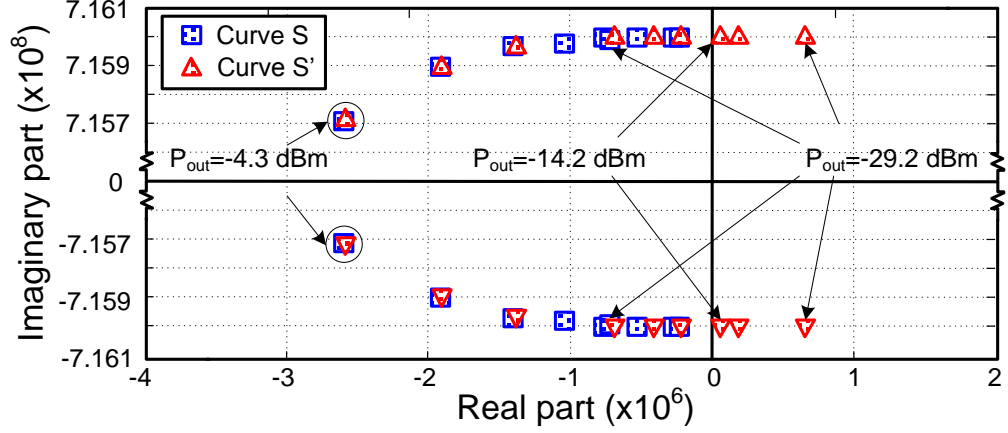


Figure 34: Stability analysis using pole-zero identification of the solution curves in Fig. 33.

dividers (without an independent source at the divided-by-2 frequency), two identical solutions with 180° phase shifts coexist after the bifurcation. In fact, the two solutions in the upper section of Fig. 33(a) have a phase difference close, but not identical to, 180° . The small difference in magnitude is attributed to the presence of an independent source at $\omega_s = \frac{\omega_p}{2}$. The power difference increases with increasing source power level, as seen in the simulation of Fig. 35. In fact, the physical observation of one solution or another will depend on the initial conditions of the amplifier.

For $f_s = 650$ MHz, there is a qualitative change in the circuit behavior, as seen in Fig. 36. Curve S exhibits the turning point (TP2) whereas curve S' does not change its stability properties in the neighborhood of this point. Curve S (providing the only circuit solution for small pump power levels) becomes unstable at TP2, so the system necessarily jumps to the upper curve section in agreement with the measurement results.

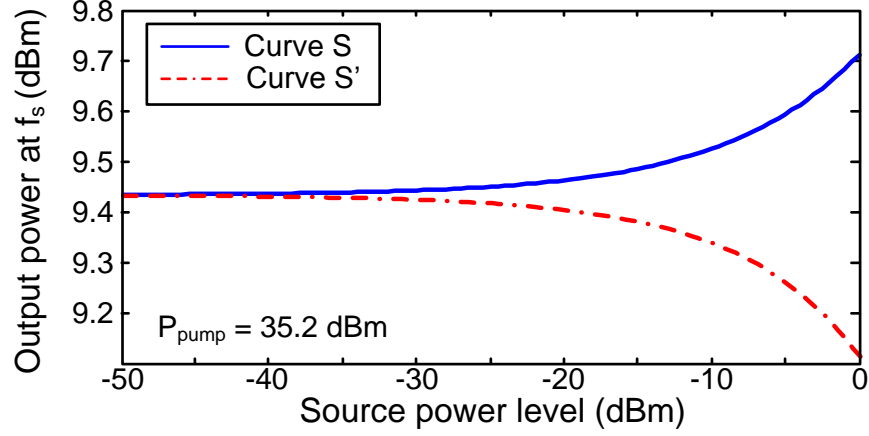


Figure 35: Variation in the output power at f_s versus increasing source power level showing two possible solution curves that are dependent on the initial conditions of the phase-coherent degenerate parametric amplifier.

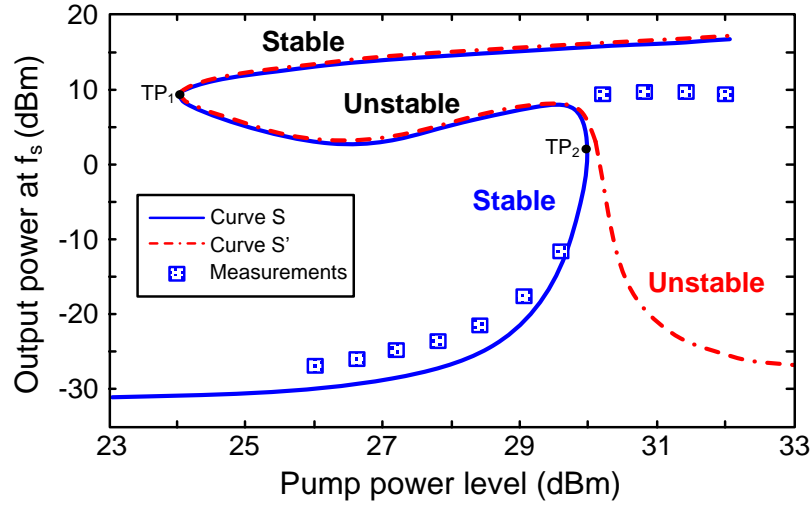


Figure 36: Solution curve for the phase-coherent negative-resistance degenerate parametric amplifier at $f_s = 650$ MHz.

5.3 Conditional Stability of Phase-Coherent Upconverting Parametric Amplifiers

The analytical models developed in Chapter 3 regarding phase-coherent upconverting parametric amplifiers shows the generation of a negative resistance at the third harmonic of the source. Power gain at the upconverted frequency is possible when

the negative resistance is large enough as the circuit attempts to balance the excess negative resistance exhibited by the nonlinear reactance with the positive resistance presented by the losses of the surrounding linear circuitry. However, when the value of the negative resistance exceeds the positive losses of the circuit, balance cannot be maintained, and the circuit will become unstable, as was seen above with phase-coherent degenerate parametric amplifiers. From (3.66), phase-coherent upconverting parametric amplifiers will maintain stability when

$$256 (G_s G_L G_p^2)^2 > 9 (\omega_s b I_p)^4. \quad (5.20)$$

Algebraic manipulation of (5.20) shows that, in terms of the pump current drive level, the amplifier will remain stable in the large-signal regime when

$$I_p < \frac{2.31 G_p \sqrt{G_s G_L}}{\omega_s b}. \quad (5.21)$$

CHAPTER VI

CONCLUSIONS AND FUTURE WORK

This chapter provides a summary of the novel contributions of this thesis, as well as comparisons of these contributions to current state-of-the-art. In addition, future work pertaining to the development and performance enhancement of parametric architectures is discussed.

6.1 Summary and Comparisons to Current State-Of-The-Art

The focus of this author's work has been on the development, characterization, and demonstration of novel parametric architectures capable of wideband operation while maintaining high gain and stability. To begin the study, phase-incoherent upconverting parametric amplifiers were explored. Simulations and breadboard prototypes were developed for two phase-incoherent upconverting parametric amplifiers; one designed to operate at VHF source input frequencies, while the other at RF. Analytical models were derived that are capable of accurately predicting the linear transducer gain and RF-RF conversion efficiency of phase-incoherent upconverting parametric amplifiers, and the prototype boards were used to validate the models. Further analysis of the analytical models and the Manley-Rowe relations led to the conclusions of bandwidth and gain limitations in phase-incoherent upconverting parametric amplifiers and resulted in their abandonment in lieu of negative-resistance parametric amplifiers.

Traditionally, there were two versions of negative-resistance parametric amplifiers available: degenerate and non-degenerate. Both modes of operation are considered single-frequency amplifiers, because both the input and output frequencies occur at

the source frequency. Degenerate parametric amplifiers offer more power gain than their non-degenerate counterpart, and do not require additional circuitry for idler currents. As a result, both a phase-coherent degenerate parametric amplifier printed circuit board prototype and simulations were developed that are capable of, on average, 26 dB of power gain across approximately an octave, or 150%, of usable fractional bandwidth centered at 650 MHz. Large-signal transducer gain and RF-RF conversion efficiency analytical models were developed that demonstrated the mechanism of gain compression responsible for AM-AM distortion in phase-coherent degenerate parametric amplifiers. The prototype was used to validate both the large-signal transducer gain analytical model and simulated data. The analytical model demonstrated a direct trade-off between gain and stability, therefore, an in-depth stability study was performed to explore the unique coexistence of a parametric divide-by-two oscillatory solution with the source input in the large-signal regime and to trace solution curves perturbed in the periodic regime.

Combining the traits of both phase-incoherent upconverting and negative-resistance parametric amplifiers, a previously unknown parametric architecture was developed: phase-coherent upconverting parametric amplifiers. This new architecture uses commensurate source and pump frequencies to generate a negative resistance that is capable of upconversion with gain. Using the phase-coherent degenerate parametric amplifier prototype board, phase-coherent upconversion with gain was demonstrated from the source input frequency to its third harmonic. An analytical model describing the large-signal transducer gain of phase-coherent upconverting parametric amplifiers from the first to the third harmonic of the source input was derived and validated using the prototype board and simulations. The phase-coherent upconverting parametric amplifier demonstrated an achievable transducer gain greater than the theoretical limit imposed by the Manley-Rowe relations for phase-incoherent upconverting parametric amplifiers.

Single-frequency parametric amplifiers can be considered a comparable technology to current state-of-the-art. Solid-state transconductance power amplifiers currently comprise the majority of the power amplifier market and are still the topic of academic and industrial research. In order to compare solid-state transconductance technology to parametric, a figure of merit must be defined. Let

$$FOM_1 = \frac{\%BW \times \text{Gain} \times \text{Output Power}}{\text{Area}} \quad (6.1)$$

be said figure of merit, taking into account the metrics percent bandwidth, power gain, output power, and total amplifier area. Note that efficiency is being omitted, since transconductance power amplifiers measure efficiency in terms of a DC-RF power conversion, whereas parametric amplification is a process of RF-RF power conversion. Using (6.1), a technology comparison was performed between degenerate parametric amplifiers and the best solid-state transconductance power amplifiers available today from popular vendors, as seen in Fig. 37.

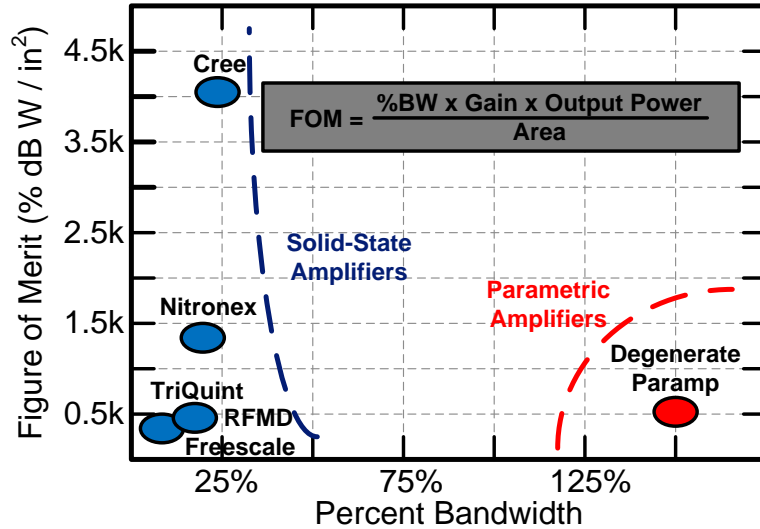


Figure 37: Technology comparison of current state-of-the-art solid-state transconductance amplifiers to degenerate parametric amplifiers.

Figure 37 makes it clear that while the operating bandwidth of single-frequency parametric amplifiers can be quite significant they are lacking in comparable output power that results in a lower figure of merit than most of their transconductance counterparts. There are several techniques that can be implemented to increase the output power of single-frequency parametric amplifiers, but each comes with a design trade-off. For instance, increasing the voltage swing across the nonlinear reactance by increasing the pumping power level would increase the voltage swing across the load, resulting in a greater average power being delivered to the load. However, the stability analysis performed in Chapter 5 demonstrated that increasing the pump power level could result in a flip bifurcation that would destabilize the amplifier. Another possibility to increase the average power delivered to the load would be to transform the load impedance to a lower value, but this typically requires high-Q matching networks that would limit the operating bandwidth.

Current state-of-the-art mixers with conversion gain can be compared to phase-coherent upconverting parametric amplifiers. As with single-frequency amplifiers, a figure of merit must be defined that relates the comparable critical metrics. Let

$$FOM_2 = \frac{\%BW \times \text{Conversion Gain}}{\text{Area} \times \text{No. of Active Components}} \quad (6.2)$$

be said figure of merit, taking into consideration the frequency range of the mixer, upconversion gain, total mixer area, and the required number of active components. Using (6.2), a second technology comparison was performed between phase-coherent upconverting parametric amplifiers and the best reported upconverting mixers with conversion gain by Wang et al. in [51], Chen et al. in [52], Johansen et al. in [53], and Su et al. in [54], as seen in Fig. 38.

Figure 38 shows a large difference in the figure of merit between phase-coherent

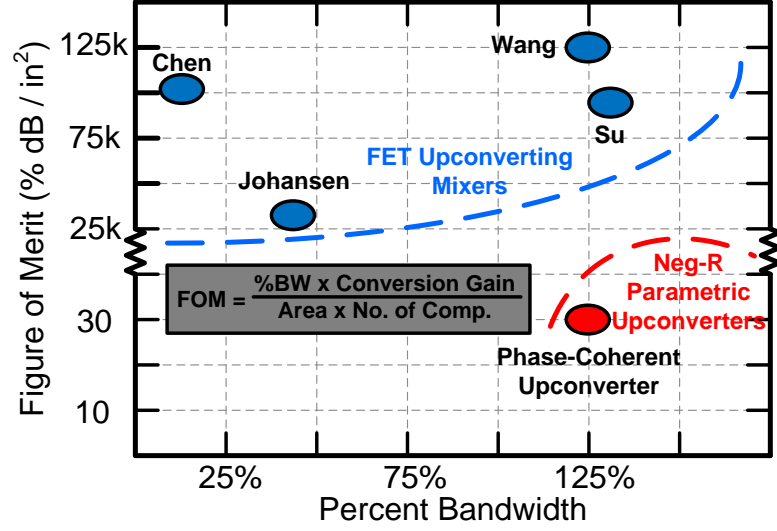


Figure 38: Technology comparison of phase-coherent upconverting parametric amplifiers to reported upconverting mixers with conversion gain.

upconverting parametric amplifiers and recently reported state-of-the-art. The phase-coherent upconverting parametric amplifier prototype was fabricated in a microstrip environment for testing and measurement at microwave frequencies. The resulting prototype board is large compared to the FET upconverting mixers in Fig. 38, thus, by (6.2), the FET upconverting mixers will dominate phase-coherent upconverting parametric amplifiers. Expanding this work to be compatible with, say, a CMOS-based process would significantly decrease the overall amplifier size, resulting in phase-coherent upconverting parametric amplifiers being comparable in performance and size to FET upconverting mixers.

6.2 Contributions

The novel contributions of this work are summarized as follows.

1. Development of analytical models that can accurately predict both linear transducer gain and RF-RF conversion efficiency of phase-incoherent upconverting parametric amplifiers [28, 55]

- Developed simulations and breadboard prototypes for two phase-incoherent upconverting parametric amplifiers at VHF and RF frequencies to validate the analytical models and demonstrate the concept of parametric upconversion
 - Demonstrated conditional stability of phase-incoherent upconverting parametric amplifiers due to the possibility of a flip bifurcation at high pump power levels
2. Development of analytical models that can accurately predict large-signal transducer gain and gain-compression of phase-coherent degenerate parametric amplifiers [56, 57]
 - Developed simulations and a printed circuit board prototype for a microwave broadband high-gain double-balanced phase-coherent degenerate parametric amplifier to validate the analytical models
 - Successfully implemented a double-balanced mixer architecture as a phase-coherent degenerate parametric amplifier and demonstrated an octave of usable bandwidth with an average of 26 dB power gain
 - Through the analytical models, the mechanism of gain compression responsible for AM-AM distortion in phase-coherent degenerate parametric amplifiers was identified
 3. An in-depth stability study was performed on phase-coherent degenerate parametric amplifiers to explore the unique bifurcation in both the large-signal and periodic regime that coexists with the source input [58]
 4. Development of a previously unknown parametric architecture (phase-coherent upconverting parametric amplifiers) that is capable of upconverting a signal with gain through a negative resistance [59]

- Developed an analytical model that can accurately predict the upconverting transducer gain from the source input frequency to its third harmonic
- The phase-coherent degenerate parametric amplifier prototype was used to both demonstrate the operation of the new parametric architecture and to validate the analytical model
- Demonstrated conditional stability of phase-coherent upconverting parametric amplifiers through the transducer gain analytical model
- Demonstrated that phase-coherent upconverting parametric amplifiers are capable of a transducer gain greater than the Manley-Rowe theoretical limit for phase-incoherent upconverting parametric amplifiers

6.3 Future Work

To finalize the study of parametric amplifiers and to determine if they are implementable as commercial RF power amplifiers, several additional tasks must be completed. While phase-incoherent upconverting parametric amplifiers are capable of high gain and moderate efficiency, they suffer from bandwidth limitations. This can be seen in the Manley-Rowe relations since the ideal gain is $\frac{\omega_o}{\omega_s}$, where $\omega_o = \omega_s + \omega_p$. To achieve high gain, either the pump frequency must be increased, or the source frequency must be decreased (or both may be necessary), resulting in the upconverted spectrum being very near that of the pump, necessitating high-Q filters to separate the two, and thus decreasing the overall bandwidth of the amplifier. Negative-resistance parametric amplifiers offered higher gain and relaxed filtering requirements with the option of degenerate operation, thus, work on phase-incoherent upconverting parametric amplifiers was abandoned. However, before the change to negative-resistance parametric amplifiers several solutions were investigated (though not in detail) that could ease filtering requirements and extend the operating bandwidth

of phase-incoherent upconverting parametric amplifiers. Image-rejection mixer architectures, discussed in detail in [45], separate the upper and lower sidebands from the local oscillator (pump) through hybrid couplers and power combiners. There are multiple references that demonstrate broadband hybrid couplers and power combiners, however, image-rejection mixer architectures tend to be lossy [60, 61]. Nevertheless, further investigation into increasing the operating bandwidth of phase-incoherent upconverting parametric amplifiers seems warranted.

The author was able to demonstrate a broadband phase-coherent degenerate parametric amplifier with high gain and stable operation. This was achieved through point-by-point phase equalization and input/output impedance tuning in order to demonstrate the concept. For this parametric architecture to be implementable in any commercial process the conditions outlined in Chapter 2 to generate a negative resistance must be satisfied by a combination of broadband impedance matching networks and resonance structures. Broadband group delay equalizers will also be necessary to set and maintain the phase condition $\phi_p = 2\phi_s$. There are plenty of resources available for the design of broadband impedance matching networks, both lumped and distributed, as well as group delay equalizers, however, the challenge will come in the design of a broadband resonance network. Within the usable bandwidth of the parametric amplifier, the reactance dual (inductive or capacitive) seen by the primary nonlinear reactance responsible for the parametric action (nonlinear capacitance or nonlinear inductance) must be very close to resonance to establish high parametric gain. This requires a frequency-dependent inductor in the case of a nonlinear capacitance acting as the parametric element or a frequency-dependent capacitor in the case of a nonlinear inductance. In the practical case of using varactor diodes as a nonlinear capacitance, structures such as printed microstrip inductors can act as broadband frequency-dependent inductors due to the capacitive coupling between the coiled lines, but the percent change in inductance is small [62]. A BiCMOS-based

frequency-dependent inductor was report in [63] that demonstrated multi-octave capability but very little change in inductance as well.

In addition to the need for broadband impedance matching networks, resonance structures, and group delay equalizers, phase-coherent degenerate parametric amplifiers must demonstrate high RF-RF conversion efficiency to be considered as a viable RF power amplifier architecture. The development of (3.51) suggests that high efficiency is obtainable simultaneously with high gain and stability, however, in practice, this is a challenging problem. The derivation of (3.51) assumed all unwanted harmonics generated by the nonlinear reactance were properly terminated such that no average power was dissipated at these frequencies. Achieving this in practice typically requires stringent filter requirements for both its in-band and out-of-band impedances. If the filter is not to also act as the impedance matching network, then its in-band impedance cannot disrupt any impedance transformation (or must be designed to work in conjunction with the transforming network). The filter's out-of-band impedance should be designed to provide a broadband open termination. This is necessary so that the filter does not short any voltage potential seen across the nonlinear reactance's terminals as these voltages drive the parametric action. Considering the necessary filtering requirements, broadband impedance matching, broadband resonance matching, group delay equalizing, source, pump, and output current isolation, and stability concerns, achieving a simultaneous stable, broadband, high gain and efficiency, high output power, phase-coherent degenerate parametric amplifier is a difficult task.

The development of phase-coherent upconverting parametric amplifiers as a new parametric architecture demonstrated the ability to go beyond the theoretical limits imposed by Manley and Rowe for phase-incoherent upconverting parametric amplifiers. This new architecture possesses the same practical implementation problems as the phase-coherent degenerate parametric amplifier. Investigation of term 1 in

(3.66) shows that phase-coherent upconverting parametric amplifiers are sensitive to small perturbations in circuit parameters, therefore, an in-depth stability study, similar to that performed for phase-coherent degenerate parametric amplifiers, should be performed to determine the trade-off between upconverting gain and stability.

Both the phase-coherent degenerate parametric amplifier and the phase-coherent upconverting parametric amplifier utilized the same printed circuit board prototype to demonstrate functionality and the concepts discussed in previous chapters. As described in Chapter 4, the prototype was fabricated on 62 mils thick Rogers 4350 RF substrate material with 1 oz copper plating with an overall board area of approximately 9 square inches. During the time the work in this thesis was performed, the available equipment limited the testing frequency range from DC to 6 GHz. Within this frequency range, microstrip environments are preferable for its ease of access to components and connector adaptability. The analytical models developed in Chapter 3 for phase-coherent degenerate parametric amplifiers and phase-coherent upconverting parametric amplifiers show that these architectures are implementable at frequencies beyond the microwave range. These parametric architectures should be made compatible with current CMOS-based processes to explore their performance above microwave frequencies. In addition to investigating parametric architectures at millimeter-wave frequencies and above, which is currently an active research topic in academia to expand the use of the electromagnetic spectrum, it will demonstrate that they can successfully undergo size reduction making both phase-coherent degenerate parametric amplifiers and phase-coherent upconverting parametric amplifiers more attractive based on the figures of merit in (6.1) and (6.2).

Finally, the effect of load line modulation of the pumping power amplifier on the RF-RF conversion efficiency needs to be investigated. As the input source power level is increased, the pump port impedance shifts from being mostly reactive towards 50 Ohms, as seen in Fig. 39.

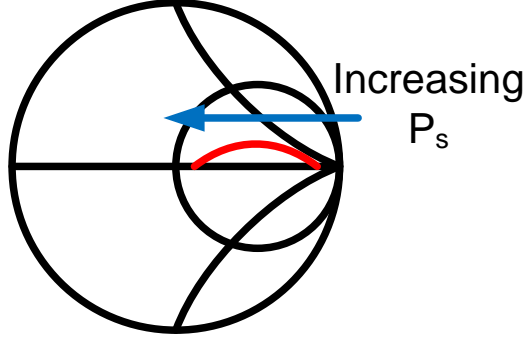


Figure 39: Change in the pump port impedance as the source drive level increases.

The pump port impedance serves as the load for the pump PA. Therefore, as the pump port impedance changes the optimal load resistance to maximize the pump PA DC-RF efficiency changes. For reduced conduction angle power amplifiers, the optimal load resistance can be related to the maximum drain current and voltage by (6.3) [9].

$$R_{L,opt} = \frac{2V_{DD}}{I_{Max}} \rightarrow I_{max} = \frac{2V_{DD}}{R_{L,opt}} \quad (6.3)$$

As the source power increases, the pump port impedance decreases and I_{Max} must increase. The DC current drawn by the drain is proportional to I_{Max} and this shift in the load-line results in a decrease in DC-RF efficiency of the pump PA. As a result, the process of RF-RF power conversion must be efficient when the source power level is backed off as opposed to peaking under high source drive level otherwise the decrease in efficiency of the pump PA will decrease the overall efficiency of parametric amplifiers. Investigating methods of obtaining high RF-RF conversion efficiency when the source power level is backed off would be valuable in the development of any parametric architecture.

Bibliography

- [1] N. Srirattana, A. Raghavan, D. Heo, P. E. Allen, and J. Laskar, "Analysis and design of a high-efficiency multistage doherty power amplifier for wireless communications," *Microwave Theory and Techniques, IEEE Transactions on*, vol. 53, no. 3, pp. 852–860, 2005.
- [2] F. H. Raab, "Class-e, class-c, and class-f power amplifiers based upon a finite number of harmonics," *Microwave Theory and Techniques, IEEE Transactions on*, vol. 49, no. 8, pp. 1462–1468, 2001.
- [3] D. Kang, J. Choi, D. Kim, and B. Kim, "Design of doherty power amplifiers for handset applications," *Microwave Theory and Techniques, IEEE Transactions on*, vol. 58, no. 8, pp. 2134–2142, 2010.
- [4] D. Chowdhury, C. D. Hull, O. B. Degani, Y. Wang, and A. M. Niknejad, "A fully integrated dual-mode highly linear 2.4 ghz cmos power amplifier for 4g wimax applications," *Solid-State Circuits, IEEE Journal of*, vol. 44, no. 12, pp. 3393–3402, 2009.
- [5] P. Gray, P. Hurst, S. Lewis, and R. Meyer, in *Analysis and Design of Analog Integrated Circuits*, 4th ed. John Wiley and Sons, Inc., 2001, ch. 1, pp. 38–73.
- [6] Y. P. Tsividis, in *Operation and Modeling of the MOS Transistor*. McGraw-Hill, 1987, p. 294.
- [7] P. Gray, P. Hurst, S. Lewis, and R. Meyer, *Analysis and Design of Analog Integrated Circuits*. John Wiley and Sons, Inc., 2001.
- [8] "Cgh09120f gan hemt for wcdma, lte, mc-gsm," Cree, Inc., Durham, North Carolina, United States.
- [9] S. C. Cripps, *RF Power Amplifiers for Wireless Communications*. Artech House, Inc., 2006.
- [10] "Class e - a new class of high efficiency tuned single-ended power amplifiers," vol. 10, no. 3.
- [11] "Idealized operation of the class e tuned power amplifier," vol. 24, no. 12.
- [12] "Efficiency of doherty rf power systems," vol. BC-33, no. 3.
- [13] I. Takenaka, H. Takahashi, K. Ishikura, K. Hasegawa, K. Asano, and M. Kanamori, "A 240w doherty gaas power fet amplifier with high efficiency and low distortion for w-cdma base stations," in *Microwave Symposium Digest, 2004 IEEE MTT-S International*, 2004, pp. 525–528.

- [14] F. H. Raab and D. J. Rupp, "High-efficiency single-sideband hf/vhf transmitter based upon envelope elimination and restoration," in *HF Radio Systems and Techniques, 1994., Sixth International Conference on*, 1994, pp. 21–25.
- [15] "Comparison of linear single-sideband transmitters with envelope elimination and restoration single-sideband transmitters," vol. 44, no. 12.
- [16] J.-H. Chen and J. S. Kenney, "A crest factor reduction technique for w-cdma polar transmitters," in *Radio and Wireless Symposium, 2007 IEEE*, 2007, pp. 345–348.
- [17] P. Johannessen, W. Ku, and J. Andersen, "Theory of nonlinear reactance amplifiers," *Magnetics, IEEE Transactions on*, vol. 3, no. 3, pp. 376–380, 1967.
- [18] H. Heffner and G. Wade, "Gain, band width, and noise characteristics of the variable-parameter amplifier," *Journal of Applied Physics*, vol. 29, no. 9, pp. 1321–1331, 1958.
- [19] M. Hines, "The virtues of Nonlinearity—Detection, frequency conversion, parametric amplification and harmonic generation," *Microwave Theory and Techniques, IEEE Transactions on*, vol. 32, no. 9, pp. 1097–1104, 1984.
- [20] L. Blackwell and K. Kotzebue, *Semiconductor Diode Parametric Amplifiers*. Prentice Hall, Inc., 1961.
- [21] D. P. Howson and R. B. Smith, *Parametric Amplifiers*. McGraw-Hill Education, Apr. 1970.
- [22] R. Engelbrecht, "Parametric energy conversion by nonlinear admittances," *Proceedings of the IRE*, vol. 50, no. 3, pp. 312–321, 1962.
- [23] J. Edrich, "Low-noise parametric amplifiers tunable over one full octave," *Solid-State Circuits, IEEE Journal of*, vol. 7, no. 1, pp. 32–37, 1972.
- [24] C. Boyd, "Design consideration for parametric amplifier low-noise performance," *Military Electronics, IRE Transactions on*, vol. MIL-5, no. 2, pp. 72–80, 1961.
- [25] H. Okean, J. DeGruyl, and E. Ng, "Ultra low noise, ku-band parametric amplifier assembly," in *Microwave Symposium Digest, 1976. MTT '76. IEEE MTT-S International*, 1976, pp. 82–84.
- [26] A. Smith, R. Sandell, J. Burch, and A. Silver, "Low noise microwave parametric amplifier," *Magnetics, IEEE Transactions on*, vol. 21, no. 2, pp. 1022–1028, 1985.
- [27] J. Manley and H. Rowe, "Some general properties of nonlinear elements-part i. general energy relations," *Proceedings of the IRE*, vol. 44, no. 7, pp. 904–913, 1956.

- [28] B. R. Gray, B. Melville, and J. S. Kenney, "Analytical modeling of microwave parametric upconverters," *Microwave Theory and Techniques, IEEE Transactions on*, vol. 58, no. 8, pp. 2118–2124, 2010.
- [29] H. Iwasawa, "The extended theory of the manley-rowe's energy relations in nonlinear elements and nonlinear lossless medium," *Microwave Theory and Techniques, IRE Transactions on*, vol. 8, no. 4, pp. 459–460, 1960.
- [30] C. Someda, "Modified manley-rowe relations for parametric interaction with small linear losses," *Electronics Letters*, vol. 3, no. 8, pp. 383–384, 1967.
- [31] B. Anderson, "When do the manley-rowe relations really hold?" *Electrical Engineering, Proceedings of the Institution of*, vol. 113, no. 4, pp. 585–587, 1966.
- [32] G. Longo and C. Someda, "On the scope and validity of the manley-rowe relations," *Electronics Letters*, vol. 3, no. 5, pp. 179–180, 1967.
- [33] E. Rutz-Philipp, "Design of high efficiency frequency doublers based on manley-rowe's energy relations," in *Electron Devices Meeting, 1965 International*, 1965, p. 56.
- [34] T. Hattori, K. Takeuchi, and T. Ishii, "Cascading in thz wave generation by optical rectification," in *Infrared Millimeter Waves and 14th International Conference on Terahertz Electronics, Joint 31st International Conference on*, 2006, p. 192.
- [35] V. Kozlov, K. Vodopyanov, M. Fejer, Y. Lee, and W. Hurlbut, "Thz generation by cascaded optical down-conversion," in *Infrared Millimeter Waves and 14th International Conference on Terahertz Electronics, Joint 31st International Conference on*, 2006, p. 390.
- [36] I. Waldmueller, W. Chow, and M. Wanke, "Optically-assisted electrically-driven thz generation - a new approach for efficient thz quantum cascade lasers," in *Lasers and Electro-Optics, Conference on*, 2007, pp. 1–2.
- [37] Y. Jiang and Y. Ding, "High-power thz pulses based on difference-frequency generation," in *IEEE Lasers and Electro-Optics Society, 21st Annual Meeting of the*, 2008, pp. 792–793.
- [38] L. Blackwell and K. Kotzebue, in *Semiconductor Diode Parametric Amplifiers*, 1st ed. Prentice Hall, Inc., 1961, ch. 3, pp. 37–42.
- [39] A. Suárez, *Analysis and Design of Autonomous Microwave Circuits*. Wiley-IEEE Press, 2009.
- [40] R. E. Collin, *Foundations for Microwave Engineering*, 2nd ed. Wiley-IEEE Press, Dec. 2000.

- [41] A. Saltelli, S. Tarantola, F. Campolongo, and M. Ratto, *Sensitivity Analysis in Practice: A Guide to Assessing Scientific Models*, 1st ed. Wiley, Apr. 2004.
- [42] L. Chua, in *Introduction to Nonlinear Network Theory*, 1st ed. McGraw-Hill, Inc., 1969, ch. 1, pp. 31–32.
- [43] B. Perlman, “Current-Pumped Abrupt-Junction varactor Power-Frequency converters,” *Microwave Theory and Techniques, IEEE Transactions on*, vol. 13, no. 2, pp. 150–161, 1965.
- [44] D. Xu and G. Branner, “An efficient technique for varactor diode characterization,” in *Circuits and Systems, 1997. Proceedings of the 40th Midwest Symposium on*, vol. 1, 1997, pp. 591–594 vol.1.
- [45] S. Maas, *Microwave Mixers*. Artech House, Inc., 1993.
- [46] A. Smith, R. Sandell, J. Burch, and A. Silver, “Stability and power-gain invariants of linear two-ports,” *Circuit Theory, IEEE Transactions on*, vol. 9, pp. 29–32, 1962.
- [47] A. Suárez, in *Analysis and Design of Autonomous Microwave Circuits*, 1st ed. John Wiley and Sons, Inc., 2009, ch. 3, pp. 156–160.
- [48] J. Jugo, J. Portilla, A. Suárez, and J. Collantes, “Closed-loop stability analysis of microwave amplifiers,” *IEEE Electronics Letters*, vol. 37, no. 4, pp. 226–228, 2001.
- [49] J. Guckenheimer and P. Holmes, *Nonlinear Oscillations, Dynamical Systems, and Bifurcations of Vector Fields*. Springer-Verlag, 1983.
- [50] H. Kawakami, “Bifurcation of periodic responses in forced dynamic nonlinear circuits,” *Circuits and Systems, IEEE Transactions on*, vol. 31, pp. 248–260, 1984.
- [51] M. Wang and C. E. Saavedra, “Reconfigurable broadband mixer with variable conversion gain,” in *Microwave Symposium Digest, 2011 IEEE MTT-S International*, 2011, pp. 1–4.
- [52] “An 80 ghz high gain double-balanced active up-conversion mixer using 0.18 micron sige bicmos technology,” vol. 21, no. 6.
- [53] “A high conversion-gain q-band inp dhbt subharmonic mixer using lo frequency doubler,” vol. 56, no. 3.
- [54] Z.-C. Su and Z.-M. Lin, “A 18.9 db conversion gain folded mixer for wimax system,” in *Circuits and Systems, 2008. APCCAS 2008. IEEE Asia Pacific Conference on*, 2008, pp. 292–295.

- [55] B. Gray, J. Kenney, and R. Melville, "Behavioral modeling and simulation of a parametric power amplifier," in *Microwave Symposium Digest, 2009. MTT '09. IEEE MTT-S International*, 2009, pp. 1373–1376.
- [56] B. R. Gray, F. Ramírez, R. Melville, A. Suárez, and J. S. Kenney, "A broadband double-balanced phase-coherent degenerate parametric amplifier," *Microwave and Wireless Components Letters, IEEE*, vol. 21, no. 11, pp. 607–609, 2011.
- [57] B. R. Gray, M. Pontón, A. Suárez, and J. Kenney, "Analytical modeling of transducer gain and gain compression in degenerate parametric amplifiers," in *Radio and Wireless Symposium, 2012. RWS '12. IEEE*, 2012.
- [58] M. Pontón, B. R. Gray, F. Ramírez, A. Suárez, and J. Kenney, "An in-depth stability analysis of degenerate parametric amplifiers," in *Microwave Symposium Digest, 2012. MTT '12. IEEE MTT-S International*, 2012, Pending Acceptance.
- [59] B. R. Gray, M. Pontón, A. Suárez, and J. Kenney, "A phase-coherent upconverting parametric amplifier," in *Microwave Symposium Digest, 2012. MTT '12. IEEE MTT-S International*, 2012, Pending Acceptance.
- [60] S.-C. Jung, R. Negra, and F. M. Ghannouchi, "A miniaturized double-stage 3db broadband branch-line hybrid coupler using distributed capacitors," in *Microwave Conference, 2009. APMC 2009. Asia Pacific*, 2009, pp. 1323–1326.
- [61] G. Prigent, E. Rius, H. Happy, K. Blary, and S. Lepilliet, "Design of wide-band branch-line coupler in the g-frequency band," in *Microwave Symposium Digest, 2006. IEEE MTT-S International*, 2006, pp. 986–989.
- [62] I. J. Bahl, *Lumped Elements for RF and Microwave Circuits*. Artech House, 2003.
- [63] W. Woods, H. Ding, G. Wang, P. Sun, J. Rascoe, P. Tannhof, and J. Pekarik, "On-chip frequency-dependent inductor for multi-band circuit designs," in *Microwave Conference (EuMC), 2010 European*, 2010, pp. 421–442.

VITA

Blake Gray was born in Kansas City, Missouri on July 30th, 1981, to Bill and Linda Gray. He spent his first years growing up in Lawson, Missouri, then was moved to Liberty, Missouri, where later he attended and graduated from Liberty High School. He then enrolled at University of Missouri - Rolla (now Missouri University of Science and Technology), obtaining bachelors degrees in both electrical engineering and computer engineering with Magna Cum Laude graduating honors. During his undergraduate years at University of Missouri - Rolla, Blake participated in several extra-curricular activities such as working with Eta Kappa Nu (an electrical and computer engineering honor society), the student branch of IEEE, and Alpha Phi Omega (a national philanthropic service society), where, while serving as chapter president was awarded Best Section President.

After graduating with his bachelors, Blake stayed at University of Missouri - Rolla to earn a masters degree in electrical engineering under the advisement of Professor Randy Moss. His research work focused on the automated detection of mine wall convergence using laser light resulting in several peer-reviewed journal publications.

Blake then relocated to Atlanta, Georgia, where he attended Georgia Institute of Technology to work on a doctorate in electrical engineering under the advisement of Professor J. Stevenson Kenney. His research work has been focused on communication systems technologies, specifically new and emerging power amplifier architectures. This focus lead to the development of broadband parametric amplifier architectures that centered on broadband operation and gain. His contributions have been noted in multiple peer-reviewed journal publications and conference presentations.